Institute for Ship Structural Design and Analysis

Hamburg University of Technology

Investigation of constraint effect on fatigue crack growth rate measurements

Einfluss von Spannungs-Mehrachsigkeit auf Risswachstumsmessungen

Masterthesis

Veronika Hochfellner

August 27, 2017

Supervisors: Prof. D.Sc. (Tech.) Sören Ehlers
D.Sc. (Tech.) R. U. Franz von Bock und Polach
Moritz Braun, M.Sc.

TUHH
Hamburg University of Technology

I, Veronika Hochfellner, certify that the work presented here is, to the best of my knowledge and belief, original and the result of my own investigations, except where otherwise indicated. It has not been submitted, either in part or whole, for a degree at this or any other University.

Place, Date

Signature

Veronika Hochfellner
Matr. Nr.: 43594
Hamburg University of Technology
Institute for Ship Structural Design and Analysis (M-10)
Am Schwarzenberg-Campus 4(c)
21073 Hamburg

Abstract

For the purpose of reliable life prediction the fatigue crack growth behaviour of a material has to be well-known. Therefore standardized fatigue crack growth tests are made with test specimens of the material. The obtained fatigue crack growth data is taken as material specific data and is given without any information of the test conditions and used specimen geometry. However, in several studies a geometry dependency of the test specimen on the fatigue crack growth data is found.

Hence in this investigation experiments on fatigue crack growth behaviour are made with two different specimen geometries, the middle tension specimen M(T) and the compact (tension) specimen C(T). The direct current potential drop (DCPD) method is used to determine the crack lengths which is calibrated with the aid of beach marks and crack detection gauges. Two different configurations of the DCPD method are implemented to gain acceptable results. With the obtained data fatigue crack growth curves are established which are analysed regarding the geometry influence of the used test specimens. Discrepancies in the fatigue crack growth curves between the tested specimens are found.

With these findings an approach is tested to create a material curve which is independent of the specimen geometry. However, this approach is not leading to satisfactory results.

The implementation of the DCPD method in its main configuration on the used experimental setup proves to be applicable for fatigue crack growth tests on different geometries and will be used in further studies at low temperatures.

TUHH Hamburg University of Technology

Ship Structural Design & Analysis

TUHH · M-10 · Am Schwarzenberg Campus 4C · D-21073 Hamburg

MASTER THESIS 2017

for

Veronika Hochfellner

Investigation of constraint effect on fatigue crack growth rate measurements

The fatigue life of structures can be divided in two stages. While the crack initiation stages can occupy up to 90% of the lifetime of smooth specimen (Clark and Knott, 1975), the fatigue life of welded structures is generally propagation-dominated. Once a crack can be detected in a smooth specimen, the lifetime until final fracture is seemingly short. However, there is also a wide range of situations that are neither initiation- nor propagation-dominated. Such situations mainly cover structures with stress concentrations less severe than at welded joints. Thus, fatigue assessment and test methods vary significantly for those three cases.

Standardization of laboratory test specimen for fatigue crack growth rate measurements play an important role in fracture mechanics. However, in order to apply those test results for structural integrity assessment of real structures they need to be transferred from test conditions to engineering applications. In general, the test condition eg. specimen size, section thickness, loading rate, crack depth and shape differ from the conditions during fracture and crack growth of actual structural members. Those effects are in literature referred to as “constraint effects” and have a significant effect on the stress-strain state around the crack tip.

Recommendations for estimating material data for fatigue crack growth analysis in failure assessment procedures and codes like BS 7910:1999 or API 579-1, are usually given regardless of the test conditions and specimen geometries employed in respective studies. However, the significance of crack tip constraint on fatigue crack growth rate and fracture toughness was demonstrated by Varfolomeev et al. (2011) for example. Hence, this project is concerned with the investigation of constraint effects on fatigue crack growth rate measurements in typical test specimen. For this purpose, the direct current potential drop method will be applied.

1) Construction of the missing elements for fatigue crack growth rate measurements in compact tension (C(T)) specimen
2) Calibration of the direct current potential drop method for fatigue crack growth rate measurements in C(T) specimen
3) Crack growth rate curves shall be measured with notched middle tension (M(T)) and C(T) specimen based on the relevant industry standards
4) The test results shall be analysed regarding uncertainties and be compared with published data

5) The test results shall be analysed with respect to the constraint effect

Literature studies of specific topics relevant to the thesis work shall be included.

The work scope may prove to be larger than initially anticipated. Subject to approval from the supervisors, topics may be deleted from the list above or reduced in extent.

In the thesis the candidate shall present his personal contribution to the resolution of problems within the scope of the thesis work.

Theories and conclusions should be based on mathematical derivations and/or logic reasoning identifying the various steps in the deduction.

The candidate should utilise the existing possibilities for obtaining relevant literature.

Thesis format

The thesis should be organised in a rational manner to give a clear exposition of results, assessments, and conclusions. The text should be brief and to the point, with a clear language and the objective to be published in a conference article and/or scientific journal. It is thus desirable that the thesis is written in English. Telegraphic language should be avoided.

The thesis shall contain the following elements: An executive summary, list of symbols and acronyms, followed by the main body of the thesis consisting of a brief background introduction, a state of the art defining the knowledge gaps defining the scope or work and limitations, the actual contribution chapters, conclusions with recommendations for further work, references and (optional) appendices. All figures, tables and equations shall be numerated.

The supervisors require that the candidate, in an early stage of the work, presents a written plan for the completion of the work. The plan may include a budget for the use of computer and laboratory resources if applicable, which will be charged to the department. Overruns shall be reported to the supervisors.

The original contribution of the candidate and material taken from other sources shall be clearly defined following basic academic principles and an acknowledged referencing system, which includes the name of the referred authors followed by the publication year in the text. The subsequent reference list can thus be alphabetical.

The report shall be submitted in two copies:
- Signed by the candidate
- The text defining the scope included
- In bound volume(s)
- Drawings and/or computer prints, which cannot be bound should be organised in a separate folder.
- The report shall also be submitted in PDF along with essential input files for computer analysis, spread sheets, MATLAB files etc. in digital format.

Ownership
According to the current rules, the candidate has the ownership of the thesis. Any use of the thesis has to be approved by TUHH M-10 (or external partner when this applies). TUHH M-10 has the right to use the thesis as if a TUHH M-10 employee carried out the work, if nothing else has been agreed in advance.

Thesis supervisors
Prof. D.Sc. (Tech.) Sören Ehlers (TUHH),
D.Sc. (Tech.) R.U. Franz von Bock und Polach (TUHH),
Moritz Braun (TUHH)

Deadline: 27.08.2017

Hamburg, 27.01.2017

Contents

1 Introduction **1**

2 State of the art **3**

2.1 Fracture mechanics . . . 3

2.1.1 Introduction . . . 3

2.1.2 Displacement modes of a crack . . . 4

2.1.3 Stress intensity factor K . . . 5

2.1.4 Plastic zone size and K-field . . . 8

2.2 Fatigue crack growth . . . 9

2.2.1 Introduction . . . 10

2.2.2 Cyclic loading . . . 10

2.2.3 Fatigue crack growth behaviour . . . 11

2.2.4 Constraint effect . . . 15

2.2.5 Fatigue at low temperatures . . . 18

2.3 Direct current potential drop (DCPD) method . . . 20

2.3.1 Principle . . . 20

2.3.2 Calibration of the DCPD method . . . 20

2.3.3 Current input location and potential measurement lead placement . . . 22

2.3.4 Problems using the DCPD method . . . 25

2.4 Objective of the work . . . 26

3 The test specimens **29**

3.1 The middle tension specimen, M(T) . . . 30

3.2 The compact specimen, C(T) . . . 31

4 Experimental setup and procedures **35**

4.1 Used equipment . . . 35

4.1.1 Resonant testing machine . . . 36

4.1.2 Power source . . . 36

4.1.3 Voltmeter . . . 36

4.1.4 Crack detection gauges . . . 37

4.1.5 Isolation of the test frame . . . 37

4.1.6 Current input and potential measurement lead wires . . . 38

4.2 Test procedure for fatigue crack growth testing . . . 39

4.3 Determination of crack length . . . 39

5 Preliminary tests **41**

5.1 Testing of the equipment and setting of the DCPD initial configuration . . . 41

5.2 Implementation of the DCPD method: initial configuration . . . 42

5.2.1 M(T) specimen 43
5.2.2 C(T) specimen 46
5.2.3 Results of DCPD initial configuration 47
5.3 Testing a new arrangement 47

6 Implementation and results of the DCPD method: main configuration 51
6.1 Results of DCPD main configuration 53
6.1.1 Crack growth 55
6.1.2 Fatigue crack growth rate 57

7 Summary and Conclusion 65

8 Recommendations for future work 67

Bibliography 67

Appendices A1

A Design drawings A1

B Data of used test specimens A9
B.1 M(T) specimens A10
B.1.1 Specimen $VJ1$ A13
B.1.2 Specimen $VJ3$ A14
B.2 C(T) specimen A15
B.2.1 Specimen $VH1$ A18
B.2.2 Specimen $VH2$ A19
B.2.3 Specimen $VH4$ A20
B.3 Beach marks A21

List of Figures

2.1 Wide Plate containing an elliptical hole loaded with tension 3
2.2 Stress distribution along the x-axis for the tension loading case 4
2.3 Comparison of stresses for an ideal and real crack tip and plastic zone . . . 4
2.4 Three different displacement modes 5
2.5 Coordinate system at the crack tip 5
2.6 Geometry functions F for plates under tension and F_P for the C(T) specimen 7
2.7 Plastic zone size 8
2.8 K-field 9
2.9 Measurements for LEFM limits 9
2.10 Three different types of constant amplitude stressing 10
2.11 Crack length a over number of cycles N at two different stress levels 11
2.12 Crack growth rate da/dN over crack length and stress intensity factor range ΔK for low and high stress level 12
2.13 Qualitative steps how to obtain grack growth rate curves from experiments and how to use it for an engineering application 13
2.14 Three regions of the fatigue crack growth rate curve 14
2.15 Region II, tensile mode, and region III, shear mode, of the fatigue crack growth on a fracture surface 14
2.16 Biaxiality factor B for the M(T) specimen 16
2.17 Biaxiality factor B for the C(T) specimen 17
2.18 Fatigue crack growth rate versus stress intensity factor range for the M(T) and C(T) specimen and fatigue crack growth rate versus effective stress intensity factor range ΔK^{eff} 18
2.19 Ductile to brittle transition curve obtained by two different fracture toughness test methods. 19
2.20 Effect of low temperatures on the fatigue crack growth rate curve for bcc (red) steels and for austenitic steels (blue) compared to room temperature (black) 19
2.21 Schematic Diagram of the DCPD system 20
2.22 Current input locations A and B on a C(T) specimen 23
2.23 Current input positions A (top surface) and B (side flanks) with variation of potential measurement lead position at the top surface of the C(T) specimen. Voltage increase $V_a/V_{a0} = U/U_0$ 24
2.24 Equi-potential distribution with two different current input locations on a C(T) specimen 24
2.25 Equi-potential field for an uncracked and center cracked M(T) specimen . . 25

3.1 Geometry of M(T) and C(T) specimens given in ASTM 29
3.2 Crack plane orientation 30

3.3 Notch of M(T) specimen 30
3.4 Required notch envelope and used notch shape of C(T) specimen 31
3.5 Designed C(T) specimen. 31
3.6 Clevis and pin assembly 32
3.7 Designed clevis for the C(T) specimen. 32
3.8 Die and bolt for bearing positioning of the C(T) specimen. 33
3.9 Designed welding arrangement with welding template. 34

4.1 M(T) specimen clamped in the resonant testing machine with attached potential measurement lead wires, current input wires and crack detection gauges. 35
4.2 C(T) specimen clamped in the resonant testing machine with attached potential measurement lead wires and current input wires. 36
4.3 Schematic picture of crack detection gauge FAC-5 37
4.4 Crack detection gauge FAC-5 glued to a test specimen. 38
4.5 Used circuit boards for isolation. 38
4.6 Beach marks of specimen $VJ1$ to demonstrate the crack front correction. . 40

5.1 Wire locations of the M(T) specimen using the DCPD initial configuration. 43
5.2 Wire locations of the C(T) specimen using the DCPD initial configuration. 44
5.3 Applied load, specimen $VJ4$. 44
5.4 Beach marks of specimen $VJ4$. 45
5.5 Voltage drop, specimen $VJ4$. 45
5.6 Crack detection gauges, specimen $VJ1$. 46
5.7 Asymmetrically cracked specimen $JS21$. 46
5.8 Calibration curve (Fit) for M(T) specimens obtained from beach marks and crack detection gauges from specimen $VJ1$ and $VJ4$. 48
5.9 Calibration curve (Fit) for C(T) specimens obtained from beach marks and crack detection gauges from specimen $VH1$ and $VH2$. 48

6.1 DCPD main configuration, M(T) specimen $VJ3$. 52
6.2 DCPD main configuration, C(T) specimen $VH4$. 52
6.3 Voltage drop, specimen $VJ3$. 52
6.4 Calibration curve (Fit) for the M(T) specimen $VJ3$ obtained from beach marks. 53
6.5 Calibration curve (Fit) for the C(T) specimen $VH4$ obtained from beach marks and crack detection gauge. 54
6.6 Comparison of modified Johnson's equation with created calibration curve for the M(T) specimen. 54
6.7 Comparison of Johnson's equation with created calibration curve for the C(T) specimen. 55
6.8 Crack growth versus number of cycles obtained from created calibration curve for the M(T) specimen at load ratio $R = 0.1$. 56
6.9 Crack growth versus number of cycles obtained from created calibration curve for the C(T) specimen at load ratio $R = 0.1$. 56
6.10 Calculation of crack growth rate 57
6.11 Calculation of the crack growth rate for the first load ratio block of the M(T) specimen $VJ3$ with corresponding ΔK and $2a_{avg}$. 58
6.12 Fatigue crack growth rate da/dN versus stress intensity factor range ΔK for M(T) and C(T) specimens as well as the Paris equation 59
6.13 Two stages of crack growth 59

6.14 Fatigue crack growth rate versus stress intensity factor range for M(T) and C(T) specimens obtained in literature 61
6.15 Biaxiality factor of the M(T) specimen 62
6.16 Biaxiality factor of the C(T) specimen 63
6.17 Effective stress intensity factor range versus fatigue crack growth rate of the M(T) and C(T) specimen with Paris equations 63

A.1 C(T) specimen design drawing. A2
A.2 C(T) specimen clevis design drawing. A3
A.3 DIN EN ISO 4762 M20x90 - 12.9 screw used as loading pin. A4
A.4 Distance disc design drawing. A5
A.5 Design drawing of bolt for bearings. A6
A.6 Design drawing of welding template for the C(T) specimen. A7

B.1 Stress intensity factor range ΔK versus ratio $2a_{avg}/W$ for specimen $VJ3$. . . A10
B.2 Data of specimen $VJ1$. A13
B.3 Data of specimen $VJ3$. A14
B.4 Stress intensity factor range ΔK versus ratio a_{avg}/W for specimen $VH4$. . . A15
B.5 Specimen $VH1$. A18
B.6 Specimen $VH2$. A19
B.7 Specimen $VH4$. A20
B.8 Beach marks of the tested M(T) specimen $VJ3$ and C(T) specimen $VH4$. . A21

List of Tables

2.1 Polynomial constants for B for the M(T) specimen 16
2.2 Polynomial constants for B for the C(T) specimen 16

3.1 Dimensions of used M(T) specimen and notch 30
3.2 Dimensions of used C(T) specimen and notch 31

4.1 Virtual channels for the initial and main configuration of the DCPD method. 37

6.1 Paris constants obtained for the M(T) and C(T) specimens. 58
6.2 Paris constants for stage A and B 60

B.1 Data of used M(T) specimens for the experiments at room temperature. . . A10
B.2 Data for fatigue crack growth rate curve for specimen $VJ3$. A11
B.3 Biaxiality factor B and effective stress intensity factor range ΔK^{eff} for methods a), b) and c) of specimen $VJ3$. A12
B.4 Data of used C(T) specimens for the experiments at room temperature. . . A15
B.5 Data for fatigue crack growth rate curve for specimen $VH4$. A16
B.6 Biaxiality factor B and effective stress intensity factor range ΔK^{eff} for methods a), b) and c) of specimen $VH4$. A17

List of Symbols

Symbol	Unit	Description
a	mm	Crack length
a_0	mm	Initial crack length
b	mm	Maximum crack length
B	–	Biaxiality factor
B	mm	Specimen thickness in [ASTM 2015]
C	$\frac{\mathrm{mm}/\mathrm{cycle}}{(\mathrm{MPa}\sqrt{\mathrm{m}})^m}$	Paris equation constant
da	mm	Crack growth
dN	cycle	Number of loading cycles
da/dN	mm/cycle	Fatigue crack growth rate
F	–	Geometry function
F_P	–	Geometry function
K	$\mathrm{MPa}\sqrt{\mathrm{m}}$	Stress intensity factor
K_I	$\mathrm{MPa}\sqrt{\mathrm{m}}$	Stress intensity factor, mode I
K_Ic	$\mathrm{MPa}\sqrt{\mathrm{m}}$	Fracture toughness, mode I
ΔK_{th}	$\mathrm{MPa}\sqrt{\mathrm{m}}$	Threshold stress intensity factor range
K_{max}	$\mathrm{MPa}\sqrt{\mathrm{m}}$	Maximum stress intensity factor
K_{min}	$\mathrm{MPa}\sqrt{\mathrm{m}}$	Minimum stress intensity factor
ΔK	$\mathrm{MPa}\sqrt{\mathrm{m}}$	Stress intensity factor range
K^{eff}	$\mathrm{MPa}\sqrt{\mathrm{m}}$	Effective stress intensity factor
ΔK_{eff}	$\mathrm{MPa}\sqrt{\mathrm{m}}$	Effective cyclic stress intensity factor range
m	–	Paris equation constant
P	N	Applied load
P_{max}	N	Maximum load
P_{min}	N	Minimum load
ΔP	N	Force range
R	–	Stress ratio
r	mm	Hole radius of M(T) specimen
S	N/mm^2	Nominal Stress
S_g	N/mm^2	Gross section nominal stress
ΔS	N/mm^2	Stress range

S_{max}	$^{N}/_{mm^2}$	Maximum stress
S_{min}	$^{N}/_{mm^2}$	Minimum stress
t	mm	Specimen thickness
T_{stress}	$^{N}/_{mm^2}$	T-stress
U	mV	Electrical potential difference/Voltage drop
U_0	mV	Initial/Reference electrical potential
W	mm	Specimen width
y	mm	Distance of the voltage measurement lead from the crack plane
y_I	mm	Distance from one current input location to the middle of the crack
y_U	mm	Distance between one potential measurement lead wire location and the middle of the crack
r, θ	–	Polar coordinates
x, y, z	–	Coordinate system at the crack tip
ϵ_z	–	Strain in z-direction
ν	–	Poisson's ratio
α	–	Ratio $^{a}/_{b}$
$\sigma_{x,y,z}$ $\tau_{xy,yz,zx}$	$^{N}/_{mm^2}$	Local stresses
σ_0	$^{N}/_{mm^2}$	Yield strength
$\Delta\sigma$	$^{N}/_{mm^2}$	Stress range
σ_a	$^{N}/_{mm^2}$	Stress amplitude
σ_m	$^{N}/_{mm^2}$	Mean stress
σ_{max}	$^{N}/_{mm^2}$	Maximum stress
σ_{min}	$^{N}/_{mm^2}$	Minimum stress

List of Acronyms

CCT	Center cracked tension specimen
CDG	Crack detection gauge
C(T)	Compact (tension) specimen
CTOD	Crack tip opening displacement
DC	Direct current
DCPD	Direct current potential drop method
emf	Electromotive force
ESE(T)	Eccentrically-loaded single edge crack tension specimen
FATT	Fracture appearance transition temperature
FDBT	Fatigue ductile-brittle transition
FTT	Fatigue transition temperature
LEFM	Linear-elastic fracture mechanics
M(T)	Middle tension specimen
PTFE	Polytetrafluorethylen

Chapter 1

Introduction

In engineering failure of structural components due to fatigue is of major interest. A lot of structural components contain cracks after a certain amount of time in service. These cracks become dangerous if they become too large. Therefore analyses of crack growth life of components are made to ensure safety of a component.

For this purpose the crack growth behaviour of a material has to be well-known. Standardized fatigue crack growth rate laboratory tests are made with test specimens of the used material. The obtained fatigue crack growth data is then transferred to engineering applications but unfortunately these data is taken as material specific data which is given without any information of the test conditions and used specimen geometry [Dowling 1998], [Schijve 2008] and [Varfolomeev et al. 2011].

In several studies discrepancies in fatigue crack growth rate are found between different specimen geometries of the same material. Also the fracture toughness is influenced by the geometrical shape of the test specimen. These circumstances lead to the question if the material data of the standard laboratory tests can be transferred to life prediction in service situations without considering the used specimen geometry.

As arctic regions are getting interesting to maritime and shipping industry due to large untouched gas and oil resources and the potential route through the North East Passage to connect Europe with Asia which can reduce costs in shipping, fatigue life prediction is a special issue. Studies have shown a temperature induced change of behaviour of fatigue crack growth and fracture toughness.

Due to the aforementioned circumstances new knowledge has to be gained to ensure a reliable life prediction of structures. Therefore laboratory tests at room temperatures as well as low temperatures have to be made regarding the influence of different specimen geometries on fatigue crack growth data as well as on fracture toughness. Thus data can be collected and methods can be developed to properly transfer the information obtained in experiments to structural components.

In this thesis fatigue crack growth tests are performed for two different test specimen geometries at room temperature to investigate the geometry influence on the obtained fatigue crack growth data. The used specimen geometries are the middle tension specimen M(T) and the compact (tension) specimen C(T) as given in ASTM [ASTM 2015].

This investigation is carried out in view of further fatigue tests considering low temperatures which is topic of following studies.

Chapter 2

State of the art

In this chapter a short overview of fundamentals in fracture mechanics among others the stress intensity factor and fatigue crack growth is given. Furthermore fatigue at low temperatures is touched, the constraint effect is explained and the direct current potential drop method is elucidated.

2.1 Fracture mechanics

In this section a short overview is given concerning the fundamentals of cracked members. It is explained how a crack influences the stress field of a member under tension loading and an insight on processes near the crack tip is given. The stress intensity factor in the vicinity of the crack is introduced as well as the limits of the theory of linear-elastic fracture mechanics.

2.1.1 Introduction

If a cracked member, for example a wide plate with a small elliptical hole in it, is loaded remotely with a uniform stress S perpendicular to the major axis of the hole, the stress field in the plate is influenced by this hole. In figure 2.1 the plate is loaded with homogeneous tension.

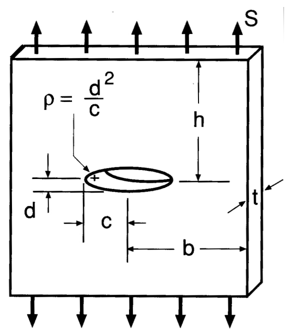

Figure 2.1 Wide Plate containing an elliptical hole loaded with tension, taken from Dowling [Dowling 1998].

The stress parallel to S measured at the crack tip along the x-axis σ_y is equal to S far away from the crack. In the vicinity of the crack tip the local stress increases and reaches a maximum at the crack tip, see figure 2.2 for the upper loading case with tension. This maximum value depends on the geometry of the hole.

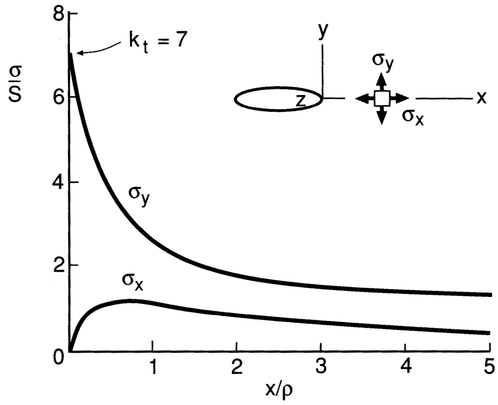

Figure 2.2 Stress distribution along the x-axis for the tension loading case, based on Dowling [Dowling 1998].

Is the tip radius of the elliptic hole approaching zero as well as the height of the ellipse, then the stress at the crack tip in theory becomes infinite. In reality an infinite stress is not possible.

In the vicinity of a crack tip yielding takes place in for instance metals. This area is called the plastic zone, see section 2.1.4 for details. Due to strong plastic deformations in this zone the edge of an ideally sharp crack becomes a non-zero radius, therefore an infinite stress cannot occur. In figure 2.3 the plastic zone for metal is depicted as well as the difference between the stress at an ideal and a real crack tip. It is shown that the stress at the real crack tip is finite and the maximum stress occurs not only at the crack tip, but also in the vicinity of it. Furthermore, the stress further away from the ideal crack is lower than it is in reality.

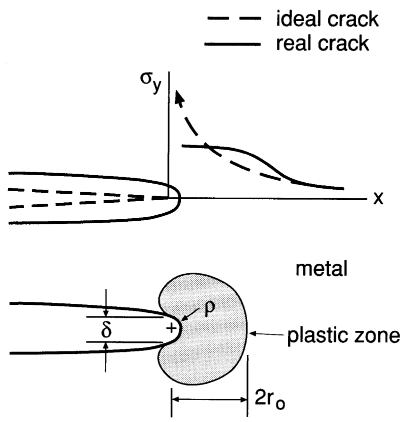

Figure 2.3 Comparison of stresses for an ideal and real crack tip and plastic zone, taken from Dowling [Dowling 1998].

2.1.2 Displacement modes of a crack

According to Tada [Tada et al. 2000] there are in general three different modes of deformation for a cracked member:

- Mode I: opening mode,
- Mode II: sliding mode,

- Mode III: shearing mode.

In figure 2.4 these three deformation modes are depicted. In mode I a member is loaded with tension, in mode II and III a shear loading is applied, but in different directions. Also a combination of the three modes is possible. In this thesis only mode I is of interest.

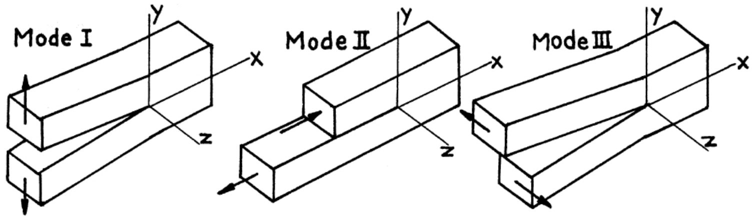

Figure 2.4 Three different displacement modes, taken from Tada [Tada et al. 2000].

2.1.3 Stress intensity factor *K*

The stress intensity factor K is a measure for the intensity of a stress field in the vicinity of a crack tip. The stress intensity factor is influenced by the crack size, the applied stress as well as the geometry. Moreover the material has to be isotropic and small-scale yielding is required. Therefore the approach of linear-elastic fracture mechanics (LEFM) can be used.

Figure 2.5 shows the coordinate system at the crack tip in which the stress field is described based on the theory of linear elasticity.

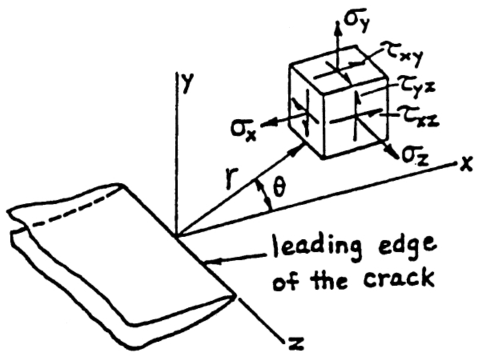

Figure 2.5 Coordinate system at the crack tip, taken from Tada [Tada et al. 2000].

The stress field in the vicinity of the crack tip for mode I loading can be expressed as an infinite series according to Williams [Williams 1957]. This so called Williams Expansion regarding to the coordinate system in figure 2.5 is:

$$\sigma_{ij}(r,\theta) = A_1 r^{-1/2} f_{ij}^1(\theta) + A_2 f_{ij}^2(\theta) + A_3 r^{1/2} f_{ij}^3(\theta) + ..., \tag{2.1}$$

where f_{ij}^n are universal functions and A_1 is identified as the stress intensity factor of displacement mode I K_I . Higher order terms are omitted because in LEFM it is assumed that the stress intensity factor is the only parameter which dominates the deformation state in the vicinity of the crack tip [Sherry et al. 1995]. The Williams Expansion can then be written as

$$
\begin{aligned}
\sigma_x &= \frac{K_I}{\sqrt{2\pi r}} cos\frac{\theta}{2}\left[1 - sin\frac{\theta}{2} sin\frac{3\theta}{2}\right] + ...,\\
\sigma_y &= \frac{K_I}{\sqrt{2\pi r}} cos\frac{\theta}{2}\left[1 + sin\frac{\theta}{2} sin\frac{3\theta}{2}\right] + ...,\\
\tau_{xy} &= \frac{K_I}{\sqrt{2\pi r}} cos\frac{\theta}{2} sin\frac{\theta}{2} cos\frac{3\theta}{2} + ...,\\
\sigma_z &= 0 \quad \text{(plane stress)},\\
\sigma_z &= \nu(\sigma_x + \sigma_x) \quad \text{(plane strain; } \epsilon_z = 0\text{)},\\
\tau_{yz} &= \tau_{zx} = 0,
\end{aligned}
\tag{2.2}
$$

where $\sigma_{x/y/z}$ are the stresses in x-, y-, z-direction, $\tau_{xy/yz/zx}$ are the shear stresses in xy-, yz-, zx-plane and r as well as θ are polar coordinates in the xy-plane. The stress σ_z is assumed zero when the thickness of the member is relatively thin in the z-direction (plane stress). If this is not the case and the member is relatively thick the plane strain assumption should be used where the strain in z-direction $\epsilon_z = 0$. Then σ_z depends on the Poisson's ratio ν.

K_I describes the magnitude of the stress field and is defined as

$$K_I = \lim_{r,\theta \to 0} (\sigma_y \sqrt{2\pi r}). \tag{2.3}$$

A general expression is

$$K_I = F S_g \sqrt{\pi a} \qquad [\mathrm{MPa}\sqrt{\mathrm{m}}], \tag{2.4}$$

where S_g is the gross section nominal stress which characterizes the applied load. This stress is based on the member without a crack. F is a dimensionless function by which different geometric shapes are considered as well as the loading conditions. This function F is also dependent on the ratio $\alpha = a/b$, where a is the crack length and b is a geometric distance which varies between different geometric shapes. If the ratio of a member is $\alpha = a/b = 1$ it is completely cracked. In figure 2.6 (a) b is shown for three different specimens and the corresponding geometry functions F which are given in Dowling [Dowling 1998] are plotted over the ratio α for plates under tension. The center cracked specimen, curve (a), corresponds to

$$F = \frac{1 - 0.5\alpha + 0.32\alpha^2}{\sqrt{1-\alpha}}. \tag{2.5}$$

In ASTM [ASTM 2015] the used geometry function for the middle tension specimen M(T) is

$$F = \sqrt{\sec \frac{\pi a}{2b}}. \tag{2.6}$$

The stress intensity factor K_I can also be determined with the applied loads as follows:

$$K_I = F_P \frac{P}{t\sqrt{b}}, \tag{2.7}$$

where F_P is a new geometry function, P the applied load, t the thickness of the member and b is the same value used for the ration α. In figure 2.6 (b) F_P for the compact tension specimen C(T) is shown over the ratio α.

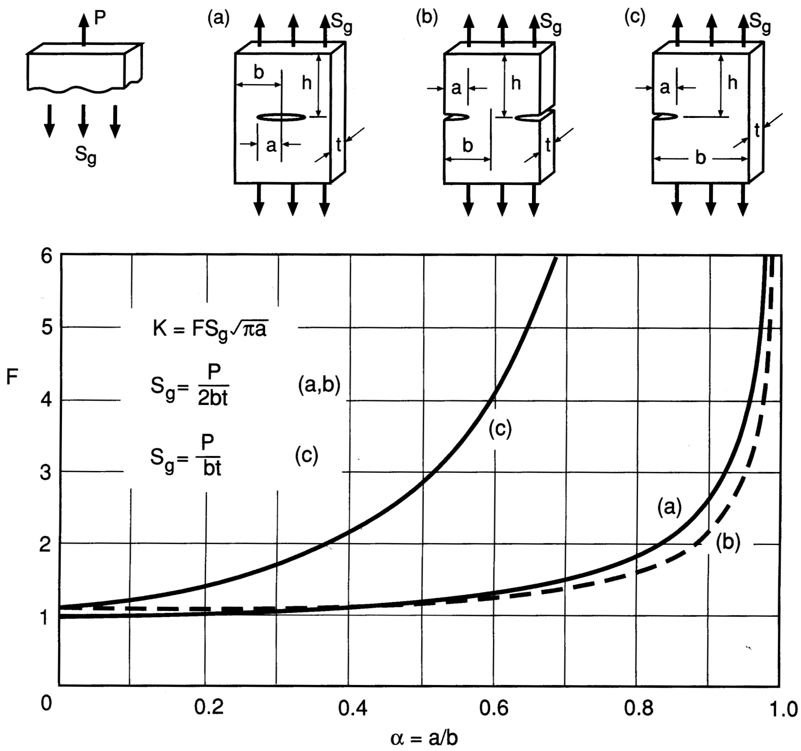

(a) Geometry function F

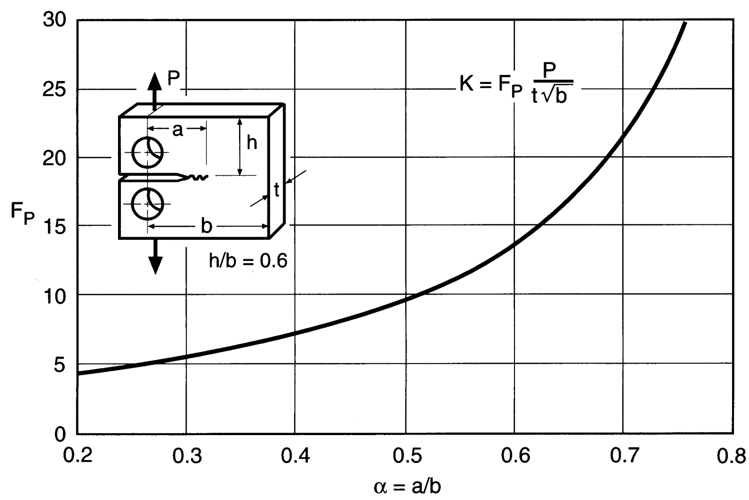

(b) Geometry function F_P for the compact (tension) specimen C(T)

Figure 2.6 Geometry functions F for plates under tension and F_P for the C(T) specimen, taken from Dowling [Dowling 1998].

The geometry function F_P for the C(T) specimen is calculated with the following equation given by Srawley [Srawley 1976]

$$F_P = \frac{2+\alpha}{(1-\alpha)^{3/2}}(0.886 + 4.64\alpha - 13.32\alpha^2 + 14.72\alpha^3 - 5.6\alpha^4), \qquad \alpha \geq 0.2. \tag{2.8}$$

If the stress intensity factor exceeds a critical value K_c, called fracture toughness, brittle fracture can occur. This value is a material property which depends among others on the geometry and temperature.

2.1.4 Plastic zone size and K-field

In linear-elastic fracture mechanics the nonlinear plastic zone is assumed to be small compared to the elastic stress field around the crack tip which is called the K-field. The size of the plastic zone can be estimated for plane stress from equation (2.2). For $\theta = 0$ these equations become

$$\begin{gathered} \sigma_x = \sigma_y = \frac{K_I}{\sqrt{2\pi r}}, \\ \sigma_z = \tau_{xy} = \tau_{yz} = \tau_{zx} = 0. \end{gathered} \tag{2.9}$$

Yielding takes place when $\sigma_x = \sigma_y = \sigma_0$ where σ_0 is the yield strength of the material. Solving the above equation for r and using σ_0 the following expression is obtained

$$r_{0\sigma} = \frac{1}{2\pi}\left(\frac{K_I}{\sigma_0}\right)^2. \tag{2.10}$$

The final width of the plastic zone is

$$2r_{0\sigma} = \frac{1}{\pi}\left(\frac{K_I}{\sigma_0}\right)^2, \tag{2.11}$$

because it is assumed that the plastic zone size is twice $r_{0\sigma}$. The reason for that is that the stresses in the plastic zone are lower than the stresses from the elastic field. The stress is redistributed due to large deformations, therefore the plastic zone increases. In figure 2.7 the estimation of the plastic zone size is shown.

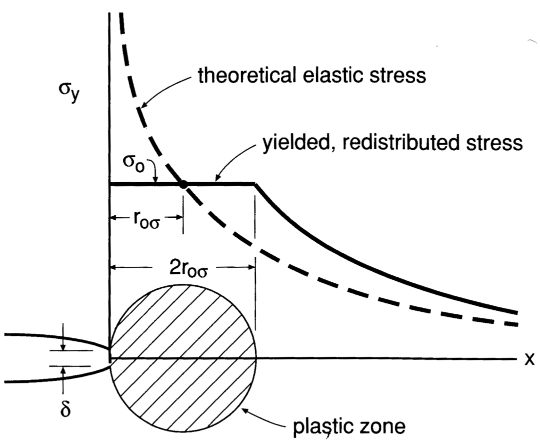

Figure 2.7 Plastic zone size, taken from Dowling [Dowling 1998].

Around the small plastic zone the K-field is situated, see figure 2.8. This field characterizes the crack situation. The size of the plastic zone is small enough if the following limits of LEFM are satisfied

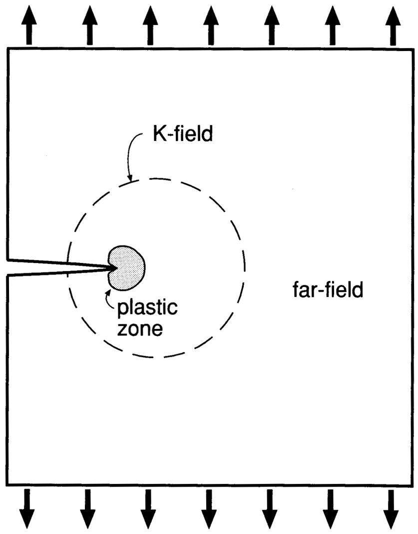

Figure 2.8 K-field, taken from Dowling [Dowling 1998].

$$a, (b-a), h \geq \frac{4}{\pi}\left(\frac{K_I}{\sigma_0}\right)^2, \tag{2.12}$$

where a is the crack length, $(b-a)$ is the uncracked ligament and h is half of the height of the member. The measurements $a, (b-a)$ and h are shown in figure 2.9.

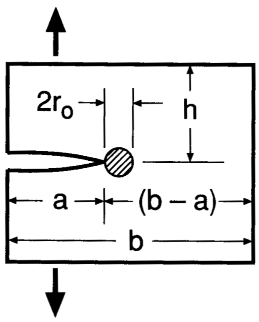

Figure 2.9 Measurements for LEFM limits, taken from Dowling [Dowling 1998].

2.2 Fatigue crack growth

In this part the importance of fatigue crack growth analysis in engineering is discussed. Different types of cyclic loading are shown, the fatigue crack growth rate over the stress intensity factor range is depicted schematically and the three different fatigue crack growth regions are explained. The constraint effect that has a significant influence on the stress-strain state in the vicinity of a crack tip is elucidated as well as fatigue crack growth behaviour at low temperatures.

2.2.1 Introduction

If structural components of for example aircrafts, rail vehicles, wind turbines or ships are exposed to cyclic loading microscopic damage can occur even below the material's ultimate strength. This damage can develop into a macroscopic crack and grow until brittle fracture. This behaviour is called fatigue.

In engineering failure due to fatigue is of major interest. A lot of structural components contain cracks after a certain amount of time in service. These cracks become dangerous if they become too large. Therefore analysis of crack growth life of components are made and periodical inspections are scheduled and performed to find cracks larger than a minimum detectable crack length. These larger cracks can then be repaired or the components with these cracks are replaced. For this purpose the crack growth behavior of a material has to be known. Therefore crack growth rate curves are determined by experiments which can then be used for structural components [Dowling 1998].

2.2.2 Cyclic loading

Cyclic loading with constant amplitude stressing is very common and means that the loading varies between a constant maximum and minimum stress. Three different types of constant amplitude stressing are distinguished. The first loading case is completely reversed stressing where the mean stress $\sigma_m = 0$. The second loading case is zero-to-tension stressing where $\sigma_{min} = 0$, and in the third case neither σ_m nor σ_{min} are equal to zero. In figure 2.10 these three types are depicted.

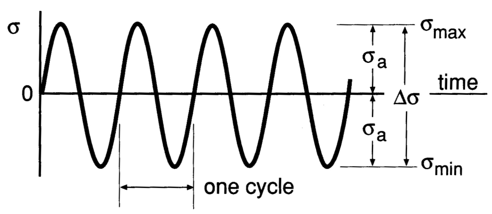

(a) Completely reversed stressing

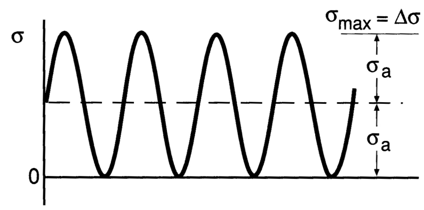

(b) Zero-to-tension stressing

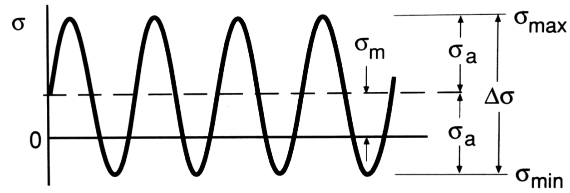

(c) Nonzero mean stress σ_m

Figure 2.10 Three different types of constant amplitude stressing, taken from Dowling [Dowling 1998].

The difference between maximum and minimum stress is called the stress range $\Delta\sigma$ and is defined as

$$\Delta\sigma = \sigma_{max} - \sigma_{min}. \tag{2.13}$$

The stress amplitude σ_a is then half of the stress range

$$\sigma_a = \frac{\Delta\sigma}{2}. \tag{2.14}$$

The mean stress σ_m which is the average between the maximum and the minimum stress is defined as

$$\sigma_m = \frac{\sigma_{max} + \sigma_{min}}{2}. \tag{2.15}$$

Often the stress ratio R is of interest which is expressed as

$$R = \frac{\sigma_{min}}{\sigma_{max}}. \tag{2.16}$$

2.2.3 Fatigue crack growth behaviour

During a considered number of loading cycles ΔN applied to a specimen a crack grows by Δa. If N and a are plotted on the x-axis and y-axis, respectively, a crack growth curve is obtained. In figure 2.11 an exemplary graph of a crack growth curve is shown for a high and low stress level. The slope of the crack growth curve at a particular point is the fatigue crack growth rate and is expressed by $^{\Delta a}/_{\Delta N}$. For small intervalls the derivative is used and the fatigue crack growth rate is expressed as $^{da}/_{dN}$. For an increased stress level the fatigue crack growth rate increases. The crack growth rate can then be plotted over the crack length, as in figure 2.12, where two different stress levels are shown. It is shown that the stress levels are overlapping in a certain range which means that similar crack growth rates are obtained at different crack lengths. This behaviour had led to a similarity principle which is based on the stress intensity factor K [Schijve 2008].

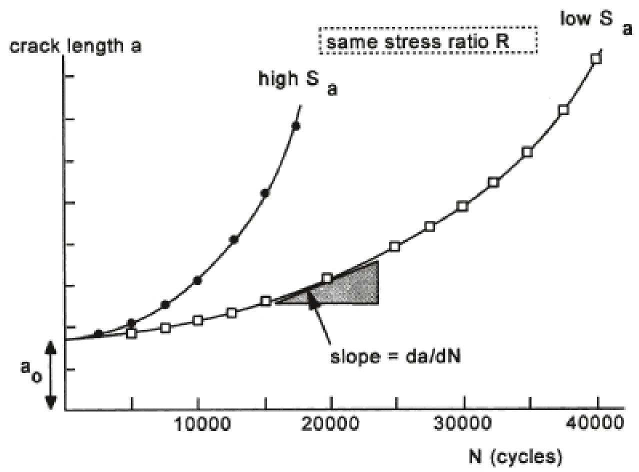

Figure 2.11 Crack length a over number of cycles N at two different stress levels, taken from Schijve [Schijve 2008].

If a cyclic load with constant amplitude is applied to a specimen the gross section stress as well as the applied load switches between its constant maximum S_{max}, P_{max} and minimum S_{min}, P_{min}. The range between maximum and minimum stress load is expressed as $\Delta S = S_{max} - S_{min}$ and $\Delta P = P_{max} - P_{min}$. Thus the stress intensity factor varies between K_{max} and K_{min}. With equation (2.4) the stress intensity factor range ΔK is introduced which is

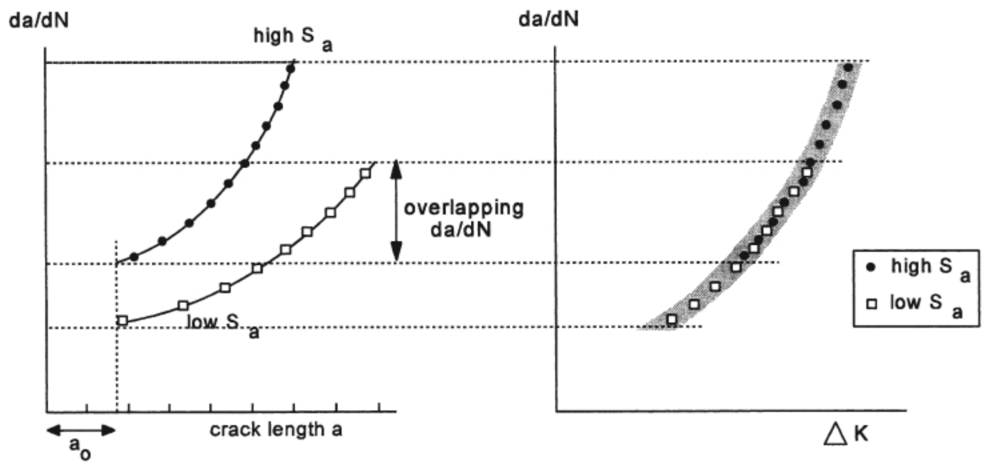

Figure 2.12 Crack growth rate da/dN over crack length and stress intensity factor range ΔK for low and high stress level, taken from Schijve [Schijve 2008].

$$\Delta K = K_{max} - K_{min} = F \Delta S \sqrt{\pi a}. \tag{2.17}$$

The stress intensity factor range ΔK can also be calculated with the following alternate equation regarding the applied load P

$$\Delta K = F_P \frac{\Delta P}{t\sqrt{b}}. \tag{2.18}$$

Therefore the stress ratio R can be expressed as

$$R = \frac{K_{min}}{K_{max}} = \frac{P_{min}}{P_{max}}. \tag{2.19}$$

The similarity principle means that if the same K_{max} and K_{min} are applied to a specimen and for instance a structural component then the fatigue process at the crack tip should be the same. Thus the crack propagation should be the same as well as the crack growth rate. This implies that the fatigue crack growth rate is a function of the stress intensity factor range where the shape of the specimen or the component is accounted for by the geometry factor.

In figure 2.12 the fatigue crack growth rate da/dN versus crack length for two stress levels with the same R is depicted qualitatively in the left picture. In the right picture the fatigue crack growth rate is plotted versus the stress intensity factor range ΔK where the two stress levels overlap in a certain region. This relationship between the crack growth rate and the stress intensity factor range is commonly used to describe the behavior of crack growth for a given material. With such curves obtained from experiments with specimen geometries like the M(T) or C(T) specimen the crack growth rate in a real component can be predicted due to the similarity principle by calculating the stress intensity factor range of the component. Hence a crack length over cycles curve can be determined for the structural component and a life estimation can be made and inspection intervalls set [Schijve 2008] [Dowling 1998]. Figure 2.13 shows the aforementioned steps of obtaining fatigue crack growth data and their engineering application in a qualitative way.

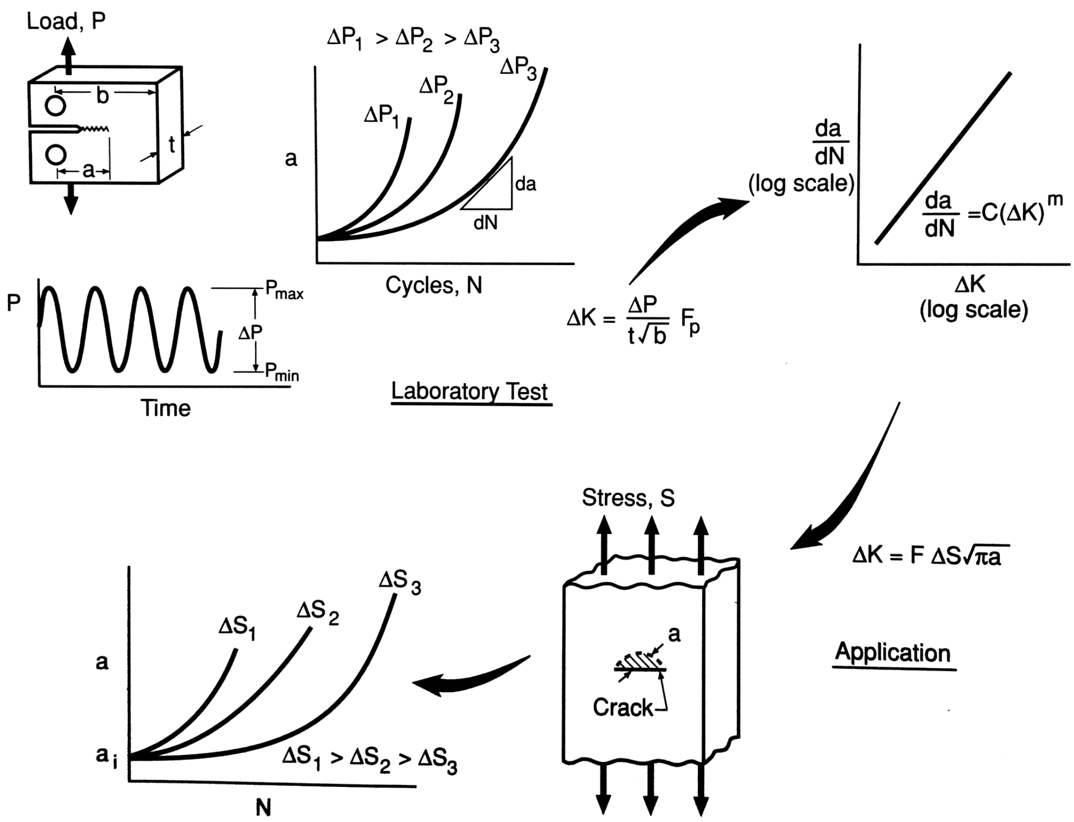

Figure 2.13 Qualitative steps how to obtain grack growth rate curves from experiments and how to use it for an engineering application, taken from Dowling [Dowling 1998].

Fatigue crack growth regions

If ${}^{da}/_{dN}$ and ΔK, which are obtained by experiments, are plotted on a double logarithmic scale the data can be fitted with a function, see figure 2.14. This function can be divided into three different regions I, II and III. Region I is called the threshold ΔK-region. In this region at low crack growth rates the curve is approaching the fatigue crack growth threshold ΔK_{th} which is a vertical asymptote. Below this value no crack propagation occurs. Region III is the stable tearing crack growth region where the crack growth rate increases rapidly due to unstable crack growth until fracture. The curve approaches the maximum stress intensity factor K_{max} which is equal to the fracture toughness K_C. In engineering region III is of lower interest because a components crack growth life spent in this region is very short. In region II, the Paris-ΔK-region, the correlation between ΔK and ${}^{da}/_{dN}$ can be described by the Paris equation which reads as follows:

$$\frac{da}{dN} = C(\Delta K)^m, \tag{2.20}$$

where m is the slope of the curve and C is a constant with unit $\frac{{}^{\mathrm{mm}}/_{\mathrm{cycle}}}{(\mathrm{MPa}\sqrt{\mathrm{m}})^m}$. The unit of C depends on the units of ${}^{da}/_{dN}$ and ΔK. Both, C and m are material constants. The Paris equation yields to the following linear function in the double logarithmic plot

$$\log\left(\frac{da}{dN}\right) = \log(C) + m\log(\Delta K). \tag{2.21}$$

Knowing C and m the number of cycles needed to grow a crack from the initial length to its final length can be determined by integrating equation (2.20).

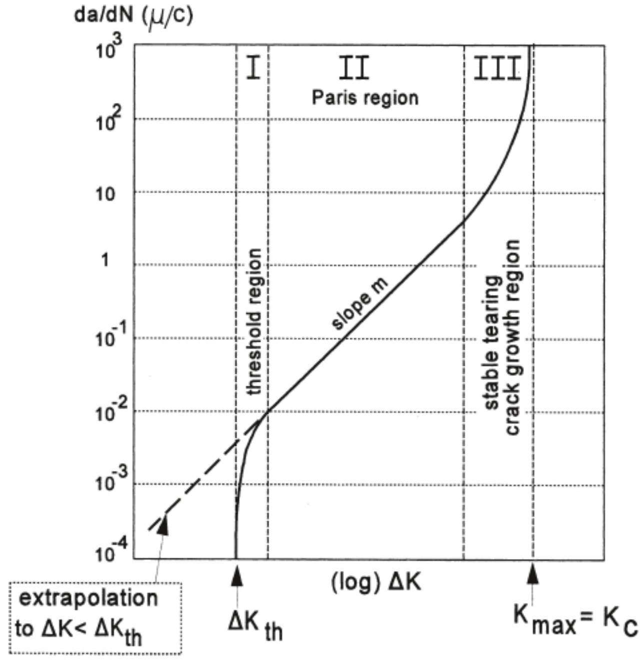

Figure 2.14 Three regions of the fatigue crack growth rate curve, taken from Schijve [Schijve 2008].

Figure 2.15 shows region II and III of fatigue crack growth on a fracture surface. There the tensile mode corresponds to region II of the crack growth rate curve and the shear mode corresponds to region III.

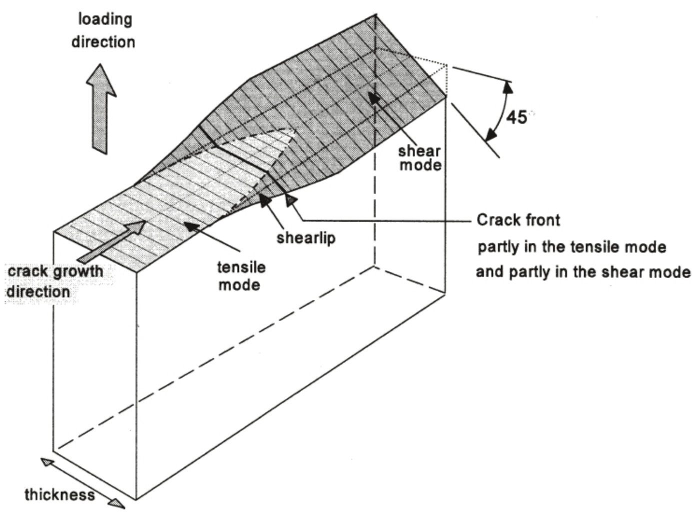

Figure 2.15 Region II and III of the fatigue crack growth on a fracture surface, taken from Schijve [Schijve 2008].

2.2.4 Constraint effect

In conventional fatigue crack growth rate tests the obtained crack growth rate curves are regarded as material specific data. Engineering analysis uses the empirically obtained material constants C and m of the Paris equation (2.20) as well as the stress intensity factor range ΔK [Varfolomeev et al. 2010]. This data is given without any specification of the used test specimen geometry and thus without information about the level of constraint near the crack tip. But there are various investigations where differences in fatigue crack growth rate have been noted in different specimen geometries of the same material [Varfolomeev et al. 2011], [Seitl et al. 2008] and [Hutař et al. 2006]. Therefore further information is needed to describe the effect of the structural and loading configuration on the crack tip constraint [Sherry et al. 1995].

Different approaches exist to account for the constraint effect. The approach used in this thesis is mainly based on the findings of Sherry [Sherry et al. 1995] and Hutař [Hutař et al. 2006] and is explained in detail in the following.

In linear elastic fracture mechanics one parameter is sufficient to describe the stress state in the vicinity of the crack tip which is the stress intensity factor K. But there is another parameter that influences the elastic stress field, which is the first non-singular term in the Williams expansion A_2, see equation (2.1), [Larsson and Carlsson 1973]. This non-singular term only occurs in the x-direction and is called elastic $T_{stress,x}$ which leads to the following expression of the elastic stress field in the vicinity of the crack tip for plane stress, according to Lu [Lu and Meshii 2015]

$$\begin{aligned}
\sigma_x &= \frac{K_I}{\sqrt{2\pi r}} cos\frac{\theta}{2}\left[1 - sin\frac{\theta}{2} sin\frac{3\theta}{2}\right] + T_{Stress,x},\\
\sigma_y &= \frac{K_I}{\sqrt{2\pi r}} cos\frac{\theta}{2}\left[1 + sin\frac{\theta}{2} sin\frac{3\theta}{2}\right] + 0,\\
\tau_{xy} &= \frac{K_I}{\sqrt{2\pi r}} cos\frac{\theta}{2} sin\frac{\theta}{2} cos\frac{3\theta}{2} + 0.
\end{aligned} \tag{2.22}$$

In the following the $T_{Stress,x}$ is written without the subscript x. The T_{Stress} can be expressed according to Leevers [Leevers and Radon 1982] as

$$T_{stress} = \frac{BK_I}{\sqrt{\pi a}}, \tag{2.23}$$

where B is a non-dimensional parameter, called biaxiality factor, which depends on the geometrical shape of the used specimen as well as on the loading condition [Sherry et al. 1995]. Substituting K_I with equation (2.4) the T_{stress} reads

$$T_{stress} = BF\sigma, \tag{2.24}$$

where $\sigma = S_g$.

Rearranging equation (2.23) the biaxiality factor B reads as follows

$$B = \frac{T_{Stress}\sqrt{\pi a}}{K_I}, \tag{2.25}$$

which normalizes the T_{Stress}. B can be used in addition to the stress intensity factor to describe the stress field in the vicinity of the crack tip [Leevers and Radon 1982].

In Sherry [Sherry et al. 1995] the biaxiality factor is calculated with a polynomial of fourth order in the form

$$B = B0 + B1\left(\frac{a}{W}\right) + B2\left(\frac{a}{W}\right)^2 + B3\left(\frac{a}{W}\right)^3 + B4\left(\frac{a}{W}\right)^4. \tag{2.26}$$

The polynomial constants for the biaxiality factor $B0$ to $B4$ are given for three different calculating methods for the M(T) and C(T) specimen, respectively. In this thesis these methods are called a), b) and c) and are not further explained, for detailed information see [Sherry et al. 1995]. In table 2.1 these constants are listed for the M(T) specimen and in table 2.2 for the C(T) specimen. B is only applicable between $0.1 \leq {}^a/_W \leq 0.6$ for the M(T) specimen and $0.2 \leq {}^a/_W \leq 0.7$ for the C(T) specimen. In figure 2.16 and 2.17 the biaxiality factor B is shown for the M(T) and C(T) specimen, respectively, for three different calculating methods.

Table 2.1 Polynomial constants for B for the M(T) specimen, taken from Sherry [Sherry et al. 1995].

Method	B0	B1	B2	B3	B4
a	-1.004	0.248	-2.39	5.532	-4.069
b	-0.991	0.163	-1.866	4.579	-3.542
c	-1.044	0.085	-0.150	–	–

Table 2.2 Polynomial constants for B for the C(T) specimen, taken from Sherry [Sherry et al. 1995].

Method	B0	B1	B2	B3	B4
a	-0.513	1.708	13.404	-39.750	29.583
b	-0.058	-0.276	12.790	-27.875	17.292
c	- 0.353	-1.702	23.667	-47.33	28.333

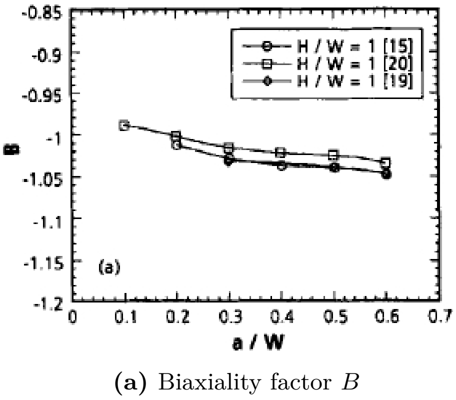

(a) Biaxiality factor B

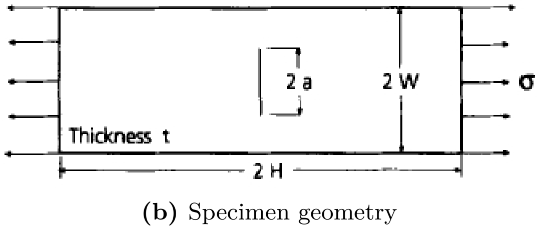

(b) Specimen geometry

Figure 2.16 Biaxiality factor B for the M(T) specimen, based on Sherry [Sherry et al. 1995].

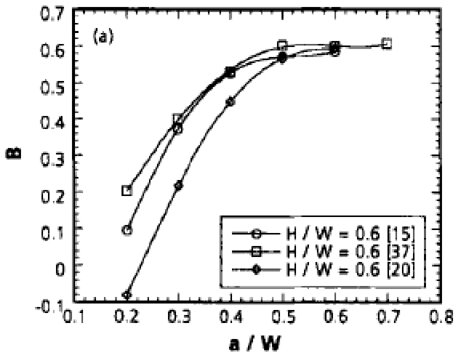

(a) Biaxiality factor B

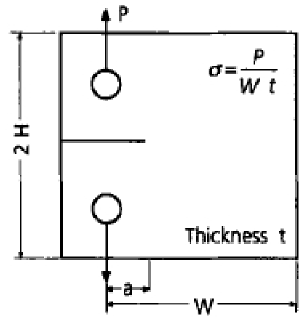

(b) Specimen geometry

Figure 2.17 Biaxiality factor B for the C(T) specimen, based on Sherry [Sherry et al. 1995].

The T_{Stress}, in form of the biaxiality factor B, can be used to describe the dependency of the crack growth rate upon the crack tip constraint [Varfolomeev et al. 2011]. Due to the low level of constraint of the M(T) specimen the biaxiality factor (T_{Stress}) is negative. The C(T) specimen has a high level of constraint which correlates with a positive biaxiality factor (T_{Stress}), see figure 2.16 and 2.17.

Hutař [Hutař et al. 2006] uses a phenomenological approach to account for the specimen geometry which is based on two-parameter linear elastic fracture mechanics where the fatigue crack growth rates for two different specimen geometries are correlated. The constraint level is quantified by the T_{stress}, thus the fatigue propagation rate is expressed in terms of K and T_{stress}. The size of the plastic zone depends on the stress intensity factor and the level of constraint. Thus in this approach the Paris equation (2.20) is rewritten using the effective stress intensity factor K^{eff} which is defined as

$$K^{eff}(T_{stress}) = \lambda \left({}^{T_{Stress}}/_{\sigma_0}\right) K(T_{Stress} = 0), \tag{2.27}$$

and the function $\lambda({}^{T_{Stress}}/_{\sigma_0})$ which relates the plastic zone size with the constraint level as

$$\lambda({}^{T_{Stress}}/_{\sigma_0}) = 1 - 0.33 \left(\frac{T_{Stress}}{\sigma_0}\right) + 0.66 \left(\frac{T_{Stress}}{\sigma_0}\right)^2 - 0.445 \left(\frac{T_{Stress}}{\sigma_0}\right)^3. \tag{2.28}$$

Thus $K^{eff}(T_{stress})$ takes into account the level of applied stress, the constraint level and the local plasticity at the crack tip.

The modified Paris equation which accounts for the constraint effect on fatigue propagation rate then reads

$$\frac{da}{dN} = C[\lambda({}^{T_{Stress}}/_{\sigma_0})K]^m, \tag{2.29}$$

where C and m are material constants at $T_{Stress} = 0$.

The experimental data obtained in Hutař [Hutař et al. 2006] for fatigue crack growth rate versus the stress intensity factor range ΔK for the M(T) and C(T) specimens is shown in figure 2.18 a) and the fatigue crack growth rate versus the effective stress intensity factor range ΔK^{eff} for these specimens is shown in figure 2.18 b). This data is fitted with the modified Paris equation. This curve is now a material curve independent of the specimen geometry.

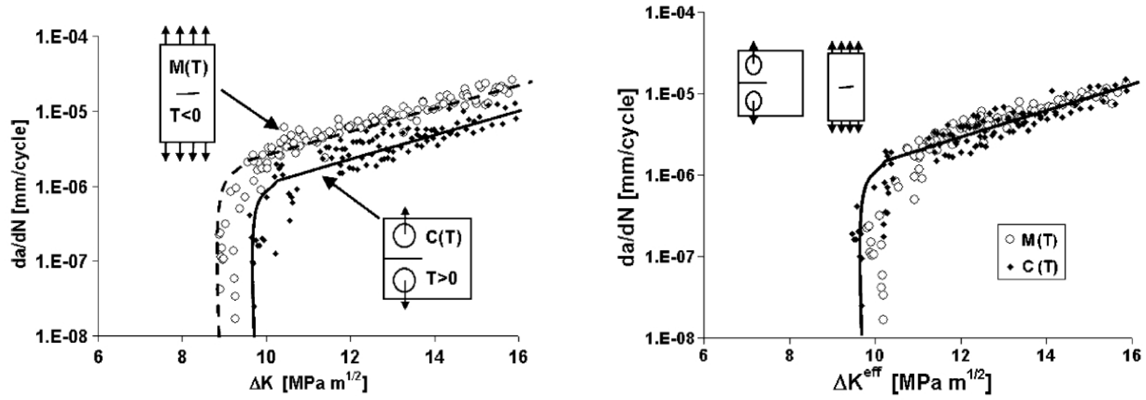

(a) Fatigue crack growth rate versus stress intensity factor range for the M(T) and C(T) specimen

(b) Fatigue crack growth rate versus effective stress intensity factor range ΔK^{eff}

Figure 2.18 Fatigue crack growth rate versus stress intensity factor range for the M(T) and C(T) specimen and fatigue crack growth rate versus effective stress intensity factor range ΔK^{eff}, taken from Hutař [Hutař et al. 2006].

2.2.5 Fatigue at low temperatures

Considering ferritic steel (body-centered cubic (bcc) crystal structure) there is a transition from ductile fracture mode at high temperatures to brittle fracture mode at low temperatures. The temperature where this transition occurs can be obtained by different fracture toughness tests. In figure 2.19 the ductile to brittle transition curve is shown for two different fracture toughness test methods. There is a shift of temperature between these two methods due to the dependency of the ductile to brittle transition temperature on different factors i.e. the size of the specimen, the sharpness of the crack and the constraint ect. [Walters et al. 2016]. Hence, the transition temperature is not a material constant.

Any of the generally used toughness test methods are accepted to obtain the transition temperature due to the lack of a general definition. However, the transition temperature is described by common values for example the Fracture Appearance Transition Temperature (FATT), the temperature T_{27J} or T_0.

In maritime and offshore industry the temperature T_{27J} is most commonly used.

Fatigue Ductile-Brittle Transition (FDBT)

For fatigue at low temperatures a similar effect to the fracture ductile to brittle transition is found for ferritic steels which is called Fatigue Ductile-Brittle Transition (FDBT). Here the transition temperature is called Fatigue Transition Temperature (FTT).

At lower temperatures the fatigue crack growth rate da/dN decreases until FTT is reached. At temperatures below FTT a higher slope in the fatigue crack growth rate versus stress intensity factor range curve is induced. Thus da/dN may be lower for low ΔK values and higher for high ΔK values compared to room temperature [Walters et al. 2016].

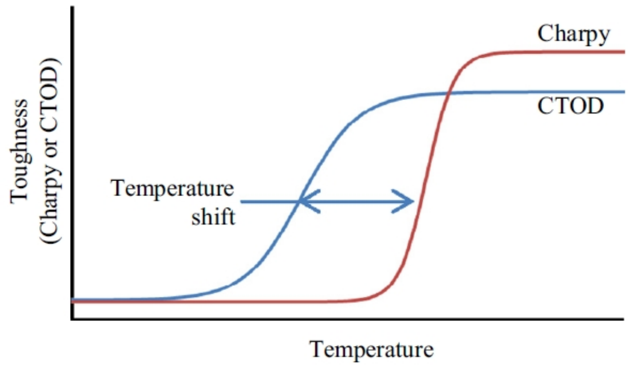

Figure 2.19 Ductile to brittle transition curve obtained by two different fracture toughness test methods, taken from Walters [Walters et al. 2016].

Figure 2.20 shows qualitatively the effect of low temperatures on the fatigue crack growth rate curve. The red curve shows a bcc steel at a temperature below FTT and the black curve shows the fatigue crack growth behavior at room temperature. The curve below FTT has an increased fatigue crack growth threshold value, the fracture toughness is lower which reduces fatigue propagation life and the Paris exponent m is higher compared to room temperature. The blue curve represents an austenitic steel at low temperature where no FDBT occurs. For these metals low temperature has a positive effect because with decreasing temperature ΔK_{th} increases and the fatigue crack growth rate decreases [Walters et al. 2016].

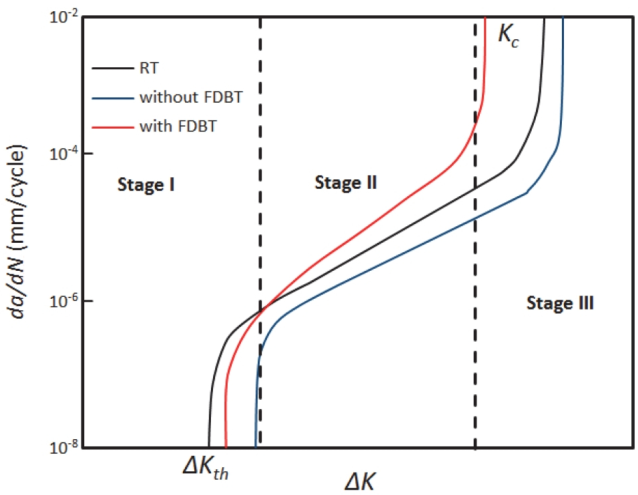

Figure 2.20 Effect of low temperature on the fatigue crack growth rate curve for bcc (red) steels and for austenitic steels (blue) compared to room temperature (black), taken from Alvaro [Alvaro et al. 2014].

Due to the increasing interest of the maritime industry in the arctic regions the interest for ferritic steel at low temperatures is increasing. Thus it is important to know how the fracture ductile to brittle transition can be correctly related to the FDBT and how the fracture toughness is influenced by low temperatures as well as the test specimen geometry.

2.3 Direct current potential drop (DCPD) method

At the beginning of this section the principle of the direct current potential drop method is explained as well as the calibration of the DCPD method. The current input and the potential measurement lead placements are discussed as well as potential problems of the DCPD method.

2.3.1 Principle

The direct current potential drop (DCPD) method is a method used for the determination of crack growth based on electric potential measurements.

A constant current I is applied to a specimen, thus an electrical field is generated. The electrical potential field of the specimen is disturbed by any occuring discontinuity. The shape and size of the discontinuity is directly correlated with the magnitude of the disturbance in the electrical potential field. So with crack propagation the electrical potential U changes. Due to the crack growth the uncracked ligament of the specimen is reduced resulting in an increase of electrical resistance R of the specimen. Thus the increasing potential difference (potential drop/voltage drop) U between two special points across the crack is measured [Aronson and Ritchie 1979]. With Ohm's law the electrical resistance and the electrical potential are related as follows

$$U = R \cdot I = const. \tag{2.30}$$

In general a calibration curve is created with the potential difference readings. This calibration curve correlates the measured potential difference U with the crack length a. The crack length is obtained by for example visual crack length measurements as beach marks or by crack detection gauges. A detailed explanation for the calibration curve is given in section 2.3.2.

In ASTM [ASTM 2015] a schematic diagram of the DCPD system is given, see figure 2.21. The system includes a test specimen, a DC current source, a voltmeter and a reading device. Normally the voltage output is in the millivolt region, therefore an amplifier can be used.

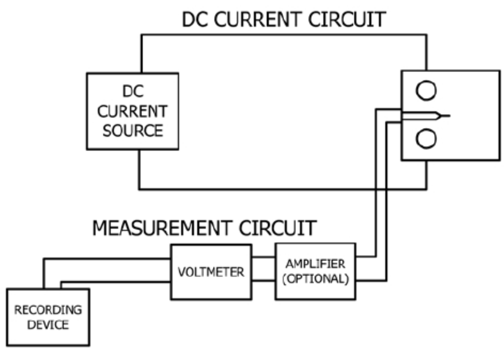

Figure 2.21 Schematic Diagram of the DCPD system, taken from ASTM [ASTM 2015].

2.3.2 Calibration of the DCPD method

For the DCPD method a correlation is needed to determine the crack length from the potential drop measurments. Therefore a calibration curve for each specimen geometry is created which provides this correlation between the potential drop and crack length. Several correlation methods exist, for example finite-element methods, experimental as well as analytical methods

[Hill and Stuart 2012].

Usually a calibration curve is given in the form of U/U_0 versus a/W, where U_0 is a reference potential drop at a reference crack length a_0. Because this ratios are nondimensional, the calibration curve is independent of specimen thickness, magnitude of current input and material properties. They are only a function of specimen and crack geometry as well as of the current input and potential measurement lead positions [Aronson and Ritchie 1979].

In the following sections three calibration methods to correlate the crack length with potential drop readings are introduced which are the analytical Johnson's equation, an optical crack length measurement and crack length measurements with crack detection gauges.

Johnson's equation

An analytical relation for calculating the crack length is the equation by H. H. Johnson, taken from Schwalbe [Schwalbe and Hellmann 1981]

$$\frac{U}{U_0} = \frac{\cosh^{-1}\left[\dfrac{\cosh\left(\dfrac{\pi y}{2W}\right)}{\cos\left(\dfrac{\pi a}{2W}\right)}\right]}{\cosh^{-1}\left[\dfrac{\cosh\left(\dfrac{\pi y}{2W}\right)}{\cos\left(\dfrac{\pi a_0}{2W}\right)}\right]}, \tag{2.31}$$

where U_0 is an initial potential drop at an initial crack length a_0, U is the actual potential drop at the actual crack length a and y is the distance of the voltage measurement lead wire from the crack plane. In equation (2.31) W is half of the width of a center-cracked specimen, thus for the M(T) specimen in ASTM [ASTM 2015] $2W$ is replaced by W, which is then the overall width of the specimen.

Rearranging equation (2.31) the crack length a reads as follows

$$a = \frac{2W}{\pi}\cos^{-1}\left[\frac{\cosh\left(\dfrac{\pi y}{2W}\right)}{\cosh\left(\dfrac{U}{U_0}\cdot\cosh^{-1}\left[\dfrac{\cosh\left(\dfrac{\pi y}{2W}\right)}{\cos\left(\dfrac{\pi a_0}{2W}\right)}\right]\right)}\right]. \tag{2.32}$$

Equation (2.32) does not account for the effect of the notch hole in the M(T) specimen. Therefore, according to Hill [Hill and Stuart 2012] some modifications have to be made. In this case W, which replaces $2W$, is substituted by $W^* = W - 2r$ which is the new specimen width. y is replaced with $y^* = y + r\,(\pi/2 - 1)$ which is the new voltage measurement lead wire location. Rearranging equation (2.32), substituting W and y and solving for the crack length a the modified Johnson's equation reads as follows

$$a_{Jmod} = \frac{W^*}{\pi} \cos^{-1} \left[\frac{\cosh\left(\frac{\pi y^*}{W^*}\right)}{\cosh\left(\frac{U}{U_0} \cdot \cosh^{-1}\left[\frac{\cosh\left(\frac{\pi y^*}{W^*}\right)}{\cos\left(\frac{\pi a_0}{W^*}\right)}\right]\right)} \right]. \tag{2.33}$$

Because the radius of the notch hole is part of the crack length the hole radius has to be added to the crack length of the modified Johnson's equation. The crack length for the M(T) specimen now reads $a_{mod} = a_{Jmod} + r$.

For the C(T) specimen equation (2.32) can be used without modifications.

Visual crack length measurement

With the aid of a second load ratio R beach marks on the fracture surface of the test specimen are created. Both load ratios have the same maximum load where the minimum load for one of the R values is higher. In literature often the load ratios $R = 0$ and $R = 0.5$ or $R = 0.1$ and $R = 0.5$ are used. Each ratio with a constant amplitude is applied for a particular number of loading cycles. Depending on the stress ratio the crack is growing faster or slower. These changes in crack propagation due to load change are visible as beach marks across the fracture plane where the load ratio with the higher minimum load creates a dark band. After the specimen is broken the beach marks are measured. Then the different crack lengths are correlated with the voltage readings resulting in a calibration curve.

Crack length measurement with crack detection gauge

Crack length can also be measured with crack detection gauges. A crack detection gauge is placed in front of the specimen notch and when the crack starts to grow the strands of the crack detection gauge are disconnected at a time with continuing crack growth. After the specimen is broken the time is known when the strands are damaged. Then the potential drop readings can be correlated with the known crack length of the crack detection gauge and a calibration curve is created.

2.3.3 Current input location and potential measurement lead placement

Aronson [Aronson and Ritchie 1979] performed an optimization analysis of the DCPD method. An optimization based on the C(T) specimen is obtained by finding the best locations for the current input and the potential measurement leads. For determination, the four parameters Accuracy, Sensitivity, Reproducibility and Measurability are considered. For those a brief overview is given. For a more detailed explanation see Aronson [Aronson and Ritchie 1979].

Accuracy refers to the accuracy of the calibration curve, thus how good the curve approximates the real relationship between the potential change and the crack length. This is limited by for example temperature variations, crack closure or the resolution of the potential measurement system.

Sensitivity refers to the slope of the calibration curve which should be maximized for better resolution.

Reproducibility is ensured when the potential measurement lead wires are placed at a position where the calibration curve is insensitive to small changes in the wire position.

Measurability means the ability to measure the output voltage signal. The current input and the potential measurement lead wires should be placed in such way that the magnitude of the voltage output is maximized.

In this investigation performed by Aronson and Ritchie two different current input locations on the C(T) specimen, A (top surface) and B (side flanks), were compared, see figure 2.22, with varying potential measurement lead wire locations. In all considered cases the optimum position for the potential measurement leads were found at $x = 2.6\,\text{mm}$ from the centreline of the notch at the top surface. Also very good reproducibility of measurements are given close to the notch in an area of $x < 4\,\text{mm}$ because here the calibration curve is insensitive to small variations in wire position and the magnitude of the voltage output is maximized, see figure 2.23 (a) and (b). There the different potential measurement lead wire positions at the top surface of the C(T) specimen are shown over U/U_0 for different crack length a/W, where U is the potential drop related to the crack length a and U_0 is the reference potential drop related to the initial crack length a_0.

It is found that if the potential measurement lead position is in the recommended area of $x < 4\,\text{mm}$ near the notch the current input positions A and B are equally good. For low resistivity metals the positions of the current input and the potential measurement lead are recommended to be at the top surface of the specimen.

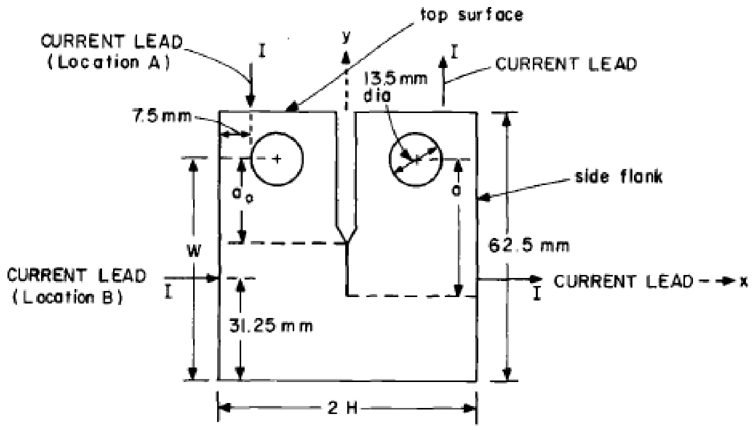

Figure 2.22 Current input locations A (top surface) and B (side flanks) on a C(T) specimen, taken from Aronson [Aronson and Ritchie 1979].

Ritchie [Ritchie et al. 1971] also tried to optimize the current input and potential measurement lead locations for the C(T) specimen. Therefore two current input positions are examined as well as different potential measurement lead positions. The determination of the optimum positions were found with the aid of graphitized electrical analogue paper which show the distribution of the potential field by indicating the equi-potential lines. In figure 2.24 (a) and (b) such equi-potential patterns in an uncracked (left) and cracked (right) C(T) specimen with different current input locations are shown. In figure (a) the current input location is at the top face, in figure (b) the current input location is at the side flank.

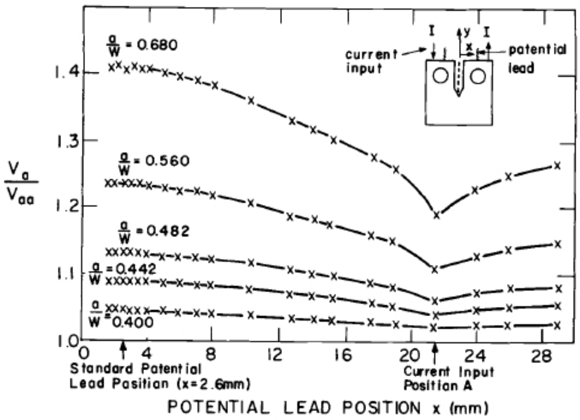

(a) Current input position A (top surface)

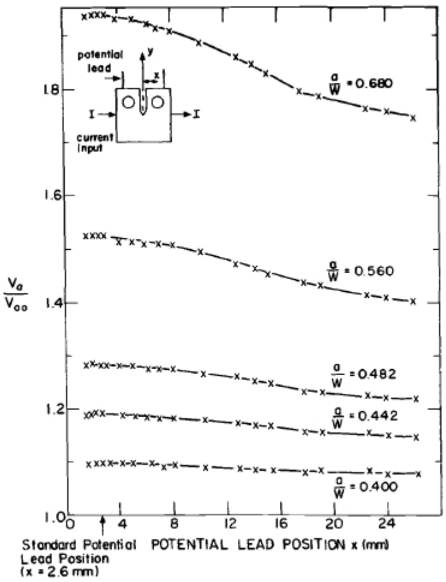

(b) Current input position B (side flanks)

Figure 2.23 Current input positions A (top surface) and B (side flanks) with variation of potential measurement lead position at the top surface of the C(T) specimen. Voltage increase $V_a/V_{a0} = U/U_0$, taken from Aronson [Aronson and Ritchie 1979].

In this investigation performed by Ritchie [Ritchie et al. 1971] it is found that the current input location at the top surface of the C(T) specimen is better due to good sensitivity and the potential measurement lead placement should be at the top surface as close to the notch as possible.

(a) Current input position at the top surface

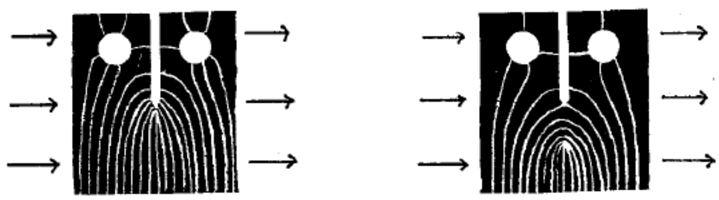

(b) Current input position at the side flanks

Figure 2.24 Equi-potential distribution with two different current input locations on a C(T) specimen for an uncracked (left) and cracked (right) specimen, taken from Ritchie [Ritchie et al. 1971].

In addition to the equi-potential distribution in a cracked and uncracked C(T) specimen the equi-potential fields for a center cracked and uncracked specimen are obtained in Anctil [Anctil et al. 1964], see figure 2.25. The position of the potential measurement leads, marked with an x, are situated in an area where the potential is less sensitive to the exact position of the wires as well as near the crack. The position of the current leads are marked with solid circles.

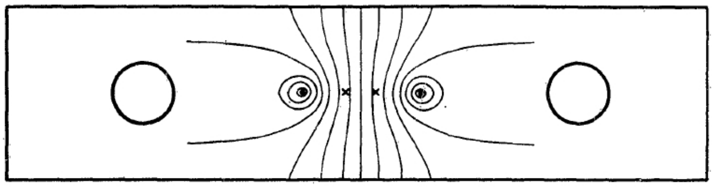

(a) Uncracked specimen

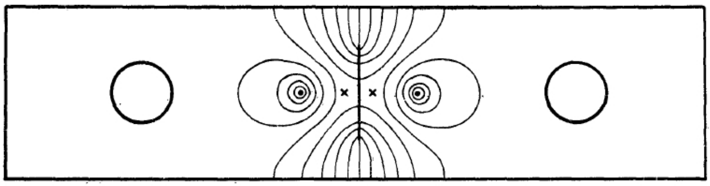

(b) Center cracked specimen

Figure 2.25 Equi-potential field for an uncracked and center cracked M(T) specimen, taken from Anctil [Anctil et al. 1964].

2.3.4 Problems using the DCPD method

According to Hartmann [Hartmann and Johnson 1987] there are three main crack-length-measurement errors using the DCPD method. These errors which are thermoelectric effects, crack closure and material-resistivity changes are explained in the next sections. Another important issue is the electrical isolation.

Thermoelectric effects

According to Pollock [Pollock 1985] two conducting elements at different temperatures (thermoelements) cause a thermoelectric circuit, so an electromotive force (emf) is produced. Thus thermal energy is converted into electrical energy. This is called a thermocouple. This effect causes additional potentials which occur in the potential readings.

To minimize the thermoelectric effect Hartmann [Hartmann and Johnson 1987] recommend to eliminate all temperature differences between the used measurement points as well as to carefully choose the right lead wire material.

ASTM [ASTM 2015] recommends to account for this effect by either measuring the potential difference with and without the current and subtracting these values or by measuring the potential difference while changing the flow direction of the current.

Crack closure

During the unloading part of a cycle the crack at the tip may already be closed even if the tension force is not yet zero. Thus contact can occur between the fracture surfaces of the specimen which would lead to incorrect voltage measurements. According to Hartmann [Hartmann and Johnson 1987] the crack closure effect can be eliminated by taking the voltage readings near the maximum load where the crack mouth is open.

Material-resistivity changes

Material-resistivity is a function of temperature, thus the resistivity changes if the specimen temperature changes. According to ASTM [ASTM 2015] a temperature change of 1 °C induces a change in the voltage reading of a few μV. Specimen heating can occur due to high current magnitude because of according to Aronson [Aronson and Ritchie 1979] for instance the contact resistance at the current input positions.

To measure the changes in material-resistivity Hartmann [Hartmann and Johnson 1987] recommend a second set of potential leads placed within the current flow field. They should be placed in such way that the field strength is not a function of the crack length. ASTM [ASTM 2015] recommends in addition to a second set of lead wires on the test specimen a reference specimen which is powered by the same electrical current source as the test specimen. The crack growth voltage reading has to be divided by the ratio of the voltage reading of the reference probe and the initial reference voltage reading.

Accounting for the specimen heating can increase the crack size resolution.

Isolation

According to ASTM [ASTM 2015] it is important that no additional electric circuit through the test frame occurs. Therefore the specimen and the test frame have to be isolated.

2.4 Objective of the work

Several studies have shown an influence of the test specimen geometry on crack growth behaviour in fatigue crack growth testing. In this thesis experiments are prepared and performed to confirm the existence of said influence and to use the obtained information in view of reliable life estimations of structural components.

To obtain fatigue crack growth data experiments are conducted with specimens of the same material in different geometrical shapes. The used geometries are the middle tension specimen M(T) and the compact (tension) specimen C(T) given in ASTM [ASTM 2015]. The tests are conducted with a resonant testing machine using the direct current potential drop (DCPD) method to relate the crack lengths to normalised voltage drop readings.

The preparation of the tests includes the design of the C(T) specimen as well as the associated clevis and pin assembly necessary for the experimental setup. During construction special requirements are considered, for instance the clevises and specimen arrangement have a restricted length due to an already existing cold chamber which will be used in further studies. All positions of current input and potential measurement lead wires regarding the DCPD method are determined for the C(T) specimen.

During the tests beach marks and crack detection gauges are used to create a calibration curve of the DCPD method for both specimen geometries. With these calibration curves crack growth data is obtained and the fatigue crack growth rate versus stress intensity factor range data is determined. These data is fitted for each geometry with the Paris equation which gives the two Paris constants.

This thesis delivers two calibration curves for the DCPD method for two different specimen geometries of the same material. Furthermore the obtained fatigue crack growth rate versus stress intensity factor range data is given with the Paris constants for both specimen geometries where the results are analysed regarding the influence of the used specimen geometry and compared to literature.

Chapter 3

The test specimens

In this thesis the M(T) and C(T) specimen geometries recommended by ASTM [ASTM 2015] are used to investigate the geometry influence on fatigue crack growth behaviour. The dimensions for both specimen geometries according to ASTM [ASTM 2015] are shown in figure 3.1. The dimensions of the M(T) specimen which are used in the experiments are already designed. The dimensions of the C(T) specimen are designed within the scope of this thesis. To test both specimen geometries with the same testing machine a clevis as well as all necessary additional components are designed and chosen for the experiments with the C(T) specimen.

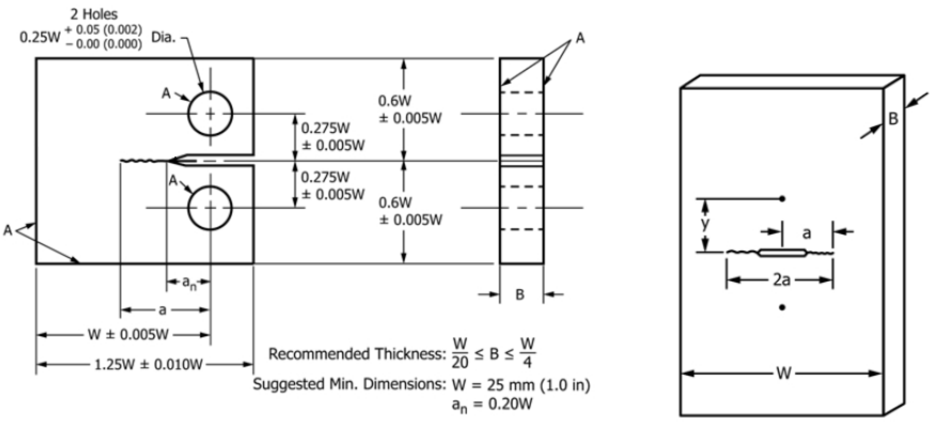

(a) Compact (tension) specimen C(T)

(b) Middle tension specimen M(T)

Figure 3.1 Geometry of M(T) and C(T) specimens given in ASTM [ASTM 2015].

The M(T) and C(T) specimens are cut out of one sandblasted and primed steel plate of the material S355 with a yield strength of $\sigma_0 = 469\,\mathrm{N/mm^2}$. The crack plane orientation of both specimens is given according to a two letter code in ASTM [ASTM 1997] for rectangular sections. The first letter gives the direction normal to the crack plane and the second letter gives the expected direction of crack propagation. In figure 3.2 the reference directions are given where L is the direction of principal deformation, T is the direction of least deformation and S is the third orthogonal direction. The M(T) and C(T) specimens used in this thesis are L - T specimens. It is important that the notch is perpendicular to the rolling direction, because microscopic structure influences the fracture toughness [Dowling 1998]. It is also recommended that the specimen is made of a material in its final condition, i.e. after heat treatment ect. [ASTM 2015].

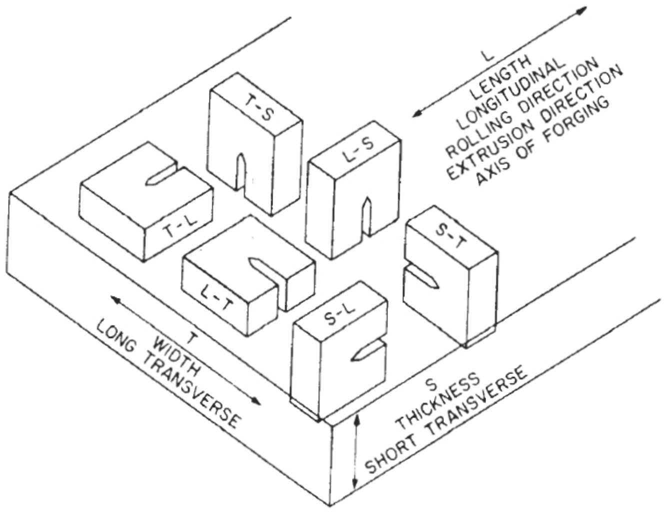

Figure 3.2 Crack plane orientation given in ASTM [ASTM 1997].

3.1 The middle tension specimen, M(T)

The middle tension specimen used in this investigation is already designed. The shape of the used notch according to ASTM [ASTM 2015] is given in figure 3.3 where a_n is the length of the notch.

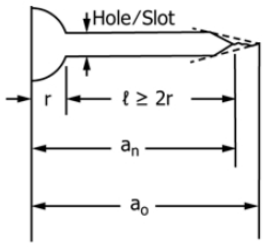

Figure 3.3 Notch of M(T) specimen given in ASTM [ASTM 2015].

The main dimensions of the M(T) specimen as well as the notch dimensions are given in table 3.1.

Table 3.1 Dimensions of used M(T) specimen and notch.

M(T) specimen	**Symbol**	**Value**	**Description**
Main dimensions	W	60.0 mm	Specimen width
	B	10.5 mm	Specimen thickness
	L	500.0 mm	Specimen length
Notch dimensions	$2a_n$	19.4 mm	Overall notch length
	r	1.0 mm	Radius of the hole
	h	1.0 mm	Notch height
	R	0.2 mm	Notch radius
	θ	30 °	Opening angle at notch tip

3.2 The compact specimen, C(T)

The dimensions of the C(T) specimen are based on ASTM [ASTM 2015]. The specimen has a width of $W = 80\,\text{mm}$, a thickness of $B = 10.5\,\text{mm}$ and the holes for the pin have a diameter of $D = 20\,\text{mm}$. According to ASTM [ASTM 2015] the notch has to be within a required envelope which is shown in figure 3.4 a). The chosen notch shape for the C(T) specimen is shown in figure 3.4 b) with a length of $a_n = 16\,\text{mm}$ and a height of $h = 16\,\text{mm}$.

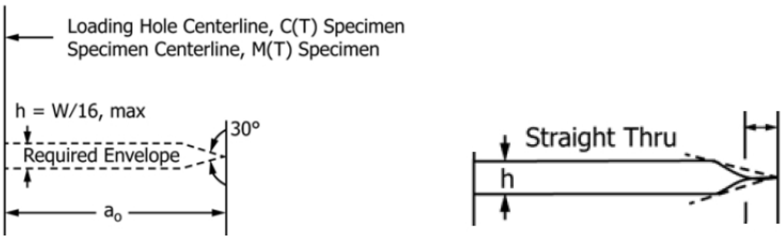

(a) Required notch envelope **(b)** Notch of C(T) specimen

Figure 3.4 Required notch envelope and used notch shape of C(T) specimen given in ASTM [ASTM 2015].

The main dimensions as well as the notch dimensions are listed in table 3.2. The designed C(T) specimen is shown in figure 3.5 which is drawn in Autodesk Inventor®. The design drawing of the C(T) specimen is shown in figure A.1 in appendix A.

Table 3.2 Dimensions of used C(T) specimen and notch.

C(T) specimen	**Symbol**	**Value**	**Description**
Main dimensions	W	80.0 mm	Specimen width
	B	10.5 mm	Specimen thickness
	D	20.0 mm	Diameter of pin hole
Notch dimensions	a_n	16.0 mm	Notch length
	h	2.0 mm	Notch height
	R	0.2 mm	Notch radius
	θ	30 °	Opening angle at notch tip

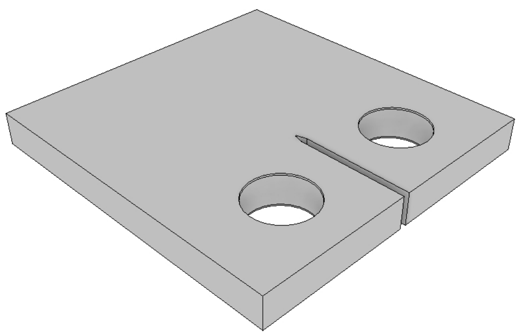

Figure 3.5 Designed C(T) specimen.

The experiments of the M(T) and C(T) specimens are performed with the same testing machine. Therefore a clevis and pin assembly has to be designed. This is done following

ASTM [ASTM 2015] where the dimensions are shown in figure 3.6. For this investigation the span of two clevises and the C(T) specimen has to be equal to the length of the M(T) specimen to be able to perform tests at low temperatures due to the dimensions of the existing cold chamber. Furthermore the clevis has to be flat on the ends to be clamped in the testing machine. The width and height of the clevis exceed the recommendations given in ASTM to be able to test thicker specimens as used in this investigation. Figure 3.7 shows the designed clevis. The design drawing of the clevis is depicted in figure A.2 in appendix A. The steel used for the clevises is 42CrMo4. For the pin a DIN EN ISO 4762 M20x90 - 12.9 screw is used which is shaped according to the design drawing in figure A.3 in appendix A.

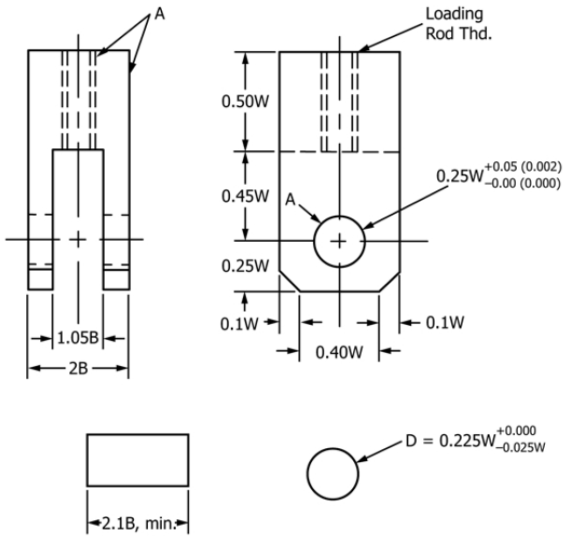

Figure 3.6 Clevis and pin assembly recommended by ASTM [ASTM 2015].

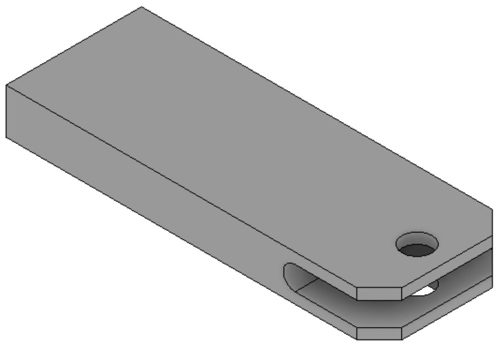

Figure 3.7 Designed clevis for the C(T) specimen.

Between the test specimen and the pin bearings are needed. The used bearings are Glycodur® PG 182015 F which are coated with Polytetrafluorethylen (PTFE). To position the bearings in the specimen holes a bolt and a die are designed, see figure 3.8. The die is used to ensure the correct vertical position of the bearings in the specimen and is made out of a leftover steel block in the laboratory. Therefore no design drawing exits. The design drawing of the bolt is shown in figure A.5 in appendix A.

Also a spacer is placed between clevis and specimen to make sure that the specimen has no direct contact with the clevis and to reduce friction. Therefore a disc made of PTFE is

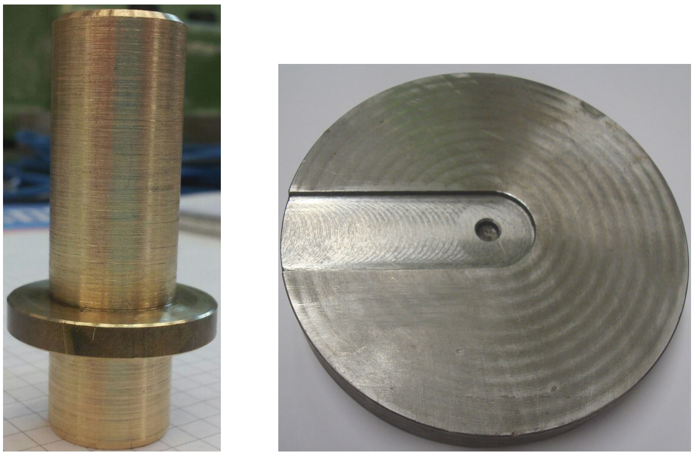

(a) Bolt (b) Die

Figure 3.8 Die and bolt for bearing positioning of the C(T) specimen.

designed where the design drawing is shown in figure A.4 in appendix A. A total of four distance discs is needed.

To fix the pin when the specimen is positioned in the clevises two R-pins 4 DIN 11024 are used.

To guarantee good reproducibility of the experimental results the position of the current input and potential measurement lead wires needed for the DCPD method, see section 2.3, are required to be at the same position for each tested specimen. These wires are attached to the specimen via threaded steel bolts with a copper coating which are already used at other experiments of the Institute. The bolts have a shaft diameter of 3 mm and a head diameter of 4 mm. To position these bolts on the specimen spot welding is used. Therefore a welding template is designed where the design drawing is shown in figure A.6 in appendix A.

To use the C(T) welding template properly a welding arrangement is designed. The C(T) specimen is fixed between two wooden plates which isolate against electricity where on top of the plates the welding template is positioned, see figure 3.9.

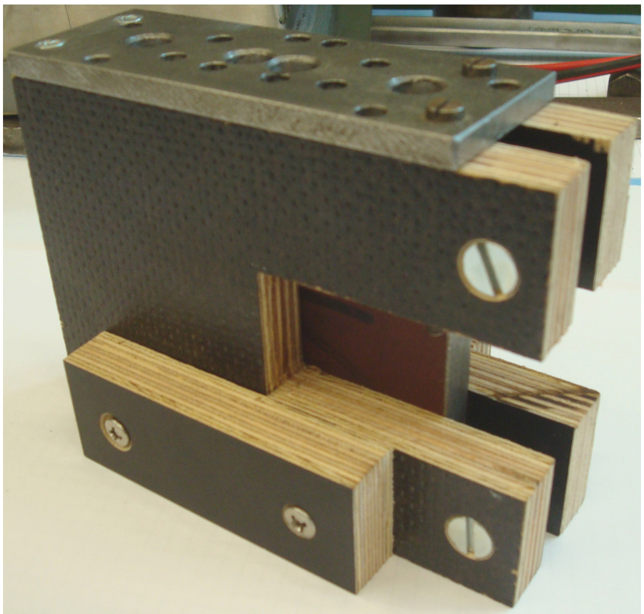

Figure 3.9 Designed welding arrangement with welding template.

Chapter 4

Experimental setup and procedures

All experiments are performed at the Institute for Ship Structural Design and Analysis at the Hamburg University of Technology. All investigations are made at room temperature.

The experimental setup consists of a resonant testing machine, a test specimen and the measuring equipment. In figure 4.1 an M(T) specimen is shown clamped in the resonant testing machine with attached potential measurement lead wires and current input wires as well as crack detection gauges. In figure 4.2 the designed C(T) specimen assembly is shown clamped in the resonant testing machine. Here, too, the electrical setup is connected.

In the following sections the equipment used for the experiments and the test procedure as well as the procedure to determine the crack lengths are explained.

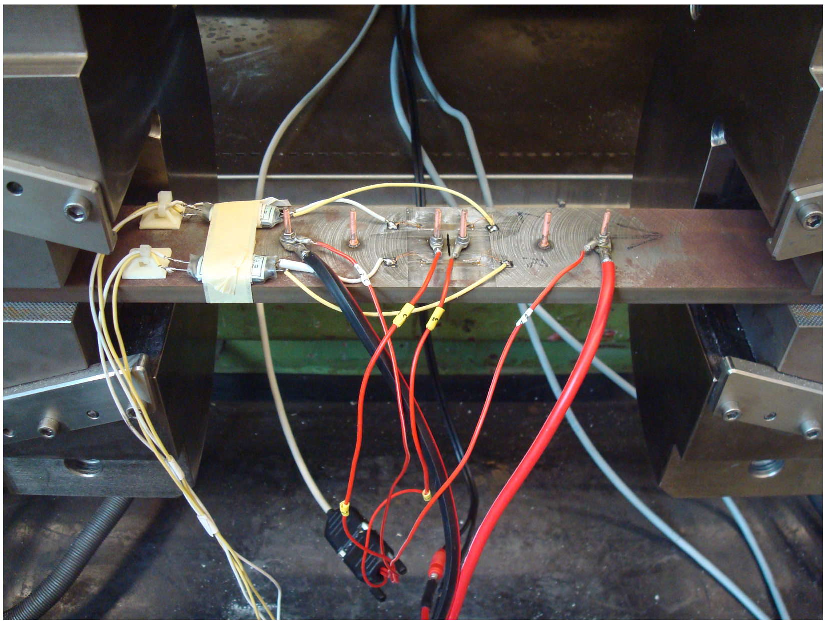

Figure 4.1 M(T) specimen clamped in the resonant testing machine with attached potential measurement lead wires, current input wires and crack detection gauges.

4.1 Used equipment

The used equipment consists of a resonant testing machine, a power source, a voltmeter, crack detection gauges, components for isolation as well as potential measurement lead wires and current input wires.

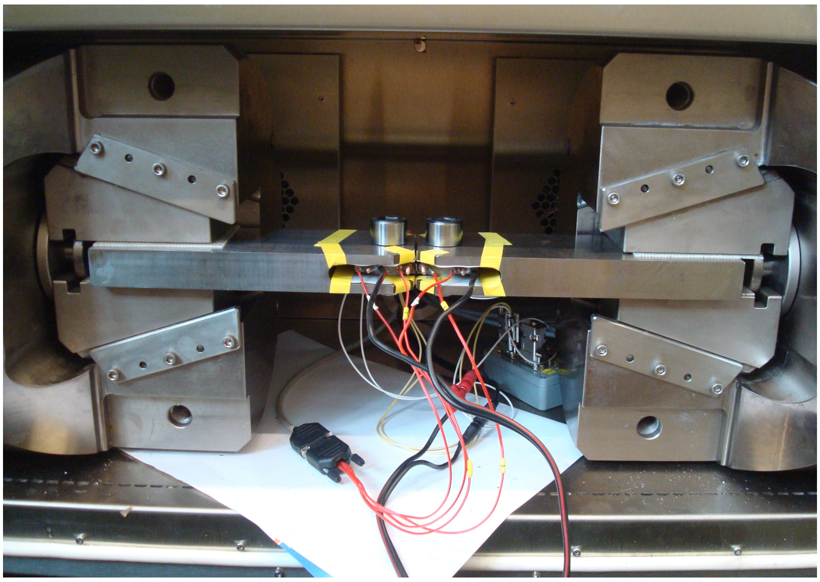

Figure 4.2 C(T) specimen clamped in the resonant testing machine with attached potential measurement lead wires and current input wires.

4.1.1 Resonant testing machine

The required load for the fatigue crack growth testing is applied by a resonant testing machine where the specimen is positioned between two hydraulic clamps. For the load application a constant static force is created and a dynamic alternating force is superimposed on the static force via a spring to create the maximum and minimum load. Thus the load pattern is sinusoidal and therefore a dynamic and static force has to be entered into the control system of the testing machine. The machine is able to switch automatically between different predefined load patterns. This is used for the implementation of two different load ratios per experiment for the creation of beach marks. Before the specimen is torn apart completely the testing machine has to stop automatically. Therefore it is equipped with safety devices.

The frequency varies in a range between 26 Hz and 33 Hz depending on the used specimen geometry.

4.1.2 Power source

The power source is a DIGISTANT® Type 6422/20 which is made by *burster präzisionsmesstechnik*. It can provide a maximum current of 20 A.

4.1.3 Voltmeter

The used voltmeter is an AUTOLOG 3000 from *Peekel Instruments* and it measures with 1000 Hz. Several variables are measured by the voltmeter and recorded by a personal computer. Recording all variables at 1000 Hz would lead to a too large amount of values. Therefore virtual channels are created to process the measured variables directly by averaging over a predefined amount of time. The created virtual channels differ from the initial configuration of the DCPD method and the main configuration which are listed in table 4.1.

Table 4.1 Virtual channels for the initial and main configuration of the DCPD method.

Initial configuration	Main configuration
Time	Time
Laboratory temperature	Laboratory temperature
Specimen temperature	Specimen temperature
Maximum applied load	Maximum applied load
Minimum applied load	Minimum applied load
Voltage 1 Voltage 2	Voltage drop
Burden voltage	Reference voltage
Number of cycles	Number of cycles
Crack detection gauge 1	Crack detection gauge 1
Crack detection gauge 2	Crack detection gauge 2

4.1.4 Crack detection gauges

The used crack detection gauges (CDG) are FAC-5 made by Tokyo Sokki Kenkyujo Co., Ltd.. These gauges measure the length of a crack due to the disconnection of the grid during crack growth in a metal specimen. The grid is aligned in an 0.1 mm interval, the total number of grids is 46 and the measuring range is 4.5 mm with an electrical resistance of 1 Ω. In figure 4.3 a schematic picture of the used crack detection gauge is shown.

The crack detection gauge is glued with a special adhesive, also made by Tokyo Sokki Kenkyujo Co., Ltd., onto the top side of the test specimen in front of the notch and perpendicular to the crack propagation direction. Figure 4.4 shows a glued crack detection gauge on a test specimen. It is important that there is no contact between the strands of the crack gauge and the surface of the specimen. That is the reason why the strands are bend in the way they are in figure 4.4.

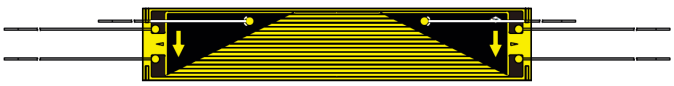

Figure 4.3 Schematic picture of crack detection gauge FAC-5 by Tokyo Sokki Kenkyujo Co., Ltd..

4.1.5 Isolation of the test frame

It is very important to isolate the test frame electrically from the test specimen to obtain correct voltage drop readings. Circuit boars made of epoxy resin are used for isolation which are positioned between the clamps of the resonant testing machine and the specimens faces or, in case of the C(T) specimen, the faces of the clevises. The use of circuit boards is cost-effective and they are easy to cut to the needed dimensions. Figure 4.5 shows the used circuit boards.

Furthermore the clevises are covered on the inside with a Teflon foil to isolate them against contact with the soldering points and the wiring of the CDG. For the same reason the surface of the C(T) specimen is locally covered in tape. On the M(T) specimen no such isolation is necessary.

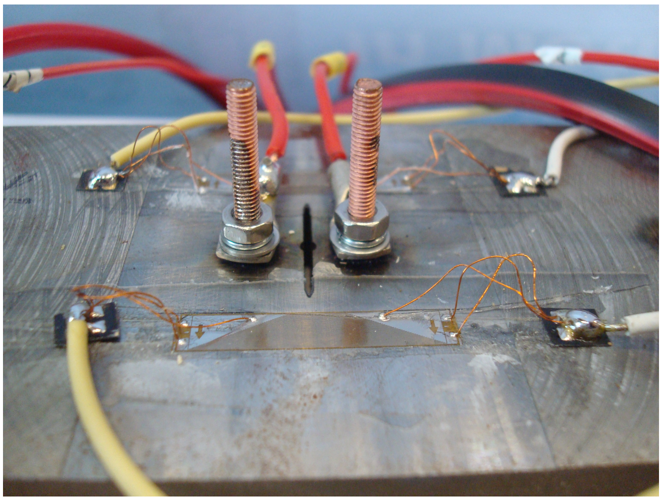

Figure 4.4 Crack detection gauge FAC-5 glued to a test specimen.

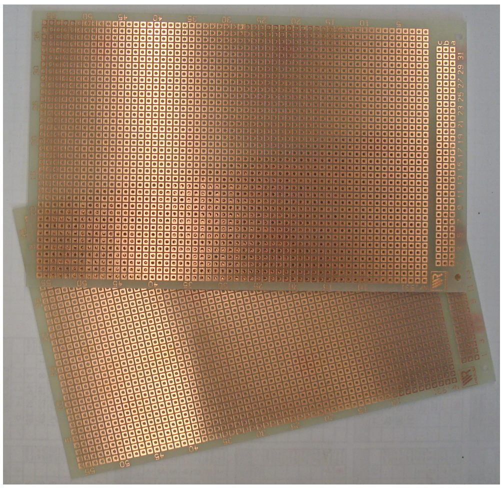

Figure 4.5 Used circuit boards for isolation.

4.1.6 Current input and potential measurement lead wires

According to ASTM [ASTM 2015] the voltage measurement lead wires should be as fine as possible to locate them precisely on the test specimen. Thin wires are also recommended to minimize the stress during the fatigue test, so that they are not getting loose. The wires should be as short as possible and rigid to reduce stray voltages.

The current input wires should be of greater diameter to provide the required current. All wires are made of copper and have an insulating layer.

4.2 Test procedure for fatigue crack growth testing

The preparation of the test specimens at the beginning of every experiment differs between the M(T) and C(T) specimens. For both specimens four steel bolts are spot welded onto the test specimens with the aid of welding templates and crack detection gauges if needed are glued onto the test specimens. After the glue is dry the wires of the crack detection gauges are soldered onto the specimen and connected with a resistance to amplify the measurements. For the M(T) specimen all additionally required wires are then attached to the steel bolts with cable lugs and fixed with ring washers and nuts.

For the C(T) specimen the bearings have to be positioned in the specimen holes with the aid of the designed bolt and die before the wires can be attached to the steel bolts. Then the spacers are placed on each face of the specimen and all pieces are placed in the clevises and fixed with the pins. Afterwards the pins are fixed with R-pins.

After preparing the specimens the current input wires are connected with the power source and the potential measurement lead wires as well as the wires for the crack detection gauge measurements are connected with the voltmeter which is connected to a personal computer. Then the M(T) specimen or the C(T) specimen assembly is positioned between the clamps of the resonant testing machine. The isolation is attached as explained in section 4.1.5.

Afterwards the personal computer, the voltmeter and the power source are switched on and the correct working of every contact and every virtual channel is ensured. After a stabilization period of the system the two clamps of the resonant testing machine are closed. During clamping it is important that the load force of the testing machine is set to zero.

The next step is to account for the thermoelectric effect. Therefore the power source is turned off, the current direction is switched and afterwards the power source is turned on again. When enough data is obtained the procedure is reversed. After accounting for the thermocouple effect the static and dynamic force of the load ratios as well as the number of cycles are entered into the control program of the resonant testing machine. Now the experiment is started. When the static and the dynamic loads of each load ratio are reached safety devices have to be adjusted.

4.3 Determination of crack length

The crack size used to create the calibration curve is obtained in two different ways. One way is the determination with the aid of beach marks, the other way is the determination with crack detection gauges. These methods are explained hereafter.

Determining the crack length with beach marks the crack lengths are calculated in accordance with ASTM [ASTM 1997] where the crack length is measured at three positions on each beach mark due to the curved shape of the crack and then the average of these points is taken. One position b) is at the center of the crack front, the two other positions a) and c) are midway between the center of the crack front and either end of the crack front on the surface. In figure 4.6 the three used points for the crack front correction are sketched for one beach mark. For the M(T) specimens this has to be done for both sides of the notch to obtain the overall crack lengths.

The crack lengths are obtained with the aid of a measuring tool within the program AutoCAD applied to a photograph of the fracture surface. Due to the manual determination of the positions a), b) and c) as well as the reference point variations of the crack lengths are inevitable. Also the reproduction of said dimensions is limited.

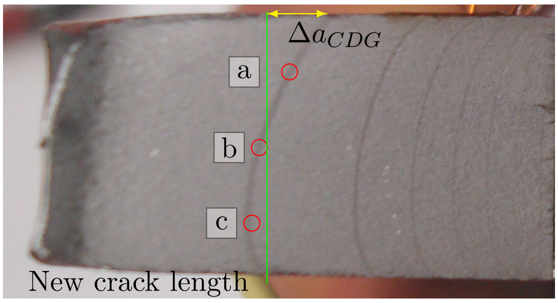

Figure 4.6 Beach marks of specimen $VJ1$ to demonstrate the crack front correction. The yellow line indicates the difference between the crack position at the surface and the calculated crack length Δa_{CDG} to correct the position of the crack detection gauge strands. The red circles indicate the used positions and the green line indicates the averaged crack length according to ASTM [ASTM 1997].

The other way to determine the crack lengths is by using the crack detection gauges. Here the positions of the strands of the crack detection gauges are known, see section 4.1.4, as well as the positions where the crack detection gauges are glued onto the specimen surface.

It is important to take the shape of the crack front into account. Due to the position of the crack detection gauge on the specimen's surface the strands are disconnected later because the crack grows slower at the surfaces. With the aid of the beach marks the difference between the corrected beach marks in accordance with ASTM [ASTM 1997] and the position of the strands at the surface Δa_{CDG} can be calculated and this difference is added to the strands position of the crack detection gauge, see figure 4.6. For making this correction beach marks in the same range as the crack detection gauges are used and the calculated differences are averaged. For M(T) specimens this has to be done for each side of the notch and then averaged again between these two sides.

Chapter 5

Preliminary tests

This chapter deals with the preparation, execution and analysis of preliminary tests. The purpose of these experiments is the testing of the equipment and to implement and optimize the direct current potential drop method in fatigue crack growth testing of M(T) and C(T) specimens. Challenges in this implementation are faced before first results are obtained and discussed.

Prior to the experiments the load limits of the M(T) and C(T) specimens are determined. To fulfill the requirement that LEFM is valid according to ASTM [ASTM 2015] the maximum applied load for the M(T) specimen P_{max} is determined as

$$(W - 2a) \geq 1.25 \frac{P_{max}}{B\sigma_0}. \tag{5.1}$$

Rearranging equation (5.1) and inserting the values from table 3.1 a maximum force of $P_{max} = 154.96\,\mathrm{kN}$ is determined.

The maximum applied load for the C(T) specimen is determined with the following equation given in ASTM [ASTM 2015]

$$(W - a) \geq \frac{4}{\pi} \left(\frac{K_{max}}{\sigma_0} \right)^2. \tag{5.2}$$

Knowing K_{max} the maximum applied load can be calculated with rearranging the equation of the stress intensity factor, see section 2.1.3,

$$P_{max} = \frac{K_{max} B \sqrt{W}}{F_P}. \tag{5.3}$$

The C(T) specimen should not be loaded with more than $73\,\mathrm{kN}$. The values of the maximum applied loads are calculated with a yield strength of $\sigma_0 = 469\,{}^{N}\!/\mathrm{mm}^2$.

The minimum load for both specimens is limited by the accuracy of the resonant testing machine. To ensure that under no circumstances a compressive load is applied to the specimens a nonzero mean stress loading case, see section 2.2.2, with only positive values is applied.

5.1 Testing of the equipment and setting of the DCPD initial configuration

The preparation of the test specimens and the test procedure is performed as explained in section 4.2. In total nine M(T) specimens and one C(T) specimen are used for first preliminary tests where no crack detection gauges are used.

During the first preliminary tests parts of the electrical system are renewed, the current intensity is reduced from 20 A to 16 A to spare the measuring equipment, and the location of the current input for the M(T) specimen is changed to receive better potential drop readings.

Preliminary tests of M(T) and C(T) specimens are made at room temperature. On each specimen two voltage measurements are taken, Voltage 1 and Voltage 2, that correspond to the virtual channels listed in section 4.1.3. Voltage 1 is taken between points 1 and 2 and Voltage 2 is taken between points 1 and 3, see figure 5.1. The voltage drop across the crack is then calculated by subtracting the individual values of the two virtual channels divided by the burden voltage of the power source. The latter is to compensate for variations in the output of the power source.

The distance between the current input position and the middle of the notch is initially set to $y_I = 45\,\mathrm{mm}$. It is found that a distance of $y_I = 75\,\mathrm{mm}$ gives better results of the potential drop readings. In figure 5.1 the adapted positions are indicated. The welding template for the M(T) specimen is adjusted to the adapted positions.

The distance between one potential measurement lead wire location and the middle of the notch is chosen to be $y_U = 6\,\mathrm{mm}$ which was already used in several previous investigations and is kept during the preliminary tests. In figure 5.1 the potential measurement lead wire locations as well as the current input locations on an M(T) specimen are shown schematically. The thin red wires are the potential measurement lead wires and the thicker black and red wires are the current input wires. The spare steel bolts are left from the former current input position.

The current input locations as well as the potential measurement lead wires for the C(T) specimen are chosen regarding the findings of Aronson [Aronson and Ritchie 1979] and Ritchie [Ritchie et al. 1971], see section 2.3.3. All wire locations are placed at the front surface of the specimen, see figure 5.2. Thus for the used specimen the distance between the current input position and the middle of the notch is $y_I = 36\,\mathrm{mm}$ and between the potential measurement lead wire location and the middle of the notch is $y_U = 6\,\mathrm{mm}$. In figure 5.2 all wire input locations for the C(T) specimen are shown schematically. The thin red wires are the potential measurement lead wires and the thick red and black wires are the current input wires.

In the following these setups, depicted in figures 5.1 and 5.2 for the M(T) and C(T) specimens, respectively, are referred to as DCPD initial configuration.

5.2 Implementation of the DCPD method: initial configuration

In total six M(T) specimens and two C(T) specimens are tested with the initial configuration of the DCPD method. All relevant specimen data such as loading condition, name, main dimensions etc. are listed in table B.1 and table B.4 in appendices B.1 and B.2 for the M(T) and C(T) specimen, respectively.

A set of M(T) and a set of C(T) specimens are cut out of one steel plate which are referred to as *VJ* and *VH*, respectively. In addition there are M(T) specimens tested from another steel plate of the same material which are referred to as *JS*.

The experiments are performed at room temperature and start with tests of M(T) specimens followed by C(T) specimens. All used specimens are tested with constant amplitude loading at a nonzero mean stress, see section 2.2.2. The used M(T) specimens are tested at the two load ratios $R = 0.1$ and $R = 0.5$ and all C(T) specimens at the load ratios $R = 0.2$ and $R = 0.4$ where the second load ratio of each specimen is used to create beach marks, see section 2.3.2.

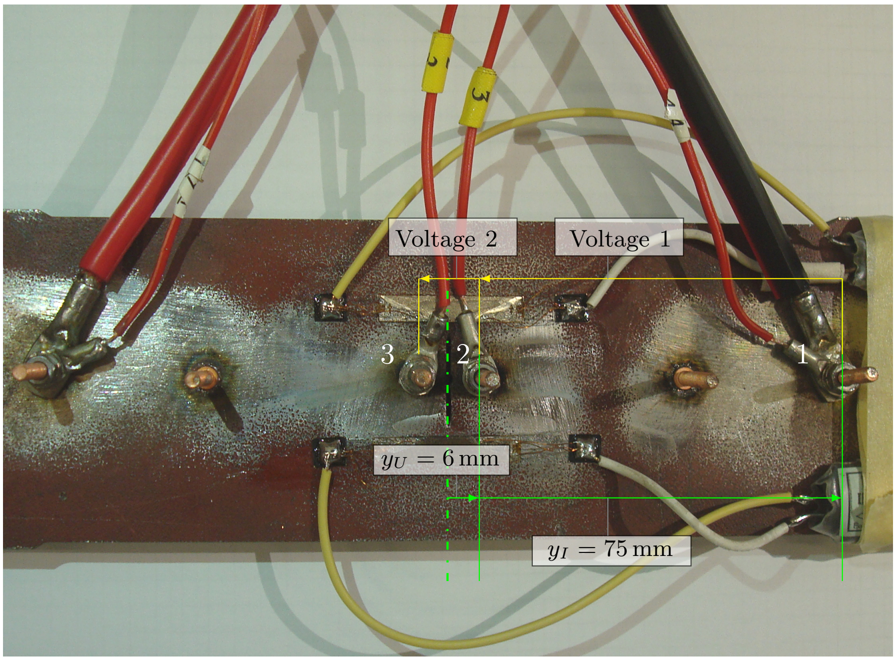

Figure 5.1 Wire locations of the M(T) specimen using the DCPD initial configuration. Thin red wires are potential measurement lead wires and thicker black and red wires are current input wires. Voltage 1 is measured between point 1 and 2, Voltage 2 is measured between point 1 and 3.

The higher first load ratio for the C(T) specimens (compared to the M(T) specimens) is chosen to ensure that the resonant testing machine is working correctly because of difficulties with generating very low loads.

If crack detection gauges are used they have to be glued at a position where a sufficient precrack exists, thus the notch has no influence on the fatigue crack growth and the crack tip is sharp. According to ASTM [ASTM 2015] the minimum required fatigue precrack length $a_0 - a_n$ is $0.1B, h$ or 1 mm whichever is greater and precrack and notch should lie within the required envelope shown in figure 3.4 a). In Walters [Walters and Voormeeren 2013] it is found for linear elastic conditions that precracks larger than $0.5h$ cause less than 1 % error of the stress intensity factor. In this study it is also found that if the enclosing angle of the required envelope is smaller than 42 ° an error of less than 1 % occurs. Hence, a precrack length of 0.5 mm and 2 mm is sufficient for the M(T) and C(T) specimen, respectively, and an opening angle at the notch tip of $\theta = 30\,°$ for both specimen geometries. Therefore if crack gauges are used for the M(T) or C(T) specimen they are positioned 2 mm in front of the specimen notch.

5.2.1 M(T) specimen

All M(T) specimens are loaded with a maximum load of $P_{max} = 50\,\text{kN}$ which lead to a minimum load of $P_{min} = 5\,\text{kN}$ for $R = 0.1$ and $P_{min} = 25\,\text{kN}$ for $R = 0.5$.

The first M(T) specimen $JS17$ is equipped with two crack detection gauges and the load ratios are applied for 75000 and 15000 cycles where the latter corresponds to the load ratio $R = 0.5$. The measurements are averaged and stored every 20 seconds which is changed for all following specimens to 2 seconds because the data of the crack detection gauges is averaged within a too long period which results in impractical data. Also the potential drop readings

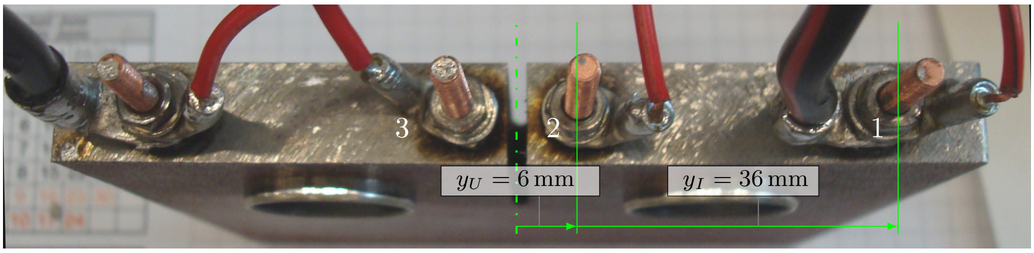

Figure 5.2 Wire locations of the C(T) specimen using the DCPD initial configuration. Thin red wires are potential measurement lead wires and thicker black and red wires are current input wires. Voltage 1 is measured between point 1 and 2, Voltage 2 is measured between point 1 and 3.

are not correct. Thus no data of specimen $JS17$ is used for further analysis.

For specimen $VJ4$ no crack detection gauges are used. To reduce environmental influences a cold chamber, which is already positioned around the resonant testing machine for planned fatigue tests at low temperatures, is put around the specimen. The temperature inside the chamber is set to a constant temperature of 23 °C. In figure 5.3 the applied maximum and minimum loads of specimen $VJ4$ are shown where the inhomogeneities at the maximum and minimum load is due to measuring errors of the system. The minimum load switches in accordance with the predefined load ratios. At the switching point to the second load ratio the dynamic force of the resonant testing machine is decreasing quickly and then increasing again which can be seen at the blue vertical lines of the maximum load. In total seven beach marks are created on the fracture surface which are depicted in figure 5.4.

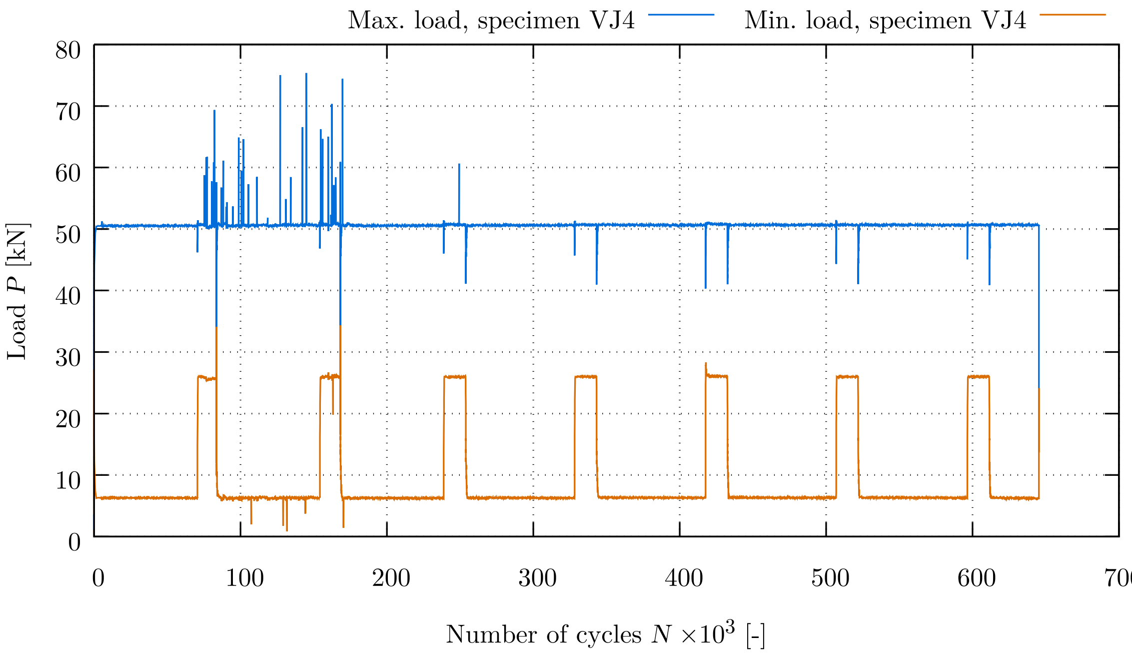

Figure 5.3 Applied load, specimen $VJ4$.

The voltage drop, calculated as explained in section 5, of specimen $VJ4$ is depicted in

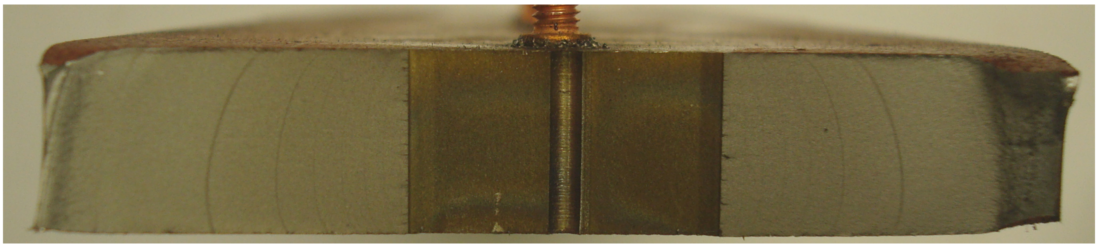

Figure 5.4 Beach marks of specimen $VJ4$. The light bands correlate with the load ratio $R = 0.1$, the dark bands correlate with the load ratio $R = 0.5$.

figure 5.5 with unit mV. The global trend is an increasing voltage drop with an increasing number of cycles which is as expected because the crack length increases with an increasing number of cycles, thus the electrical resistance raises, see section 2.3. With the present electrical equipment the noise of the potential measurement was already reduced within the preliminary tests as much as possible.

During this test the temperature inside the chamber increases by about 1.8 °C which has an negligible effect on the voltage drop.

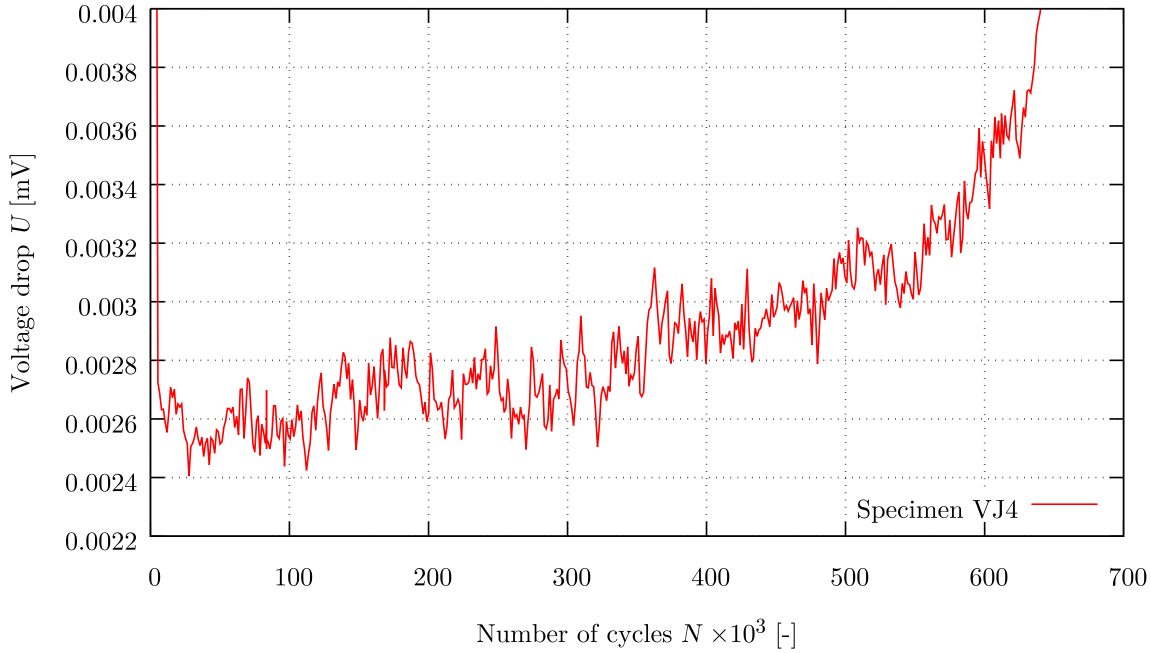

Figure 5.5 Voltage drop, specimen $VJ4$.

For specimen $VJ1$ the number of cycles of the load ratio $R = 0.5$ is increased to 20000 in order to obtain thicker beach marks. Here the cold chamber is also put around the specimen but without heating it because no temperature influence was recognised at the measurements of the previous specimen.

This specimen is equipped with two crack detection gauges for which better results are obtained compared to specimen $JS17$, see figure 5.6. These measurements have a stepped shape because at each disconnected strand the strain increases immediately.

The applied load is shown in figure B.2 a) in appendix B.1 and it can be seen that se-

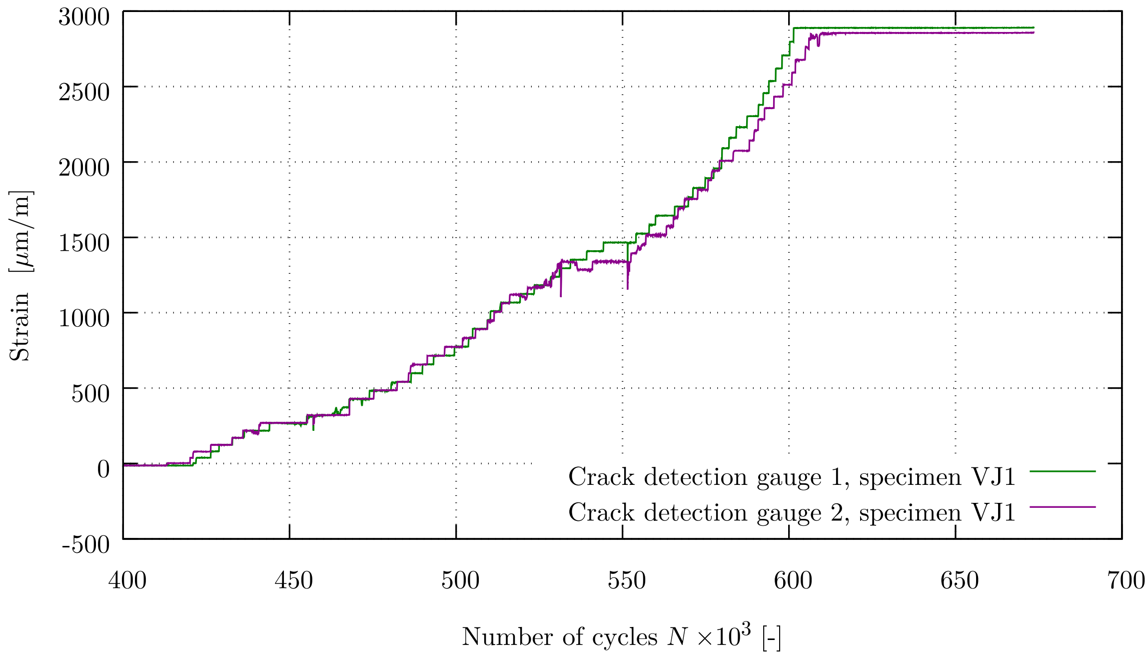

Figure 5.6 Crack detection gauges, specimen $VJ1$.

ven beach marks are created. The voltage drop is shown in figure B.2 b) and globally increases.

Specimen $JS21$ lasts much longer than the other M(T) specimen and 18 beach marks are created. The reason for this is potentially the different steel plate. For the test with this specimen the cold chamber is not closed because of a damaged door but this circumstance shows no effect on the obtained results. Nevertheless the results of specimen $JS21$ are not used for further analysis because it cracked asymmetrically, see figure 5.7.

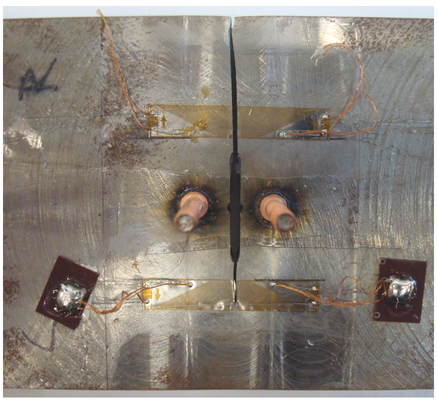

Figure 5.7 Asymmetrically cracked specimen $JS21$.

5.2.2 C(T) specimen

The C(T) specimen $VH1$ is tested with a maximum load of $P_{max} = 16\,\text{kN}$ and the second specimen $VH2$ with a maximum load of $P_{max} = 12\,\text{kN}$ which leads to a minimum load of

$P_{min} = 3.2\,\mathrm{kN}$ and $P_{min} = 6.4\,\mathrm{kN}$ for the first and second load ratio, respectively, for specimen $VH1$ and $P_{min} = 2.4\,\mathrm{kN}$ and $P_{min} = 4.8\,\mathrm{kN}$ for specimen $VH4$.

For specimen $VH1$ the load ratios are applied for 40000 and 10000 cycles, respectively, for specimen $VH2$ the second load ratio is extended to 15000 cycles to obtain thicker beach marks. In figure B.5 a) the applied load for specimen $VH1$ is shown where five beach marks are created. For specimen $VH2$ the applied load is shown in figure B.6 a) and in total nine beach marks are created. Difficulties of the resonant testing machine of applying the correct loads are identified for both tested specimens. Specimen $VH2$ is also equipped with one crack detection gauge whose readings are shown in figure B.6 c).

5.2.3 Results of DCPD initial configuration

For creating a calibration curve of the DCPD method with the obtained experimental data to relate the voltage drop to the crack length, see section 2.3.2, beach marks and crack detection gauges are used. The calibration curve is established for the M(T) specimens with specimens $VJ1$ and $VJ4$ and for the C(T) specimens with specimens $VH1$ and $VH2$.

The initial voltage drop U_0 for the M(T) specimen calibration curve is taken at the position of the first crack detection gauge strand. The initial voltage drop value as well as every other voltage drop value has to be corrected for the thermoelectric effect which is done by switching the current direction before the experiment starts. The value of the voltage drop with the switched $U_{switched}$ and unswitched U_{normal} current direction are subtracted and divided by 2 which leads to the voltage drop of the thermoelectric effect U_{diff}

$$U_{diff} = \frac{1}{2}(U_{normal} - U_{switched}). \tag{5.4}$$

For the calibration curve the voltage drop of the thermoelectric effect U_{diff} is taken as the average value of all used test specimen with the same geometrical shape.

The informations regarding the calibration curve are equally weighted for each specimen. If more than one dataset is obtained for a specimen these sets are equal, too. Thus the data of for instance $VH2$, equally generated with beach marks and crack detection gauges, is considered equal to the data of specimen $VH1$, generated with beach marks only. To ensure a sharp crack that is not influenced by the notch data below a specimen specific threshold value of the cycle number is discarded. The data then is fitted with a linear function that represents the calibration curve. The determination of the crack lengths used for the calibration curve is explained in the following section.

In figure 5.8 and figure 5.9 the calibration curve for the M(T) specimens $VJ1$ and $VJ4$ and for the C(T) specimens $VH1$ and $VH2$ are shown, respectively. The gray points indicate the area below the threshold that is not used to create the calibration curve.

Further analysis of the obtained data using the calibration curves have shown that the DCPD method is not accurate enough in this configuration because negative fatigue crack growth rates are obtained which is due to scatter in the voltage drop readings. Therefore a new configuration of the DCPD method is tested which is introduced in the next chapter.

5.3 Testing a new arrangement

Since the results of the initial configuration of the DCPD method are unsatisfying a new arrangement of the voltage drop measurement is tested with specimen $VJ2$ to measure the

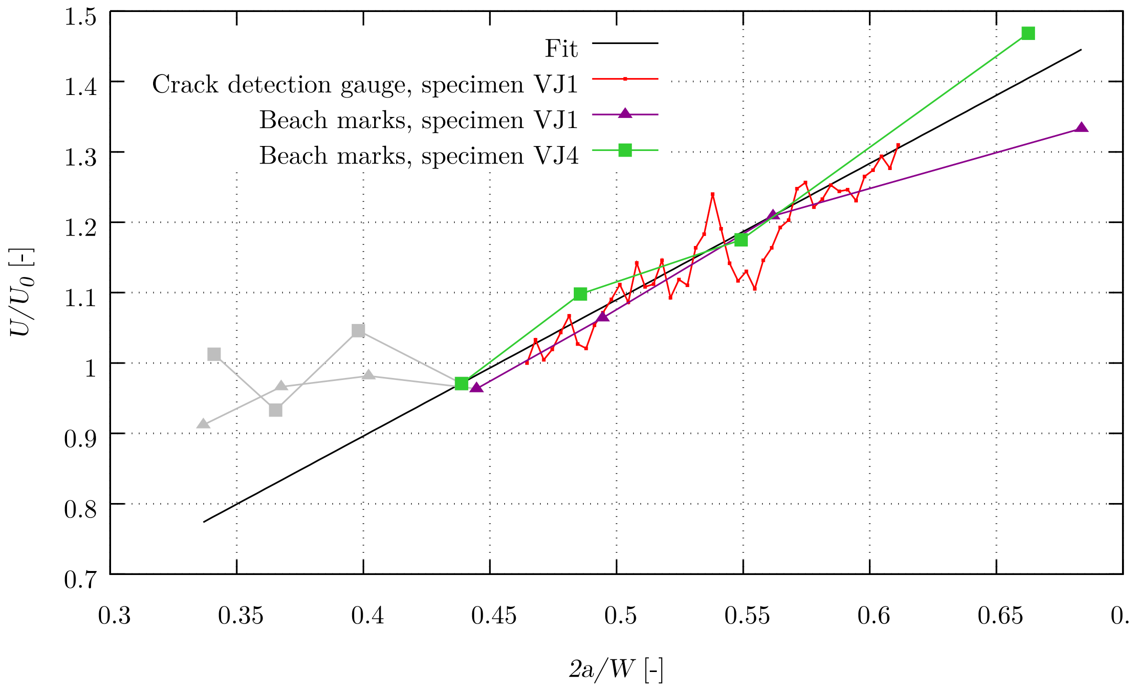

Figure 5.8 Calibration curve (Fit) for M(T) specimens obtained from beach marks and crack detection gauges from specimen $VJ1$ and $VJ4$.

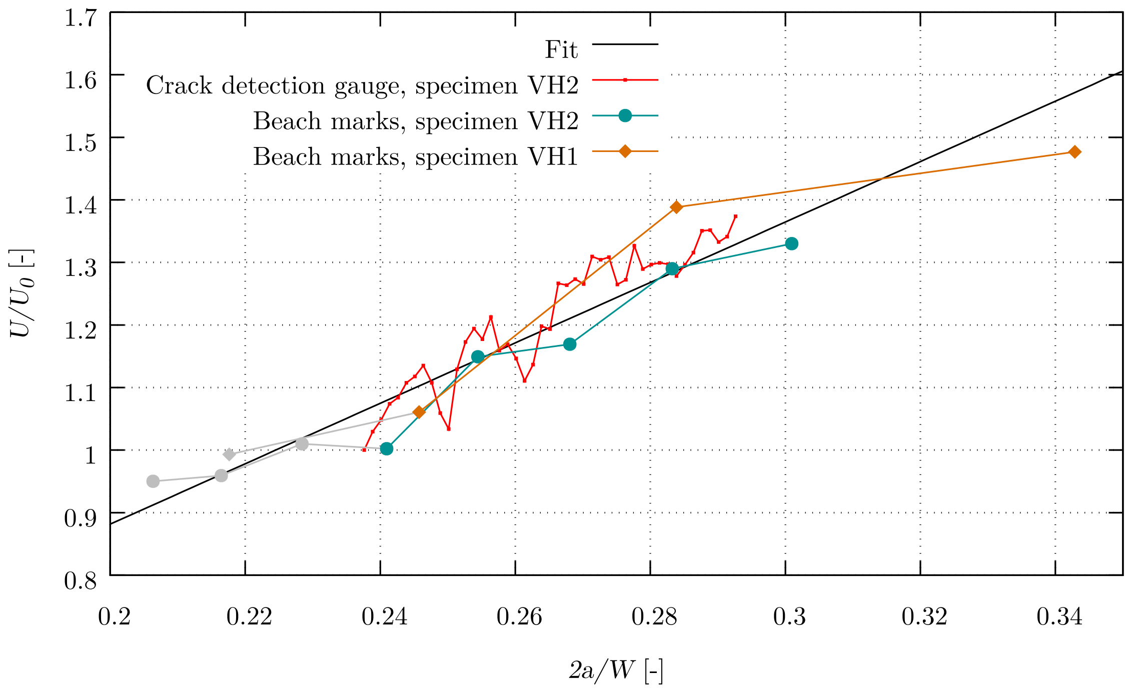

Figure 5.9 Calibration curve (Fit) for C(T) specimens obtained from beach marks and crack detection gauges from specimen $VH1$ and $VH2$.

reference voltage directly on the specimen. Therefore the current input positions are changed. Specimen $VJ2$ is equipped with a temperature sensor which is attached to the specimen surface, thus a specimen heating can be recorded directly and it can be checked if a specimen heating influences the obtained results.

Due to wrong clamping the specimen cracked asymmetrically and no data of this specimen is used for further analysis. However, this new arrangement presented some advantages over the initial configuration which leads to the development of the DCPD main configuration that is explained in the following chapter.

Chapter 6

Implementation and results of the DCPD method: main configuration

After obtaining no acceptable results with the initial configuration of the DCPD method the voltage drop across the crack is now measured directly and a different arrangement of the potential measurement positions is implemented using a new power source. This new arrangement is referred to as DCPD main configuration. In figure 6.1 this configuration is shown for the M(T) specimen where one additional position for measuring a reference voltage is created at 45 mm from the centreline of the notch. The used positions for the voltage drop measurement as well as the reference voltage are indicated. For the C(T) specimen the main configuration is depicted in figure 6.2.

One M(T) specimen, $VJ3$, and one C(T) specimen, $VH4$, are tested with the DCPD main configuration. All relevant specimen data is listed in table B.1 and table B.4 in appendices B.1 and B.2 for the M(T) and C(T) specimens, respectively.

The DCPD main configuration results in better voltage drop readings compared to the initial configuration. In figure 6.3 the voltage drop measurements for the M(T) specimen are shown where the voltage drop increases with an increasing number of cycles, as expected, and the noise is strongly decreased. Also the voltage drop increases for the M(T) specimen from the first to the last registered beach mark by about 100 % whereas for the initial configuration the increase is approximately 50 %. For the C(T) specimen the voltage drop is depicted in figure B.7 b) in appendix B.2 where the voltage drop increases from first to the last registered beach mark by about 50 % whereas the voltage drop for the C(T) specimens tested with the initial configuration of the DCPD method increases by approximately 20 % to 50 %.

The M(T) specimen is tested at the two load ratios $R = 0.1$ and $R = 0.5$ and the C(T) specimen at the load ratios $R = 0.1$ and $R = 0.4$. The applied number of cycles for the M(T) specimen is 75000 cycles for the first and 20000 cycles for the second load ratio. For the C(T) specimen 40000 and 17000 cycles are applied. The first load ratio of the C(T) specimen is realised after adjustments on the resonant testing machine. The load fluctuations are reduced to an acceptable range. The M(T) and C(T) specimens are loaded with a maximum load of $P_{max} = 45\,\mathrm{kN}$ and $P_{max} = 11\,\mathrm{kN}$, respectively. The minimum loads for the two load ratios applied to the M(T) specimen are $P_{min} = 4.5\,\mathrm{kN}$ and $P_{min} = 22.5\,\mathrm{kN}$ and for the C(T) specimen $P_{min} = 1.1\,\mathrm{kN}$ and $P_{min} = 4.4\,\mathrm{kN}$.

In appendix B.1 figure B.3 a) and in appendix B.2 figure B.7 a) the applied loads of specimen $VJ3$ and specimen $VH4$ are depicted, respectively. Ten beach marks for the M(T) specimen and 19 beach marks for the C(T) specimen are created which are shown in figure B.8. Specimen $VH4$ is additionally equipped with a crack detection gauge which is glued

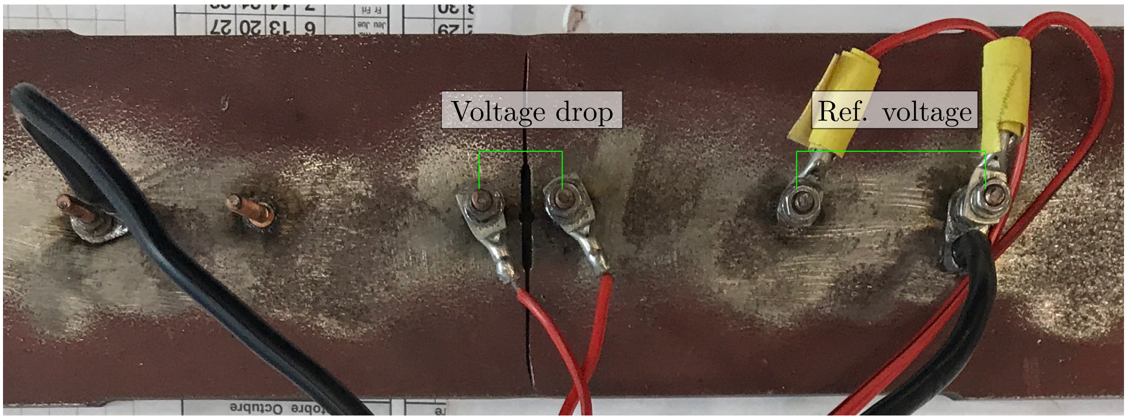

Figure 6.1 DCPD main configuration, M(T) specimen *VJ*3.

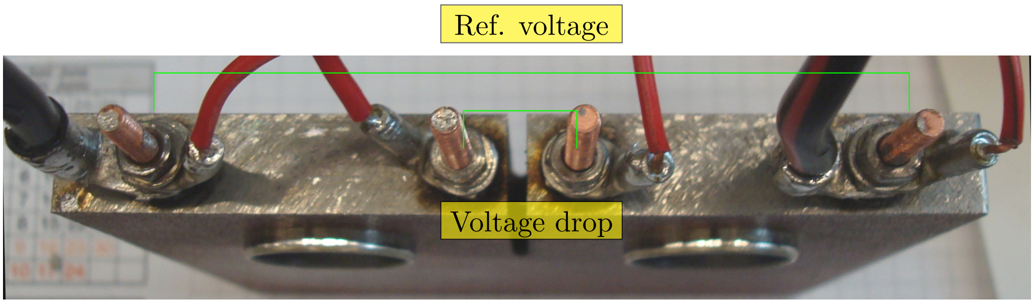

Figure 6.2 DCPD main configuration, C(T) specimen *VH*4.

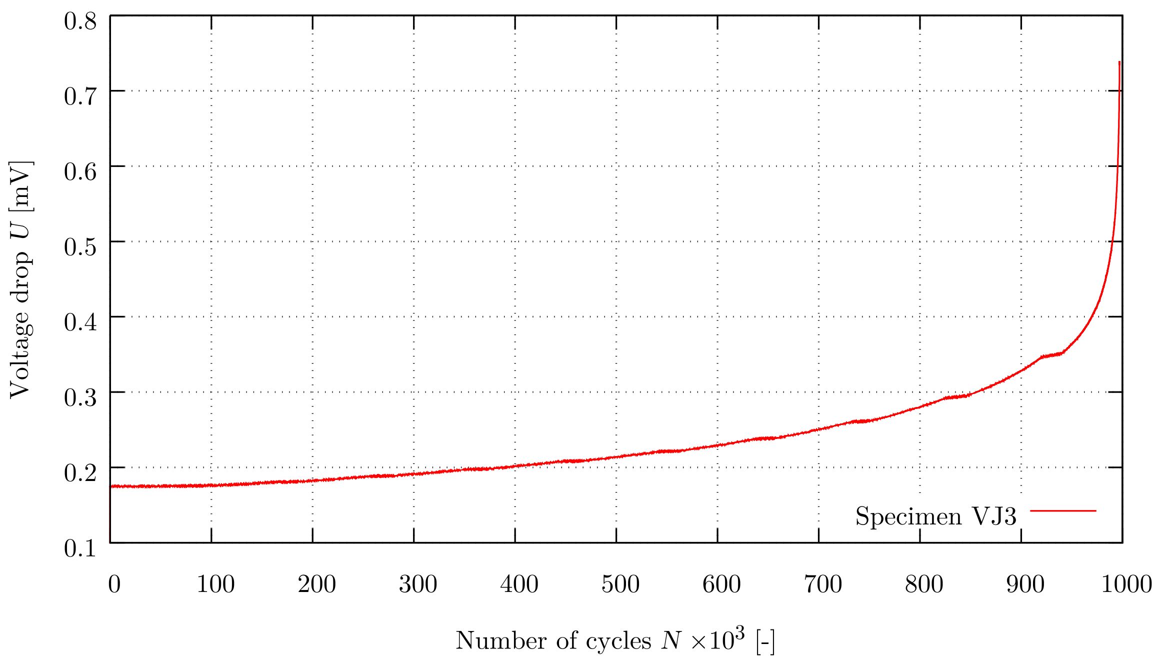

Figure 6.3 Voltage drop, specimen *VJ*3.

2 mm in front of the specimen notch. In figure B.7 c) in appendix B.2 the crack detection gauge readings are shown.

6.1 Results of DCPD main configuration

To create calibration curves of the DCPD main configuration for the M(T) and C(T) specimens beach marks and crack detection gauges are used. The initial voltage drop U_0 is taken at the position of the first crack detection gauge strand for the C(T) specimen and for the M(T) specimen the initial voltage drop is taken at a crack position where no influence of the notch is expected. The voltage drop has to be corrected for the thermoelectric effect as explained in section 5.2.3. The information regarding the calibration curve is equally weighted for each specimen as already explained in section 5.2.3. Data were an influence of the notch is expected is omitted. The data then is fitted with a linear function. The determination of the crack lengths via beach marks and crack detection gauge for the calibration curves is already explained in section 4.3.

In figure 6.4 and figure 6.5 the calibration curves of the M(T) and CT(T) specimens are shown, respectively, which are created for the M(T) specimen with beach marks and for the C(T) specimen with beach marks as well as with a crack detection gauge. As mentioned in section 5.2.3 the gray points indicate omitted data that is not used to create the calibration curve.

With these obtained calibration curves a relation between voltage drop and crack length is given for a particular specimen geometry. Thus the crack-length-to-width ratio $^{2a}/_{W}$ or $^{a}/_{W}$ can be determined through the use of the calibration curve with the voltage drop readings.

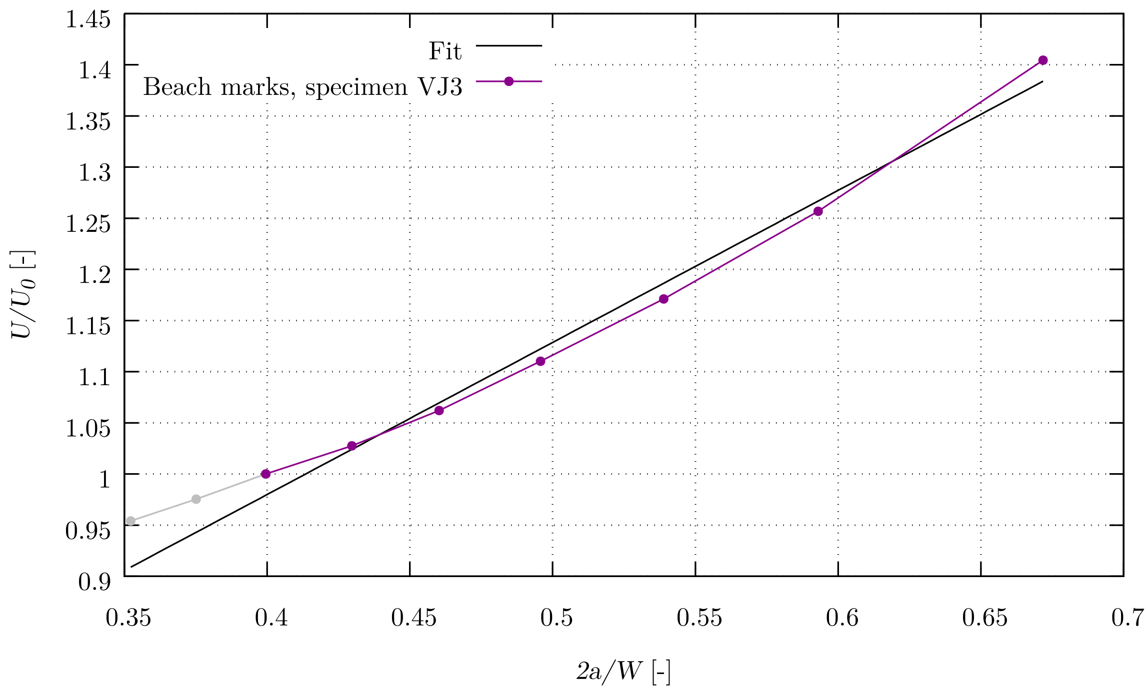

Figure 6.4 Calibration curve (Fit) for the M(T) specimen $VJ3$ obtained from beach marks.

Further a comparison between the obtained calibration curves and the analytical Johnson's equation is made whether Johnson's equation is applicable as calibration curve or not. In figure 6.6 and figure 6.7 Johnson's equation is shown for the M(T) and C(T) specimen, respectively, where Johnson's equation is obtained for the used specimen geometries as explained in section 2.3.2. It can be seen that Johnson's equation is neither applicable as a calibration curve for

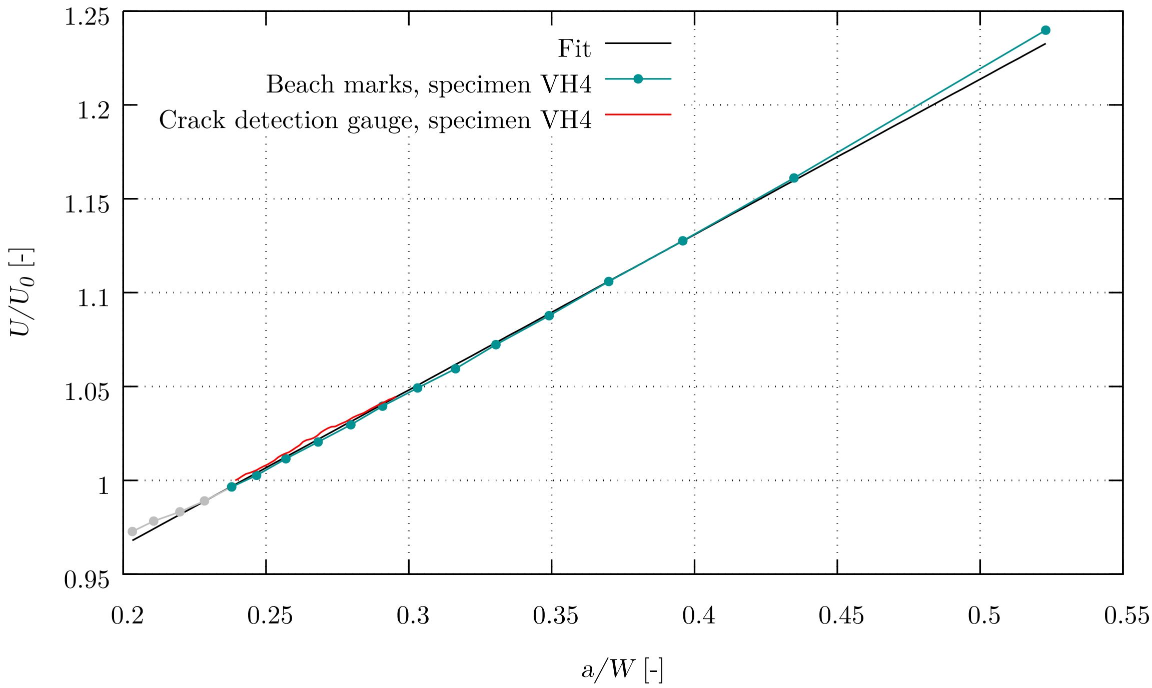

Figure 6.5 Calibration curve (Fit) for the C(T) specimen *VH*4 obtained from beach marks and crack detection gauge.

the M(T) specimen nor for the C(T) specimen because the deviation between both curves is not acceptable which would lead to a wrong calculated crack length.

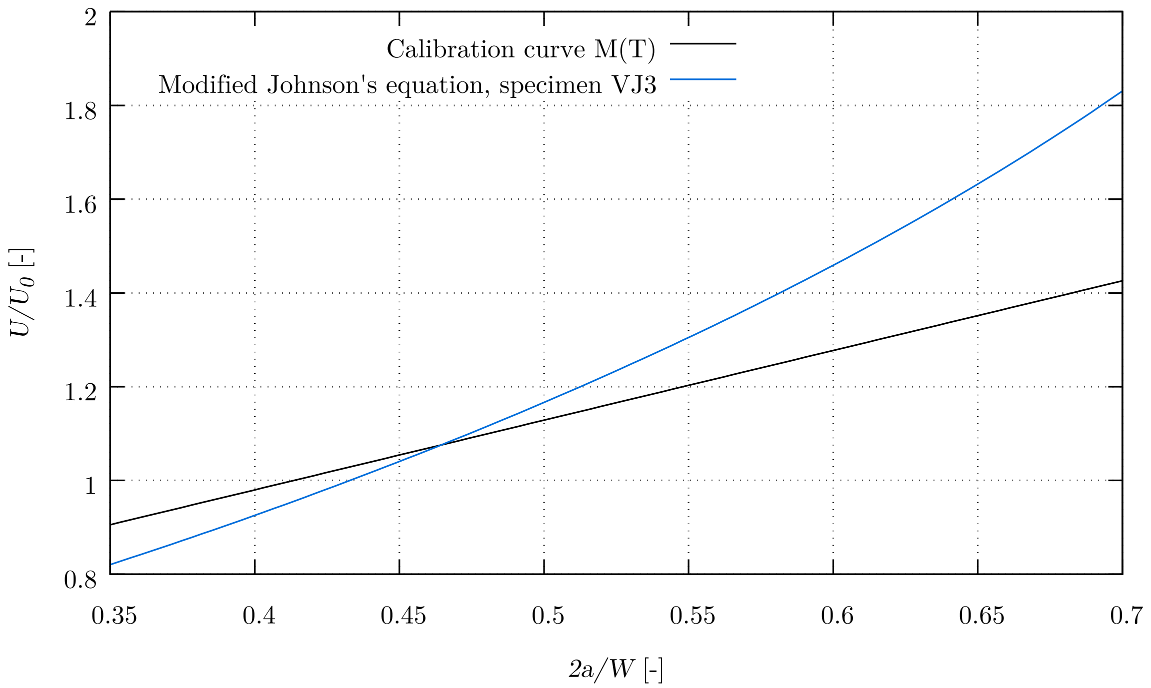

Figure 6.6 Comparison of modified Johnson's equation with created calibration curve for the M(T) specimen.

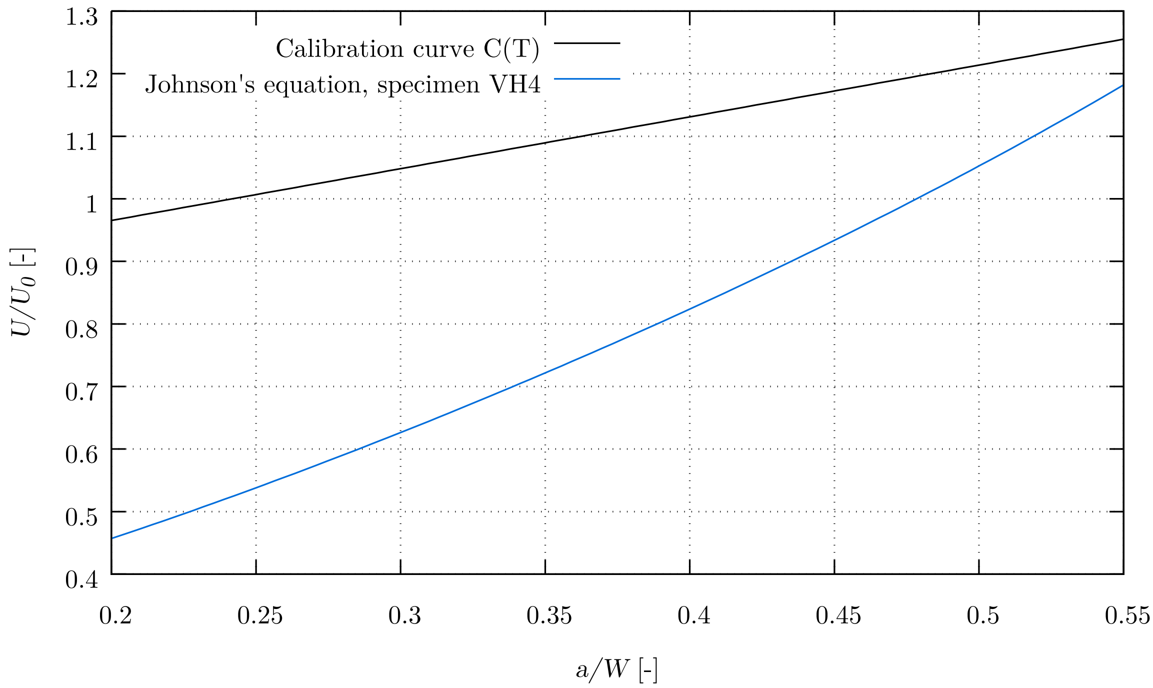

Figure 6.7 Comparison of Johnson's equation with created calibration curve for the C(T) specimen.

6.1.1 Crack growth

The crack lengths versus number of cycles for each specimen geometry are obtained with the associated calibration curves. They are shown in figure 6.8 and 6.9 for the M(T) and C(T) specimen, respectively. The data used to generate the crack length versus number of cycles plot is smoothed by a central moving average over 100 values for both specimen geometries. The crack length curve is created for the load ratio $R = 0.1$ thus the curve is interrupted where the load ratio switches to $R = 0.5$ or $R = 0.4$ for the M(T) or C(T) specimen, respectively. Because the used data is averaged the first and last 50 values of each load ratio block are not displayed. Also the crack growth curves are only shown where no influence of the specimen notch is expected.

It can be seen that for both specimen geometries the crack length increases with increasing number of cycles.

With these crack growth curves the fatigue crack growth rate da/dN as well as the stress intensity factor range ΔK are determined which is explained in the following section.

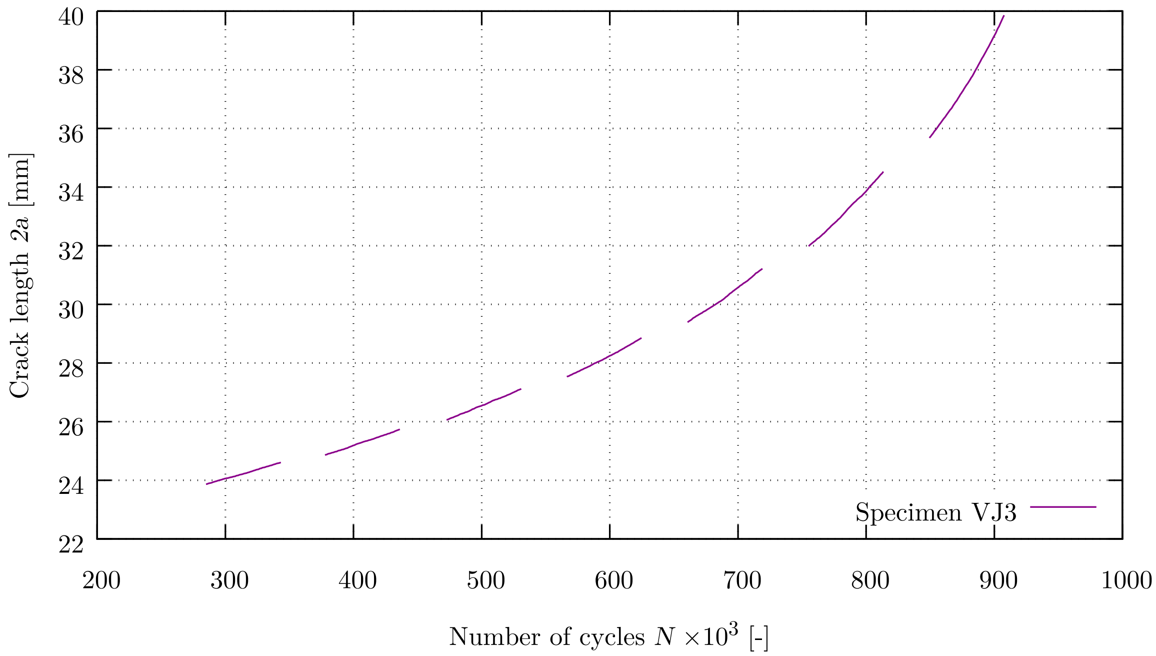

Figure 6.8 Crack growth versus number of cycles obtained from created calibration curve for the M(T) specimen at load ratio $R = 0.1$.

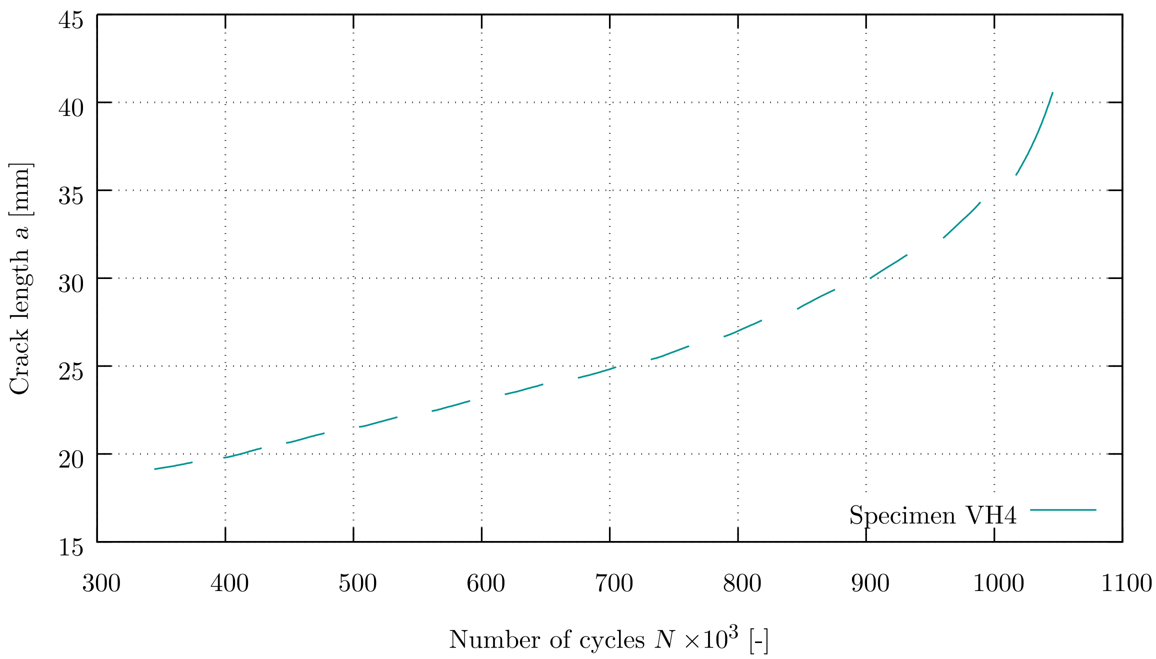

Figure 6.9 Crack growth versus number of cycles obtained from created calibration curve for the C(T) specimen at load ratio $R = 0.1$.

6.1.2 Fatigue crack growth rate

From the crack length versus number of cycles data the crack growth rate can be obtained by approaching the slopes with straight lines between two adjacent data points which is referred to as secant method. The increment between two points is calculated according to ASTM [ASTM 2015] as follows

$$\left(\frac{da}{dN}\right)_j = \frac{a_j - a_{j-1}}{N_j - N_{j-1}}, \tag{6.1}$$

where j is the point at the end of an increment, see figure 6.10. Each segment has a corresponding ΔK_j for which the average crack length a_{avg} of each segment is taken. This average crack length is calculated as

$$a_{avg} = \frac{a_j + a_{j-1}}{2}. \tag{6.2}$$

With the definition for ΔK, given in equation (2.17), using the gross section nominal stress $S_g = {}^{P}/_{2bt}$, see figure 2.6, where $2b = W$ for the M(T) specimen, and the geometry function F, given in equation (2.6), the stress intensity factor range for the M(T) specimen is calculated as

$$\Delta K_{j,M(T)} = \frac{\Delta P}{t}\sqrt{\frac{\pi\alpha_{avg}}{2W}\sec\frac{\pi\alpha_{avg}}{2}}, \tag{6.3}$$

where $\alpha_{avg} = {}^{2a_{avg}}/_{W}$.

With the definition for ΔK, given in equation (2.18), and the geometry function F_p, given in equation (2.8), the stress intensity factor range for the C(T) specimen is calculated as

$$\Delta K_{j,C(T)} = \frac{\Delta P}{t\sqrt{W}}\frac{(2+\alpha_{avg})}{(1-\alpha_{avg})^{3/2}}\cdot(0,886 + 4,64\alpha_{avg} - 13,32\alpha_{avg}^2 + 14,72\alpha_{avg}^3 - 5,6\alpha_{avg}^4), \tag{6.4}$$

where $\alpha_{avg} = {}^{a_{avg}}/_{W}$.

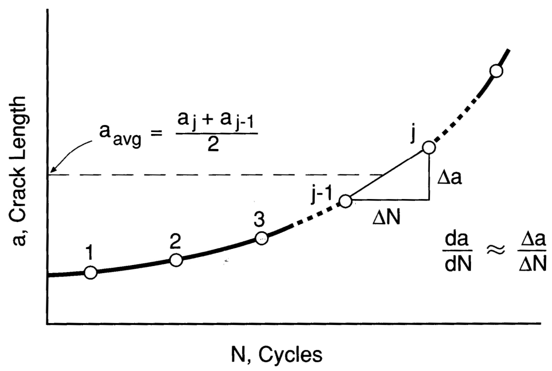

Figure 6.10 Calculation of crack growth rate, taken from Dowling [Dowling 1998].

To determine the fatigue crack growth rate ${}^{da}/_{dN}$ versus stress intensity factor range ΔK for the M(T) specimen for each load ratio block two crack growth rate and ΔK values are used with a crack length increment of more than $\Delta a = 0.25$ mm as recommended in ASTM [ASTM 2015]. For the C(T) specimen only one ${}^{da}/_{dN}$ and ΔK value is used for each load ratio block. In figure 6.11 one load ratio block of the M(T) specimen from the crack length versus number of cycles plot, figure 6.8, is shown where the used da/dN, $2a_{avg}$ and corresponding ΔK values are schematically indicated.

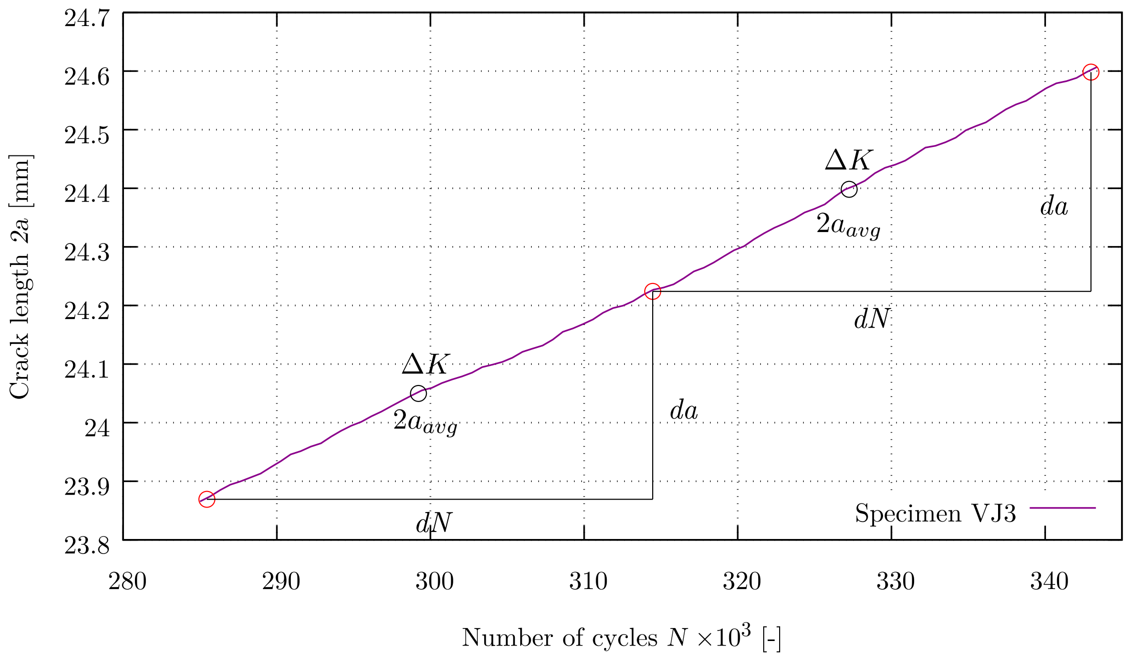

Figure 6.11 Calculation of the crack growth rate for the first load ratio block of the M(T) specimen $VJ3$ with corresponding ΔK and $2a_{avg}$.

For the M(T) and C(T) specimens the obtained fatigue crack growth rate da/dN versus the stress intensity factor range ΔK is shown in a double logarithmic plot in figure 6.12. The data for the M(T) and C(T) specimens is given in table B.2 and B.5 in appendix B.1 and B.2, respectively. In addition the stress intensity factor range versus the corresponding average crack length is shown in figure B.1 and B.4 for the M(T) and C(T) specimen, respectively.

For the M(T) specimen ΔK is in a range between 13.9 and 22.2 MPa$\sqrt{\text{m}}$ and for the C(T) specimen between 16.1 and 32.0 MPa$\sqrt{\text{m}}$. These ΔK values represent region II of the fatigue crack growth curve, as explained in section 2.2.3, so the data is fitted with the Paris equation (2.20). The material constants of the Paris equation obtained for the M(T) and C(T) specimens are listed in table 6.1.

Table 6.1 Paris constants obtained for the M(T) and C(T) specimens.

Specimen	C $\left[\frac{\text{mm/cycle}}{(\text{MPa}\sqrt{\text{m}})^m}\right]$	m [-]
M(T)	$3.83 \cdot 10^{-10}$	3.73
C(T)	$2.73 \cdot 10^{-10}$	3.83

The British Standard Institution 6.13 divides the fatigue crack growth rate curve into two stages A and B, depicted in figure 6.13 and recommends constants for the Paris equation for steels with a yield strength of ≤ 700 MPa and an operating temperature up to 100 °C in air or non-aggressive environment for $R < 0.5$. These constants are listed in table 6.2.

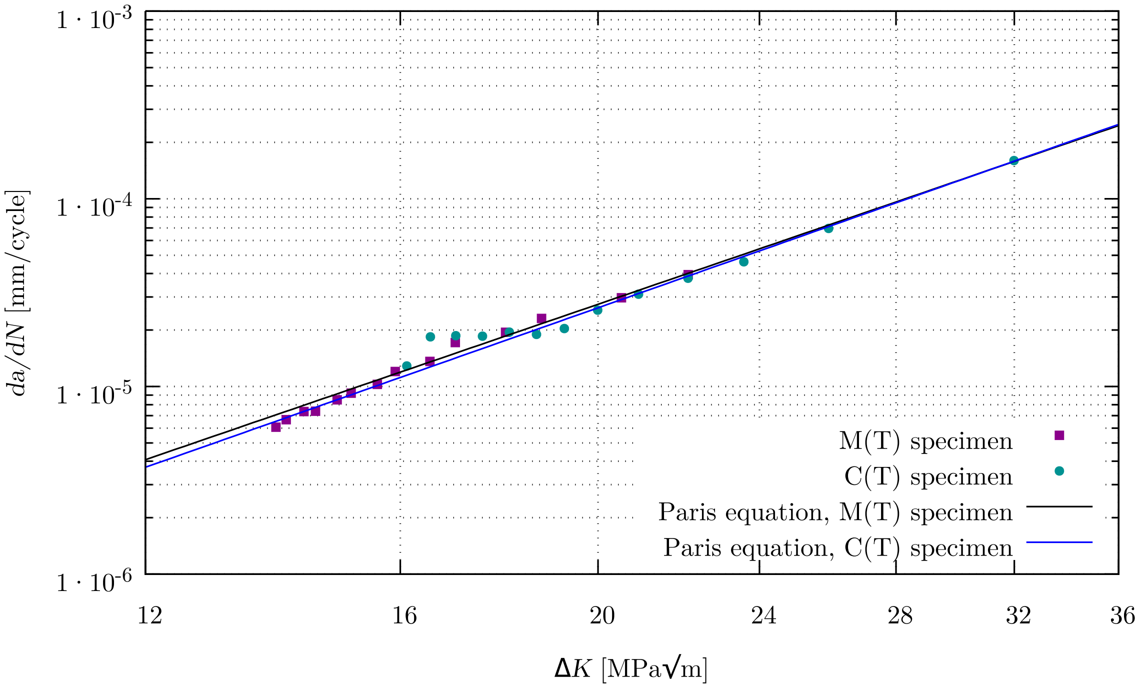

Figure 6.12 Fatigue crack growth rate da/dN versus stress intensity factor range ΔK for M(T) and C(T) specimens as well as the Paris equation with the parameters $C = 3.83 \cdot 10^{-10}$ and $m = 3.73$ (M(T)) and $C = 2.73 \cdot 10^{-10}$ and $m = 3.83$ (C(T)).

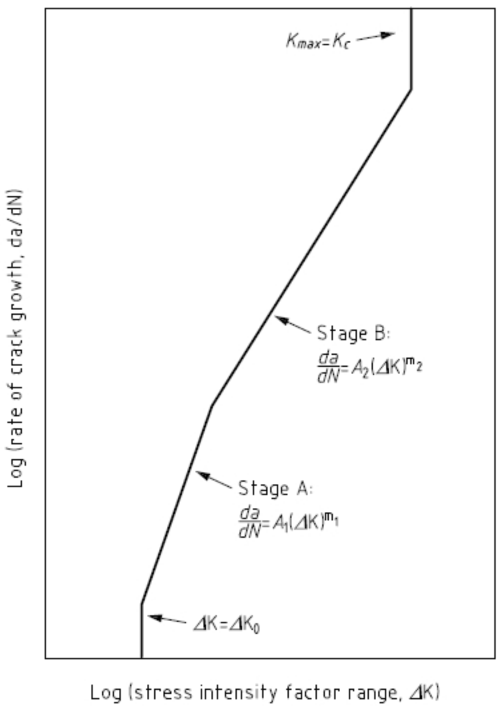

Figure 6.13 Two stages of crack growth according to the British Standards Institution [British Standards Institution 2005].

Table 6.2 Paris constants recommended by the British Standard Institution [British Standards Institution 2005] for stage A and B.

Stage	C $\left[\frac{\text{mm/cycle}}{(\text{MPa}\sqrt{\text{mm}})^m}\right]$	m [-]
A	$1.21 \cdot 10^{-26}$	8.16
B	$3.98 \cdot 10^{-13}$	2.88

In this thesis the simple Paris equation is taken where only one curve is used, thus the obtained Paris curves of both specimen geometries lie below the recommended curves.

In figure 6.12 discrepancies in fatigue crack growth rates between both specimen geometries are identified. The fatigue crack propagation rate da/dN for the M(T) specimen is slightly higher for the same stress intensity factor until a value of about $\Delta K = 32\,\text{MPa}\sqrt{\text{m}}$ where the Paris fit curves are crossing.

These results are compared to literature in the following.

In figure 6.14 the fatigue crack growth rate versus stress intensity factor range data obtained in four different literature studies are depicted. In Varfolomeev [Varfolomeev et al. 2011] the fatigue crack growth rate curves are obtained for the steel EA4T with a yield strength of 522 MPa. In Seitl [Seitl et al. 2008] the fatigue crack growth rate curve is obtained for the steel 12050 with a yield strength of 350 MPa where also another steel is investigated that shows the same behaviour, in Hutař [Hutař et al. 2006] a steel with yield strength of 220 MPa is used and in Tong [Tong 2002] the crack growth rates are investigated for a mild steel. In Varfolomeev [Varfolomeev et al. 2011] and Seitl [Seitl et al. 2008] the fatigue crack growth rates at about $\Delta K = 11\,\text{MPa}\sqrt{\text{m}}$ for M(T) specimens lie above the ones for C(T) specimens where the crack growth rates are approaching each other for higher ΔK values. It is found that the threshold region for the M(T) specimen is lower than for the C(T) specimen.

In Hutař [Hutař et al. 2006] the fatigue crack growth rates for higher ΔK values are not approaching, but the threshold region for the C(T) specimens lies at higher stress intensity factor range values, as also found in Varfolomeev [Varfolomeev et al. 2011] and Seitl [Seitl et al. 2008]. In Tong [Tong 2002] a reversed trend is found for the M(T) and C(T) specimens.

Differences in the findings in literature show the complexity of the issue. The experiments performed in this thesis conducted with the DCPD main configuration use only one test specimen for each geometry. Therefore the obtained results should be regarded with caution. Also tests at a lower ΔK range are not performed in this thesis as well as experiments to determine a threshold value with a K decreasing test. Further studies will reduce the uncertainty of the obtained results.

However, there is a difference in the fatigue propagation rate between the M(T) and C(T) specimens and the T_{stress}, see section 2.2.4, is used to account for the different specimen shapes which is elaborated in the following section.

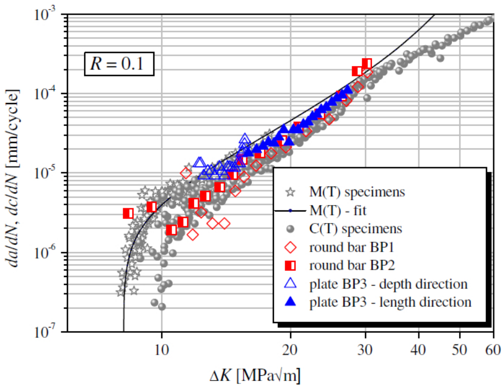

(a) [Varfolomeev et al. 2011]

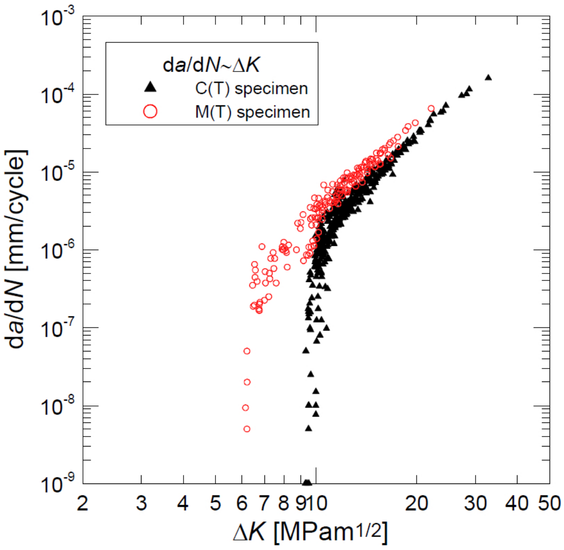

(b) [Seitl et al. 2008]

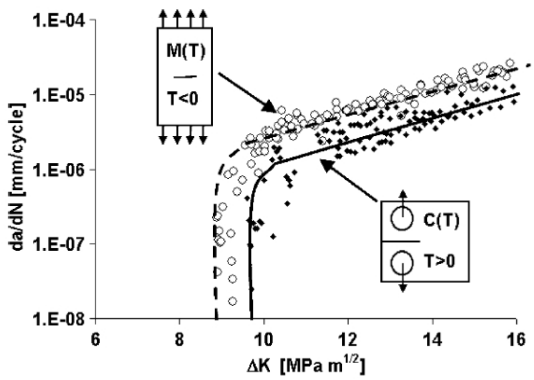

(c) [Hutař et al. 2006]

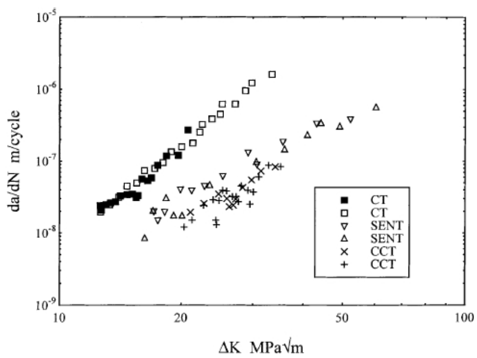

(d) [Tong 2002]

Figure 6.14 Fatigue crack growth rate versus stress intensity factor range for M(T) and C(T) specimens obtained by Varfolomeev [Varfolomeev et al. 2011], Seitl [Seitl et al. 2008], Hutař [Hutař et al. 2006] and Tong [Tong 2002].

Constraint effect

In this section it is tried to apply the findings of Hutař [Hutař et al. 2006] to obtain a material curve independent of the geometrical shape of a specimen, see section 2.2.4. Therefore the biaxiality factor B, determined in Sherry [Sherry et al. 1995], is used to calculate the T_{stress} which is then taken to determine a new material curve.

The biaxiality factor B for the two different specimen geometries considered in this investigation are obtained according to the estimations of Sherry [Sherry et al. 1995] and a polynomial of fourth order with the constants given in table 2.1 and 2.2, see section 2.2.4, is calculated. The biaxiality factor B for the three different calculation methods a, b and c) is shown in figure 6.15 and 6.16 for the M(T) and C(T) specimens, respectively. With the calculated T_{stress} an effective stress intensity factor range ΔK^{eff} is determined for each specimen geometry. In figure 6.17 the fatigue crack growth rate versus effective stress intensity factor range is shown for the M(T) and C(T) specimens where the biaxiality factor is determined with method a). The data of B and ΔK^{eff} for all three methods are listed in table B.2 and table B.5 in appendix B.1 and B.2 for the M(T) and C(T) specimens, respectively. The difference between these methods is small, so only method a) is depicted. The obtained data is fitted with the Paris equation and the constants $C = 5.20 \cdot 10^{-10}$ and $m = 3.53$ for the M(T) specimen and $C = 2.20 \cdot 10^{-10}$ and $m = 3.93$ for the C(T) specimen are obtained. Points corresponding to a low level of constraint (M(T)) are shifted to a smaller da/dN and points corresponding to a high level of constraint (C(T)) are shifted to a higher da/dN in comparison with data depicted in figure 6.12. The data can now be approximated by only one experimental curve, but in this special case this approach is not leading to an improved situation because the data for the M(T) and C(T) specimens is drifting apart. Hence for this approach more experimental data is needed as already mentioned in the previous section.

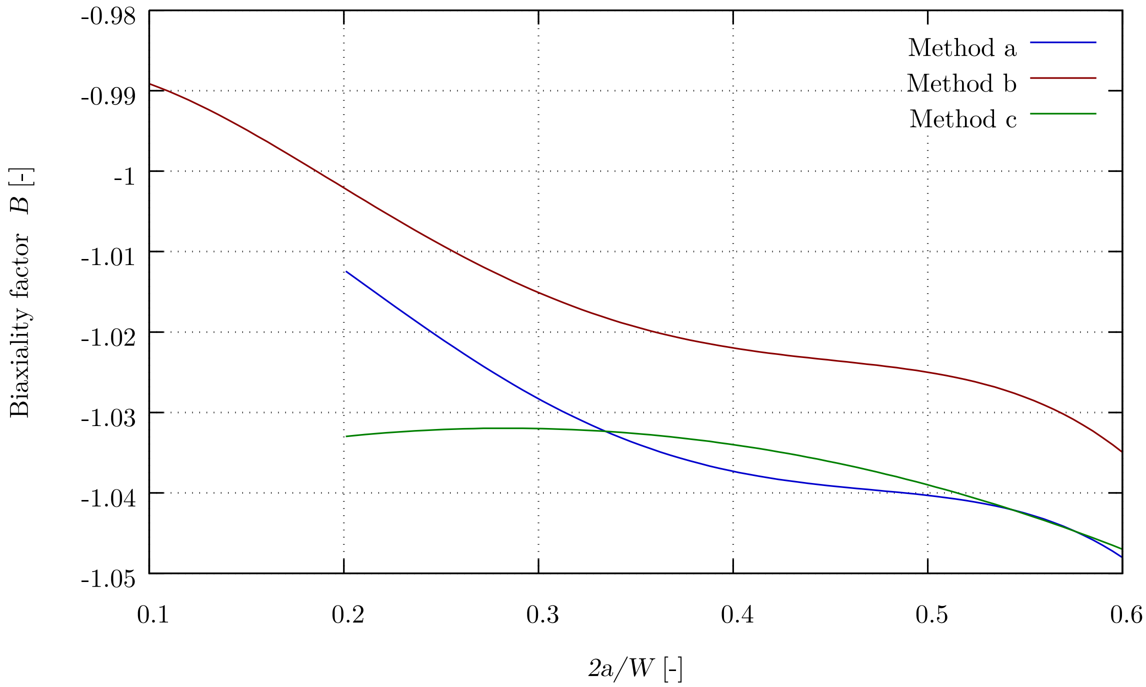

Figure 6.15 Biaxiality factor B of the M(T) specimen as estimated in Sherry [Sherry et al. 1995].

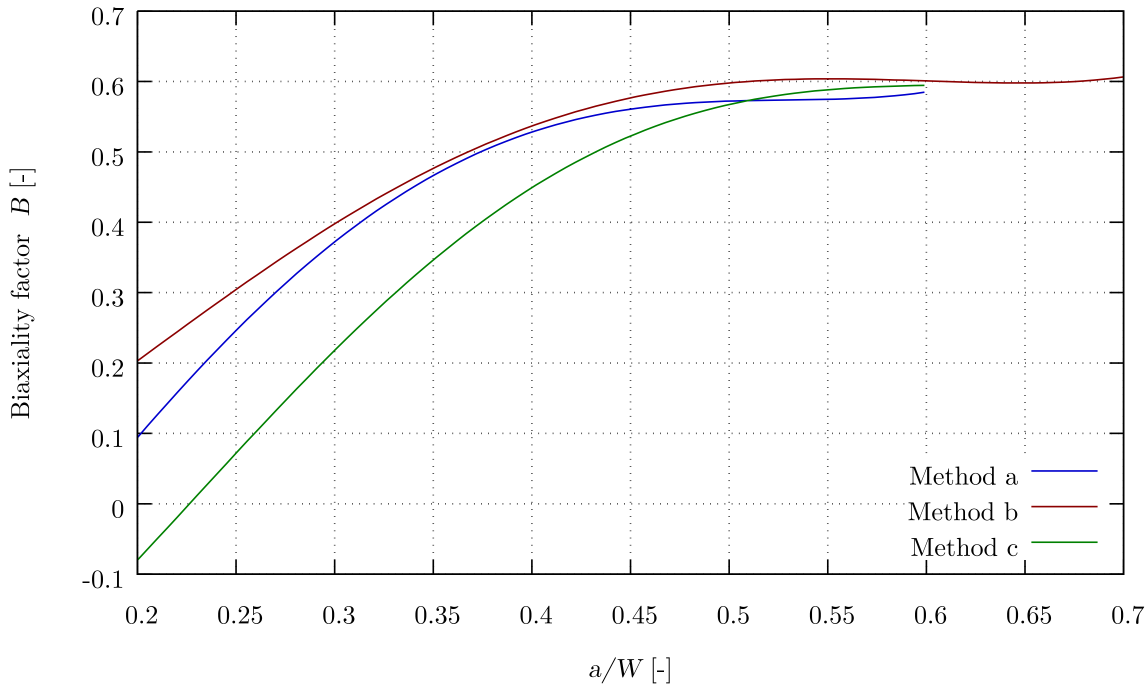

Figure 6.16 Biaxiality factor B of the C(T) specimen as estimated in Sherry [Sherry et al. 1995].

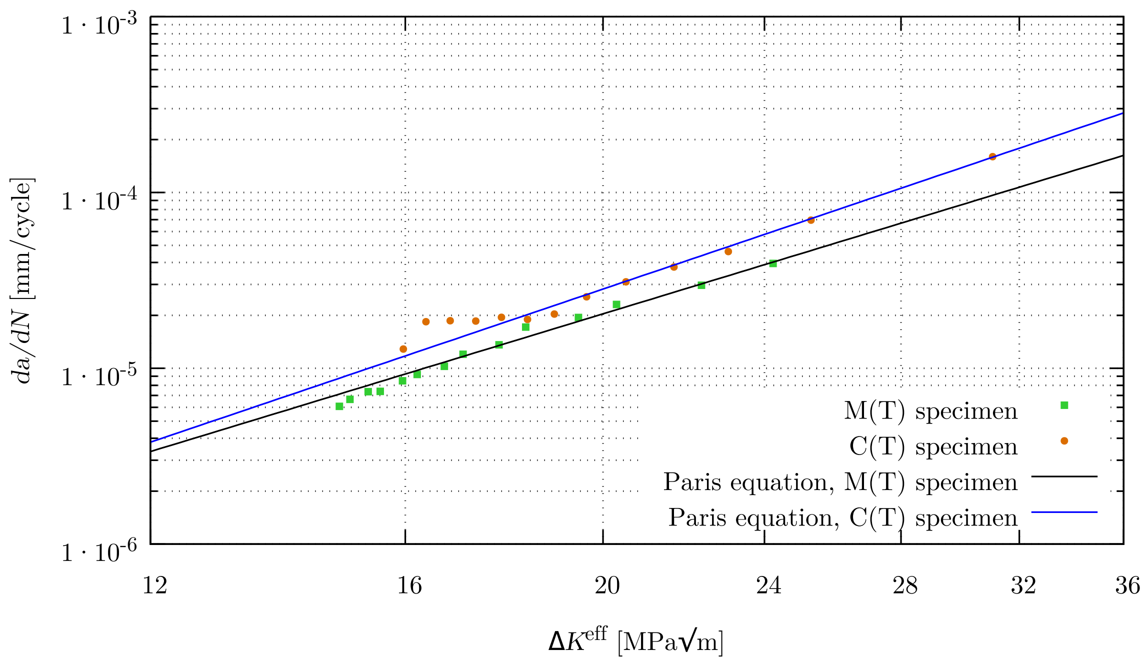

Figure 6.17 Effective stress intensity factor range ΔK^{eff} versus fatigue crack growth rate of the M(T) and C(T) specimen with Paris equations. The corresponding parameters of the Paris equation are $C = 5.20 \cdot 10^{-10}$ and $m = 3.53$ (M(T)) and $C = 2.20 \cdot 10^{-10}$ and $m = 3.93$ (C(T)).

Chapter 7

Summary and Conclusion

The main objective of this work is to investigate the geometry influence of two different test specimen geometries on fatigue crack growth behaviour. Furthermore the implementation of the direct current potential drop method is optimised in view of investigations at low temperatures.

During the first preliminary tests the experimental setup as well as the configuration of the direct current potential drop (DCPD) method is tested and parameters, as for instance the current input wire locations, are adjusted. Main result of these first preliminary tests is an initial configuration of the DCPD method. Using this configuration seven specimens are tested, four M(T) und two C(T) specimens. During these tests problems of specimen positioning between the clamps of the resonant testing machine are faced, thus data of incorrectly clamped specimens are not used for further investigations. Furthermore the recording time of the measuring system is adjusted. With two M(T) and two C(T) specimens a calibration curve for the DCPD method is made, where beach marks as well as crack detection gauges are used. It is found that the noise of the potential measurements is too large to obtain physical correct fatigue crack growth rate data. These findings lead to the implementation of a new configuration of the DCPD method. This configuration is tested with one M(T) and one C(T) specimen where a sufficient noise reduction is obtained. Therefore a calibration curve for each specimen geometry is made to relate the crack growth with the voltage drop measurements. These calibration curves are compared to the analytical Johnsons's equation and it is found that the analytical approach is not applicable. Fatigue crack growth data is calculated and fitted with Paris' equation where the corresponding constants are obtained. These constants are compared to the recommendations given by the British Standards Institution [British Standards Institution 2005].

Discrepancies in the fatigue crack growth data of the M(T) and C(T) specimens are found and the obtained results are compared to literature. Furthermore, to gain more reliable estimates of the residual life of structures a new material curve is created which is independent of the specimen geometry as given in Hutař [Hutař et al. 2006] which is not leading to satisfactory results.

The main configuration of the DCPD method gives acceptable results, thus this configuration can be used for further tests at low temperatures. However, the obtained results of the main configuration regarding the fatigue crack growth behaviour should be treated with caution due to a very low number of tested specimens.

Chapter 8

Recommendations for future work

The findings of the implementation of the main configuration of the DCPD method show that it is capable of producing accurate potential measurements for fatigue crack growth experiments. However, the quality of the obtained results of the main configuration regarding the fatigue crack growth data can still be improved.

To make a general statement of the specimen geometry influence on the fatigue crack growth behaviour it is necessary to repeat the experiments with more than one specimen per tested geometry.

The resonant testing machine is designed for a maximum load of about 250 kN, which is about 100 times the minimal applied load for the C(T) specimen. This leads to reduced precision regarding the applied loads on the C(T) specimen compared to the M(T) specimen. Figure B.7 a) compared to B.3 a) shows this reduction in precision in unsteady load values. This problem could be evaded with the use of specimens of a greater thickness that are tested with higher loads.

Further improvements might be obtained by using an alternative approach to determine the crack lengths from the beach marks. The used method is the one recommended by ASTM [ASTM 1997], using an averaged value of three measurement points. With high definition photography it is possible to determine the area of every block on the fracture surface and to calculate the average crack lengths by dividing the added-up areas by the thickness of the specimen.

Moreover the used approach to account for the geometry influence of the test specimens regarding the life prediction of structures is one of several given in literature. Since the results of this approach are not promising others may be tested with the given experimental setup.

Bibliography

Alvaro, Antonio, Odd M. Akselsen, Xiaobo Ren, and Alexander Kane (2014). “Fundamental Aspects of Fatigue of Steel in Arctic Applications”. In: *Proceedings of the Twenty-fourth International Ocean and Polar Engineering Conference.*

Anctil, Albert A., Eric B. Kula, and Eugene DiCesare (1964). *Electric-Potential Technique for Determining Slow Crack Growth.* U.S. Army Material Research Agency.

Aronson, G. H. and R. O. Ritchie (1979). “Optimization of the Electrical Potential Technique for Crack Growth Monitoring in Compact Test Pieces Using Finite Element Analysis”. In: *Journal of Testing and Evaluation* Vol. 7.4, pp. 208 - 215.

ASTM (1997). *ASTM 399-90: Standard Test Method for Plane-Strain Fracture Toughness of Metallic Materials.* ASTM International.

ASTM (2015). *ASTM E647-15: Standard Test Method for Measurement of Fatigue Crack Growth Rates.* ASTM International. DOI: 10.1520/E0647-15.

British Standards Institution (2005). *Guide to methods for assessing the acceptability of flaws in metallic sctructures: British standard BS 7910:2005.* BSI British Standards Institution.

Dowling, Norman E. (1998). *Mechanical Behavior of Materials: Engineering Methods for Deformation, Fracture, and Fatigue (2nd Edition).* Prentice Hall. ISBN: 0-13-905720-X.

Hartmann, G. A. and D. A. Johnson (1987). “D-C Electric-Potential Method Applied to Thermal/Mechanical Fatigue Crack Growth”. In: *Experimental Mechanics*, pp. 106–112.

Hill, Michael R. and Daniel H. Stuart (2012). “Direct current potential difference correlation for open-hole single-crack coupons”. In: *Engineering Fracture Mechanics* Vol. 99, pp. 141–146. DOI: 10.1016/j.engfracmech.2012.11.019.

Hutař, Pavel, Stanislav Seitl, and Zdeněk Knésl (2006). “Effect of constraint on fatigue crack propagation near threshold in medium carbon steel”. In: *Computational Materials Science* Vol. 37, pp. 51–57. DOI: 10.1016/j.commatsci.2005.12.025.

Larsson, S.G. and A.J. Carlsson (1973). “Influence of non-singular stress terms and specimen geometry on small-scale yielding at crack tips in elastic-plastic materials”. In: *Journal of the Mechanics and Physics of Solids* Vol. 21.4, pp. 263–277. ISSN: 0022-5096. DOI: 10.1016/0022-5096(73)90024-0.

Leevers, P. S. and J. C. Radon (1982). “Inherent stress biaxiality in various fracture specimen geometries”. In: *International Journal of Fracture* Vol. 19, pp. 311–325.

Lu, Kai and Toshiyuki Meshii (2015). “A systematic investigation of T-stresses for a variety of center-cracked tension specimen”. In: *Theoretical and Applied Fracture Mechanics* Vol. 77, pp. 74–81. DOI: 10.1016/j.tafmec.2015.02.001.

Pollock, Daniel D. (1985). *Thermoelectricity: Theory, Thermometry, Tool. ASTM STP 852*. Astm Intl. ISBN: 0-8031-0409-X.

Ritchie, R. O., G. G. Garrett, and J.F. Knott (1971). "Crack-Growth Monitoring: Optimisation of the Electrical Potential Technique using an Analogue Method". In: *International Journal of Fracture Mechanics* Vol. 7, pp. 462–467.

Schijve, J. (2008). *Fatigue of Structures and Materials*. Springer. ISBN: 978-1-4020-6807-2.

Schwalbe, K. H. and D. Hellmann (1981). "Application of the Electrical Potential Method to Crack Length Measurements Using Johnson's Formula". In: *Journal of Testing and Evaluation* Vol. 9, pp. 218–221.

Seitl, Stanislav, Pavel Hutař, and Zdeněk Knésl (2008). "Sensitivity of Fatigue Crack Growth Data to Specimen Geometry". In: *Key Engineering Materials* Vol. 385-387, pp. 557–560. DOI: 10.4028/www.scientific.net/KEM.385-387.557.

Sherry, A. H., C. C. France, and M. R. Goldthorpe (1995). "Compendium of T-stress solutions for two and three dimensional cracked geometries". In: *Fatigue & Fracture of Engineering Materials and Structures* Vol. 18.1, pp. 141–155. DOI: 10.1111/j.1460-2695.1995.tb00148.x.

Srawley, J. E. (1976). "Wide Range Stress Intensity Factor Expression for ASTM E399 Standard Fracture Toughness Specimens". In: *International Journal of Fracture Mechanics* Vol. 12, pp. 475-476.

Tada, Hiroshi, Paul C. Paris, and George R. Irwin (2000). *Stress Analysis of Cracks Handbook*. ASME INTL. ISBN: 0-7918-0153-5.

Tong, Jie (2002). "T-stress and its implications for crack growth". In: *Engineering Fracture Mechanics* Vol. 69, pp. 1325–1337. DOI: 10.1016/S0013-7944(02)00002-4.

Varfolomeev, I., M. Luke, and M. Burdack (2011). "Effect of specimen geometry on fatigue crack growth rates for the railway axle material EA4T". In: *Engineering Fracture Mechanics* Vol. 78.5, pp. 742–753. DOI: 10.1016/j.engfracmech.2010.11.011.

Varfolomeev, I., Michael Luke, and Sergii Moroz (2010). "Experimental and numerical investigations of fatigue crack growth in various specimen geometries". In: *Procedia Engineering* Vol. 2, pp. 1829–1837. DOI: 10.1016/j.proeng.2010.03.197.

Walters, Carey Leroy, Antonio Alvaro, and Johan Maljaars (2016). "The effect of low temperatures on the fatigue crack growth of S460 structural steel". In: *International Journal of Fatigue* Vol. 82, pp. 110–118. DOI: 10.1016/j.ijfatigue.2015.03.007.

Walters, Carey Leroy and Lars O. Voormeeren (2013). "Minimum fatigue Pre-crack extension for fracture testing". In: *ASME 2013 Pressure Vessels and Piping Conference*. DOI: 10.1115/pvp2013-97041.

Williams, M. L. (1957). "On the stress distribution at the base of a stationary crack". In: *Journal of Applied Mechanics* Vol. 24, pp. 109–114.

Appendix A

Design drawings

In figure A.1 the design drawing of the C(T) specimen and in figure A.2 the design drawing of the associated clevis is shown. In figures A.3 to A.5 design drawings of the loading pin, the distance disc, the bolt and the welding template for the C(T) specimen are depicted.

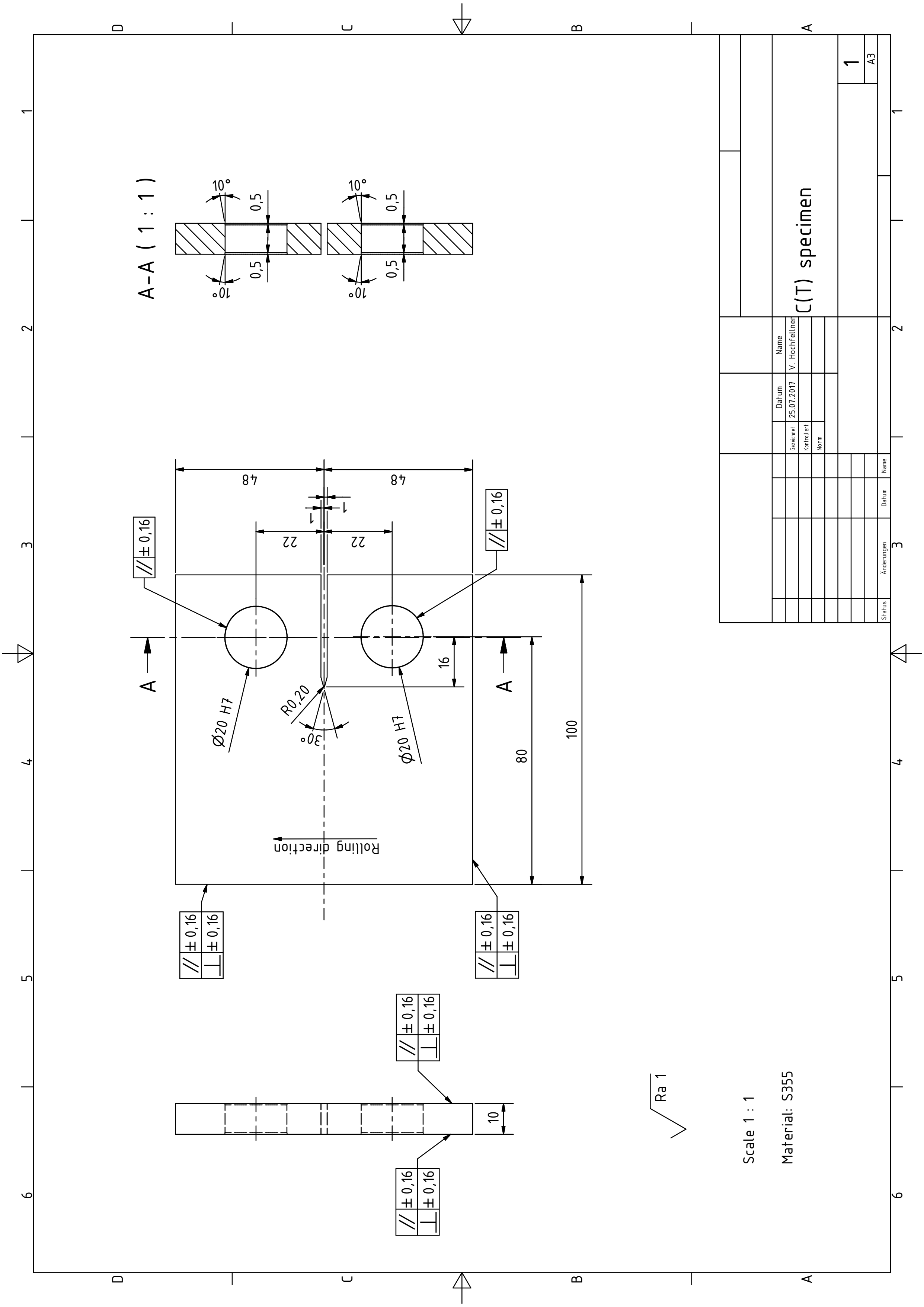

Figure A.1 C(T) specimen design drawing.

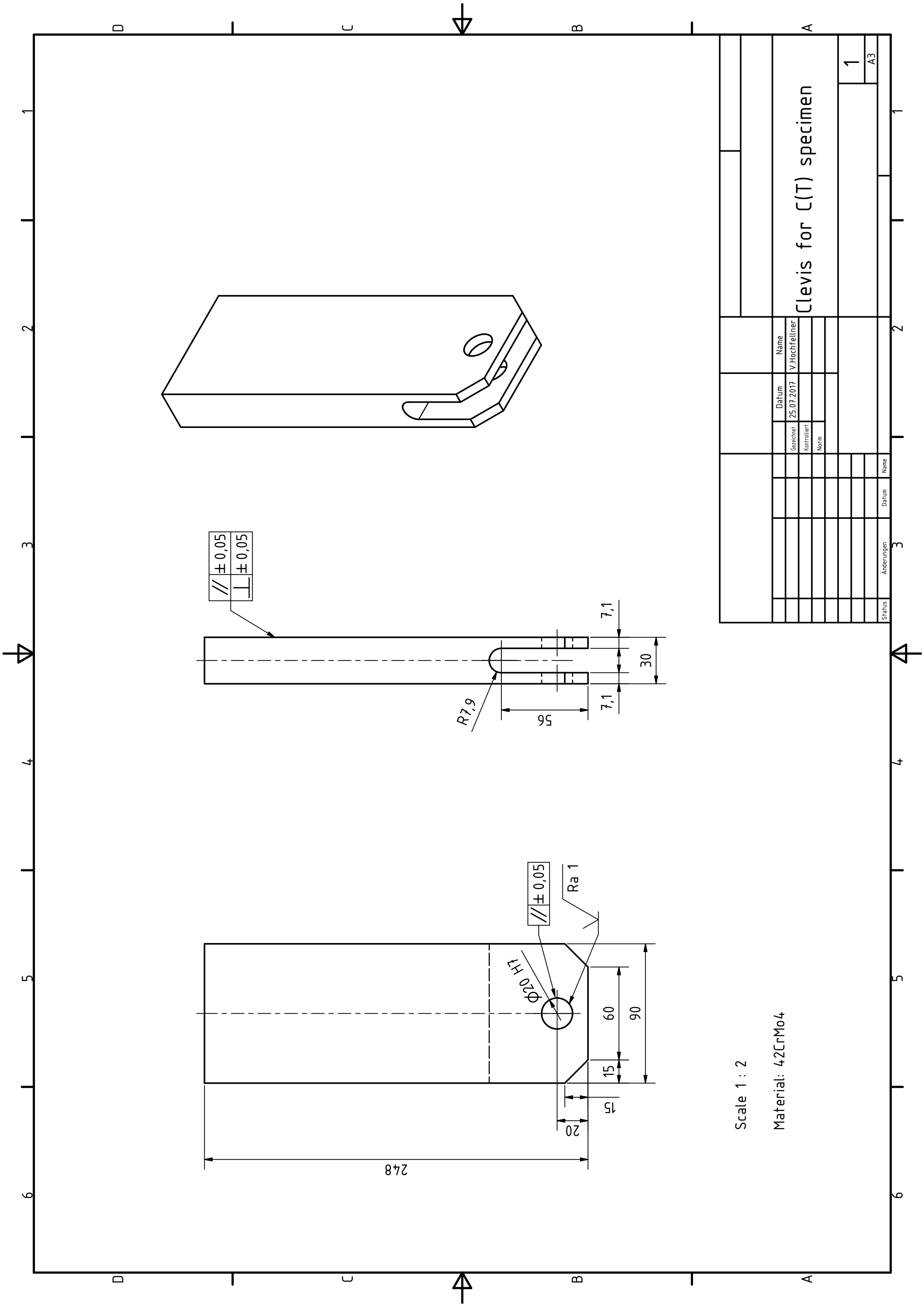

Figure A.2 C(T) specimen clevis design drawing.

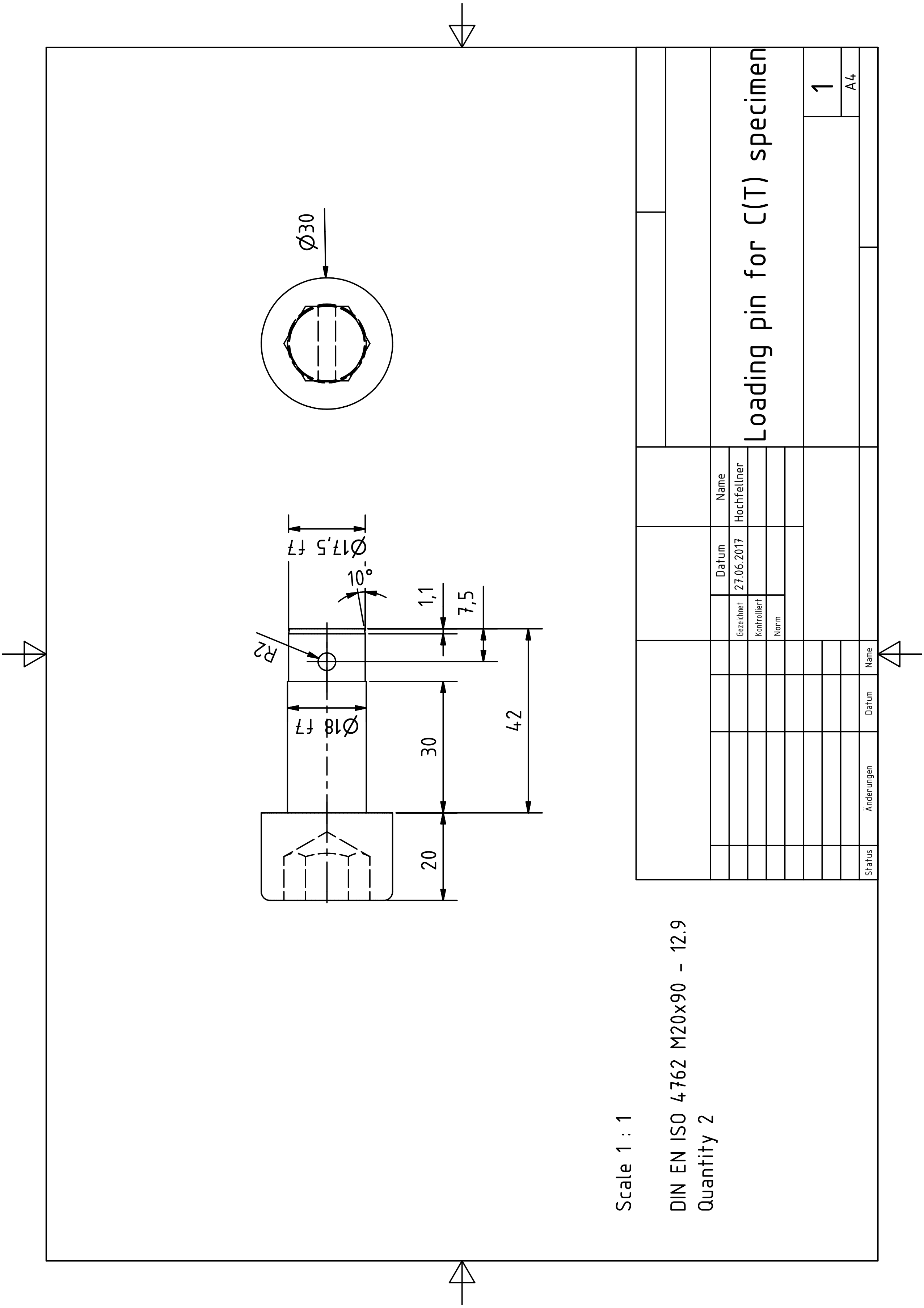

Figure A.3 DIN EN ISO 4762 M20x90 - 12.9 screw used as loading pin.

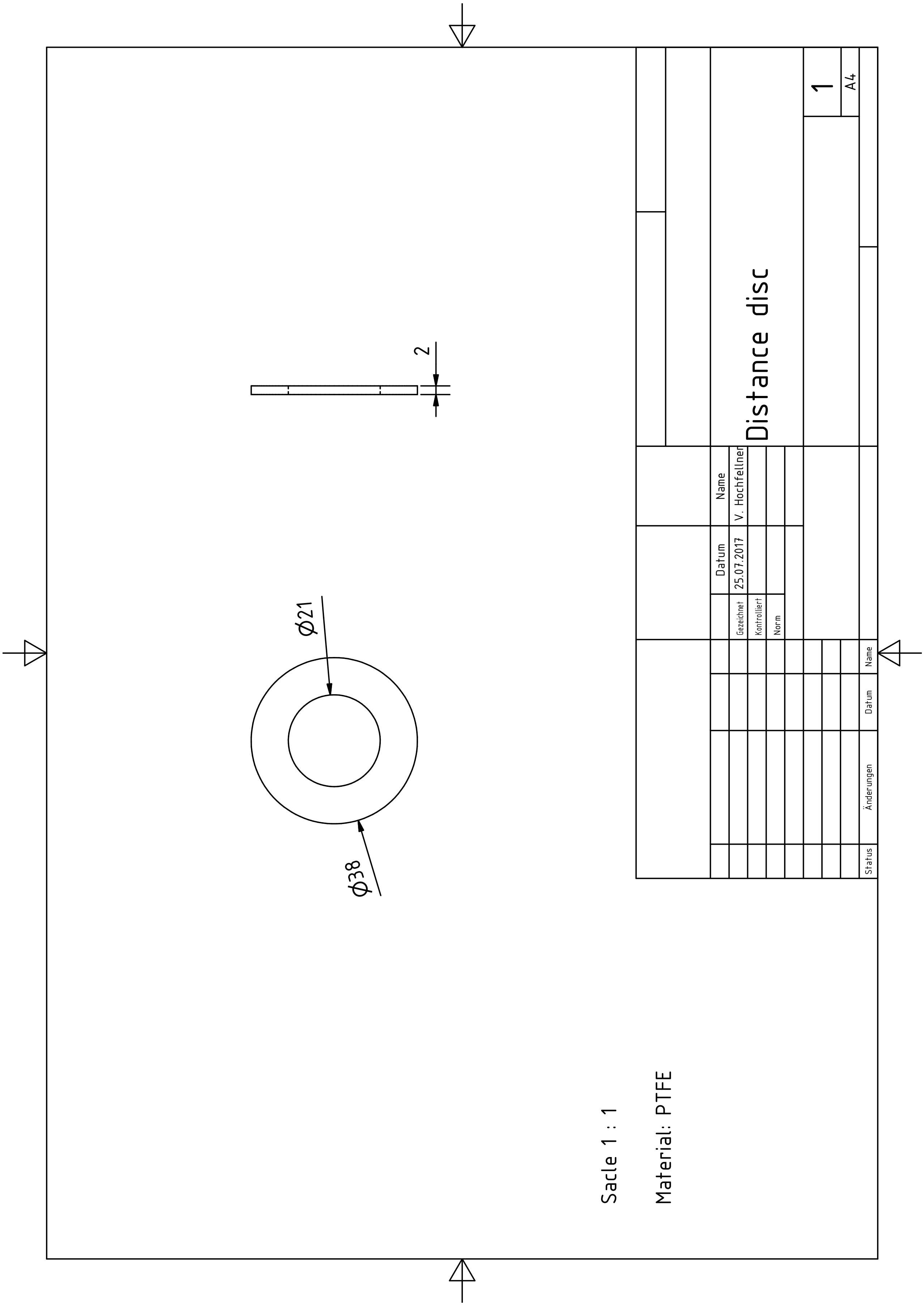

Figure A.4 Distance disc design drawing.

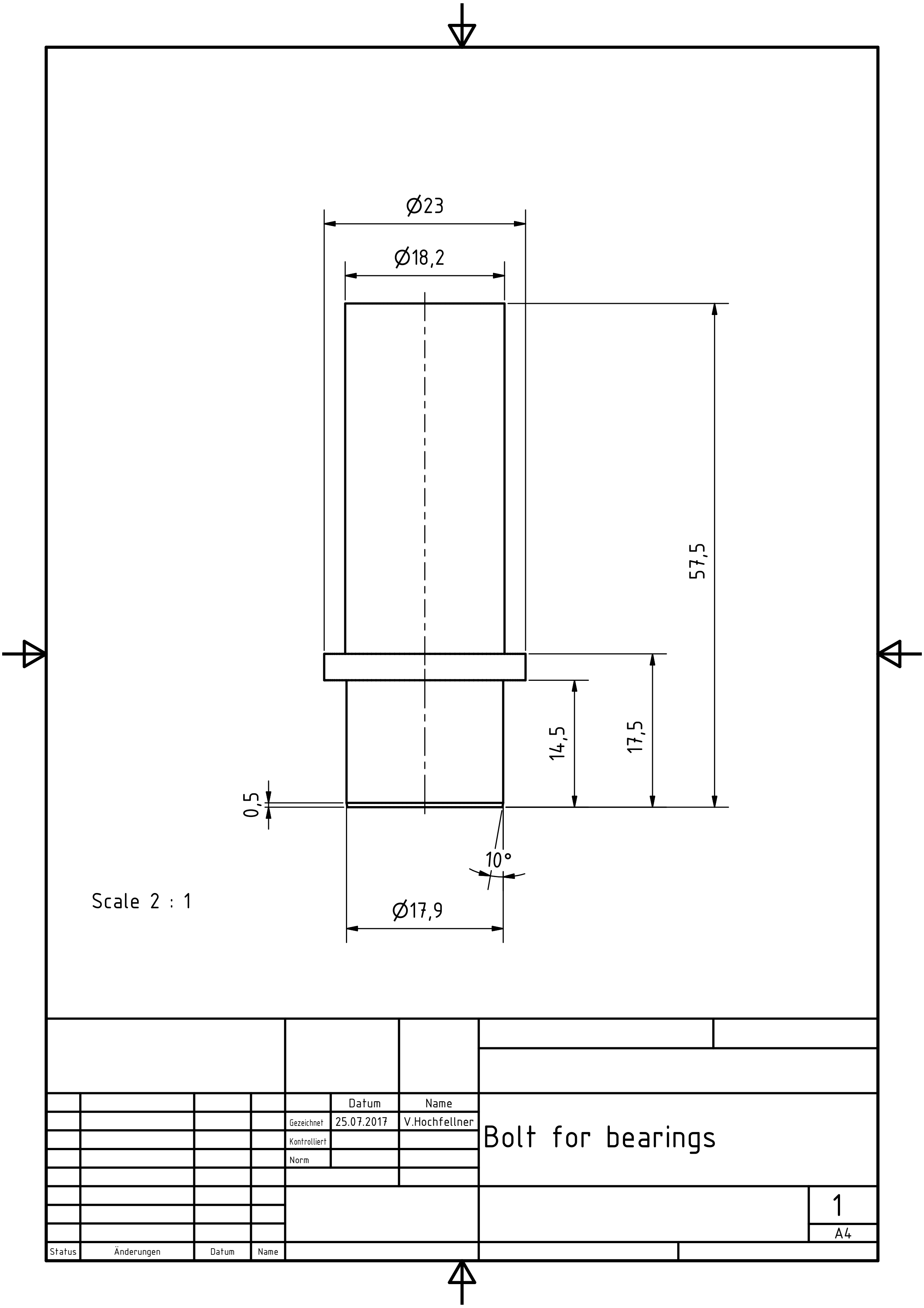

Figure A.5 Design drawing of bolt for bearings.

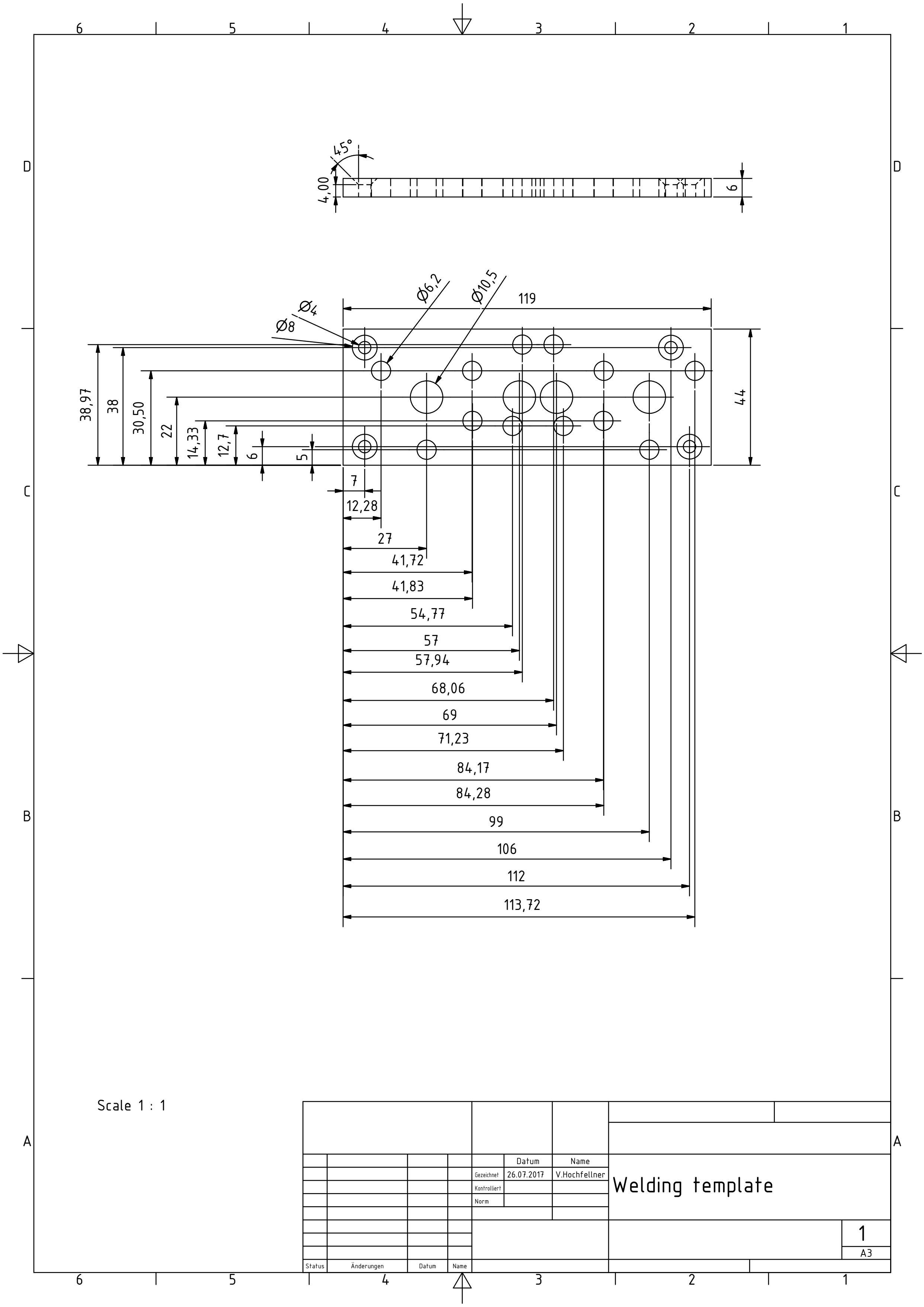

Figure A.6 Design drawing of welding template for the C(T) specimen.

Appendix B

Data of used test specimens

In table B.1 and B.4 the data of the used M(T) and C(T) specimens for the experiments are listed, respectively. In table B.2 and table B.5 the obtained data for fatigue crack growth rate curves are given and in figure B.1 and B.4 the average crack length versus stress intensity factor range is shown for the M(T) and C(T) specimen, respectively. In table B.3 and B.6 the biaxiality factor as well as the effective stress intensity factor range is given for the M(T) and C(T) specimen, respectively, for the three calculating methods a), b) and c).

In figure B.2 the applied load as well as voltage drop readings are shown for specimen $VJ1$. In figure B.3 the applied load of specimen $VJ3$ is shown. In figures B.5 to figure B.7 the applied load, voltage drop readings and crack detection gauge readings are depicted for specimen $VH1$, $VH2$ and $VH4$. In figure B.8 the beach marks of specimen $VJ3$ and $VH4$ are depicted which are used in the main configuration of the DCPD method.

B.1 M(T) specimens

Table B.1 Data of used M(T) specimens for the experiments at room temperature.

Name	$2a_n$ [mm]	W [mm]	t [mm]	R [-]	No. of cycles	P_{max} [kN]	P_{min} [kN]	No. of CDGs*	DCPD config.
JS 17	19.4	60.1	9.7	0.1	75000	50	5	2	Initial
				0.5	15000	50	25		
JS 21	19.4	60.2	9.8	0.1	75000	50	5	1	Initial
				0.5	20000	50	25		
VJ 1	19.4	60	10.5	0.1	75000	50	5	2	Initial
				0.5	20000	50	25		
VJ 2	19.4	60	10.5	0.1	75000	50	5	-	Initial
				0.5	20000	50	25		
VJ 3	19.4	60	10.5	0.1	75000	45	4.5	-	Main
				0.5	20000	45	22.5		
VJ 4	19.4	60	10.5	0.1	75000	50	5	-	Initial
				0.5	15000	50	25		

* CDGs = crack detection gauges

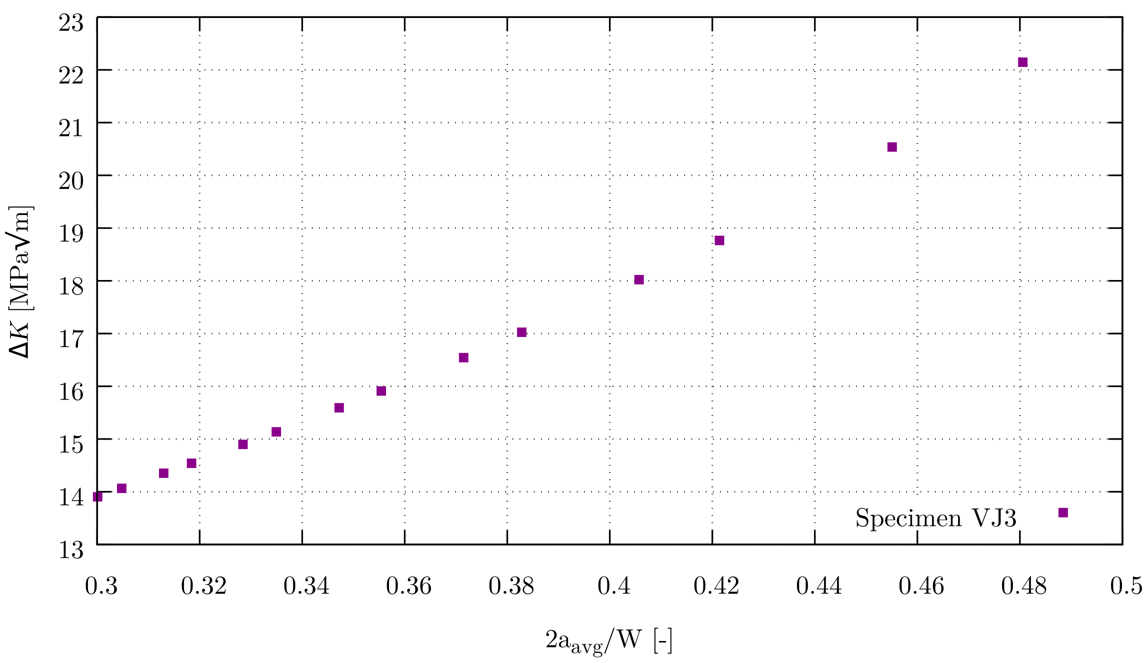

Figure B.1 Stress intensity factor range ΔK versus ratio $2a_{avg}/W$ for specimen $VJ3$.

Table B.2 Data for fatigue crack growth rate curve for specimen $VJ3$.

N	$2a$ [mm]	da/dN [mm/cycles]	ΔK [MPa$\sqrt{\text{m}}$]
281665	23.83	0.00000607	13.90
311167	24.19	0.00000665	14.07
340668	24.58		
374489	24.82	0.00000735	14.35
403988	25.26	0.00000738	14.54
433488	25.69		
469244	26.02	0.00000849	14.90
498743	26.53	0.00000922	15.14
528239	27.07		
563150	27.47	0.00001027	15.59
592644	28.08	0.00001202	15.91
622137	28.79		
657388	29.32	0.00001360	16.54
686878	30.12	0.00001714	17.03
716366	31.13		
751793	31.88	0.00001945	18.02
781277	33.03	0.00002306	18.77
810757	34.39		
845996	35.53	0.00002968	20.54
875470	37.28	0.00003945	22.15
904939	39.61		

Table B.3 Biaxiality factor B and effective stress intensity factor range ΔK^{eff} for methods a), b) and c) of specimen $VJ3$.

B			ΔK^{eff}		
Method a	Method b	Method c	Method a	Method b	Method c
-1.012	-1.002	-1.033	14.86	14.84	14.88
-1.013	-1.003	-1.033	15.03	15.02	15.06
-1.014	-1.003	-1.033	15.35	15.33	15.37
-1.014	-1.004	-1.033	15.56	15.54	15.58
-1.016	-1.005	-1.033	15.95	15.94	15.98
-1.016	-1.005	-1.032	16.22	16.20	16.24
-1.018	-1.007	-1.032	16.72	16.71	16.75
-1.019	-1.007	-1.032	17.08	17.06	17.10
-1.020	-1.009	-1.032	17.79	17.77	17.81
-1.022	-1.010	-1.032	18.33	18.31	18.35
-1.024	-1.012	-1.032	19.46	19.44	19.47
-1.026	-1.013	-1.032	20.31	20.29	20.33
-1.029	-1.015	-1.032	22.36	22.33	22.36
-1.031	-1.017	-1.032	24.24	24.21	24.25

B.1.1 Specimen *VJ*1

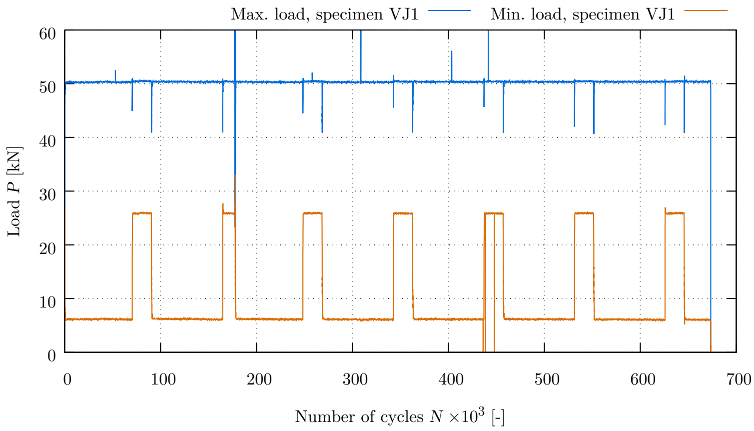

(a) Applied load

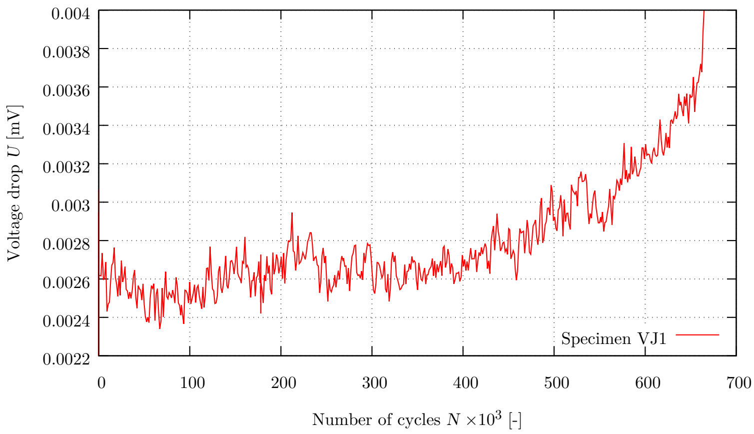

(b) Voltage drop

Figure B.2 Data of specimen $VJ1$.

B.1.2 Specimen *VJ*3

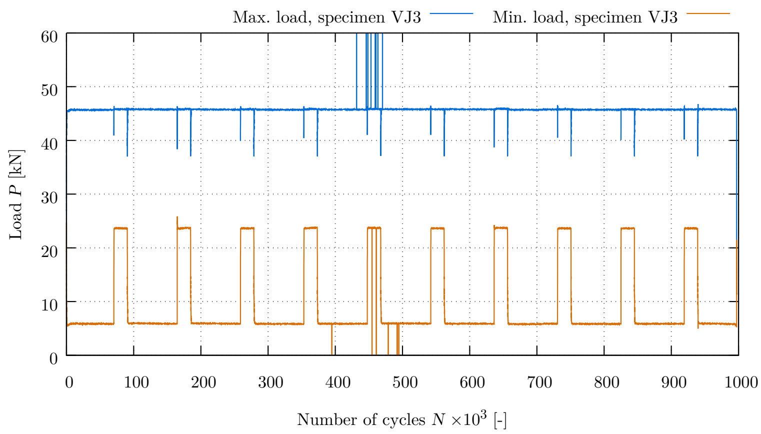

(a) Applied load

Figure B.3 Data of specimen *VJ*3.

B.2 C(T) specimen

Table B.4 Data of used C(T) specimens for the experiments at room temperature.

Name	$2a_n$ [mm]	W [mm]	t [mm]	R [-]	No. of cycles	P_{max} [kN]	P_{min} [kN]	No. of CDGs*	DCPD config.
VH 1	16	80	10.5	0.2	40000	16	3.2	-	Initial
				0.4	10000	16	6.4		
VH 2	16	80	10.5	0.2	40000	12	2.4	1	Initial
				0.4	15000	12	4.8		
VH 4	16	80	10.5	0.1	40000	11	1.1	1	Main
				0.4	17000	11	4.4		

* CDGs = crack detection gauges

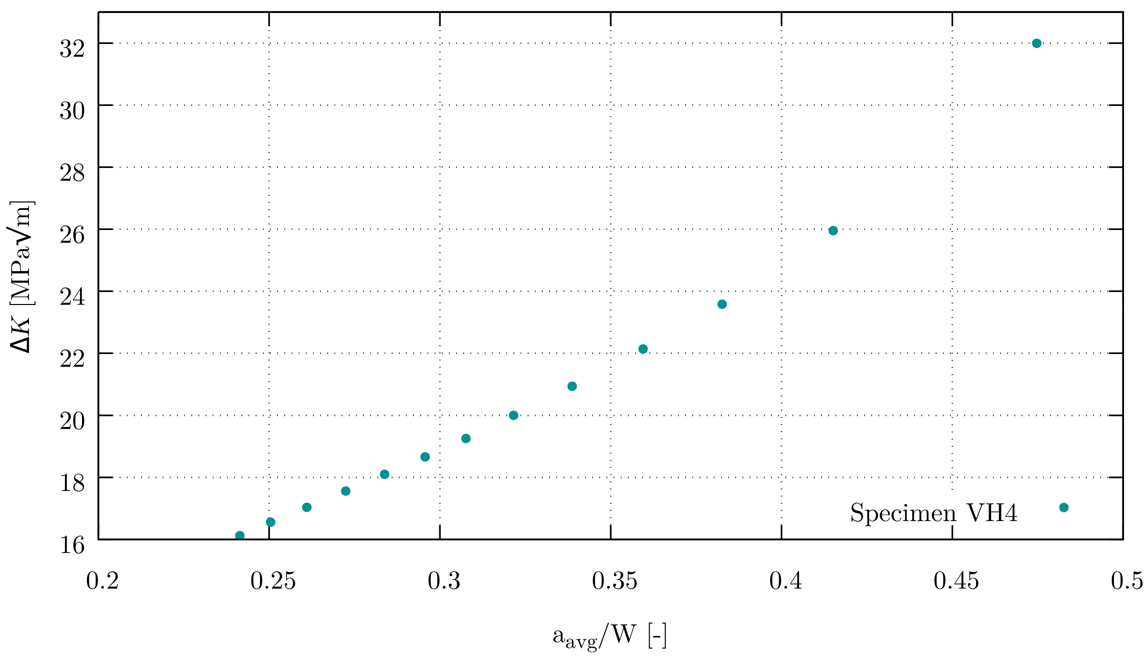

Figure B.4 Stress intensity factor range ΔK versus ratio a_{avg}/W for specimen $VH4$.

Table B.5 Data for fatigue crack growth rate curve for specimen $VH4$.

N	a [mm]	da/dN [mm/cycles]	ΔK [MPa$\sqrt{\text{m}}$]
344567	19.14	0.00001286	16.12
372242	19.50		
398403	19.78	0.00001839	16.55
426206	20.29		
447390	20.62	0.00001863	17.04
475183	21.14		
504300	21.54	0.00001854	17.56
532062	22.05		
561111	22.43	0.00001949	18.10
588847	22.98		
618093	23.40	0.00001896	18.66
645804	23.92		
675062	24.33	0.00002034	19.26
702754	24.89		
731983	25.37	0.00002549	20.00
759634	26.10		
788887	26.67	0.00003102	20.94
816484	27.53		
846142	28.24	0.00003770	22.14
873569	29.28		
902952	29.98	0.00004615	23.58
930014	31.23		
960109	32.28	0.00006953	25.95
987067	34.15		
1016810	35.84	0.00015983	31.99
1043500	40.11		

Table B.6 Biaxiality factor B and effective stress intensity factor range ΔK^{eff} for methods a), b) and c) of specimen $VH4$.

B			ΔK^{eff}		
Method a	Method b	Method c	Method a	Method b	Method c
0.2218	0.2874	0.0458	15.96	15.92	16.09
0.2474	0.3052	0.0731	16.38	16.34	16.50
0.2765	0.3259	0.1051	16.83	16.80	16.95
0.3063	0.3477	0.1389	17.32	17.30	17.45
0.3347	0.3688	0.1721	17.83	17.81	17.96
0.3625	0.3902	0.2060	18.37	18.35	18.49
0.3887	0.4108	0.2390	18.93	18.92	19.05
0.4169	0.4338	0.2762	19.63	19.62	19.74
0.4481	0.4603	0.3195	20.53	20.52	20.63
0.4806	0.4895	0.3680	21.67	21.66	21.76
0.5103	0.5180	0.4166	23.04	23.03	23.12
0.5409	0.5509	0.4745	25.30	25.29	25.36
0.5684	0.5894	0.5481	31.05	31.03	31.08

B.2.1 Specimen *VH*1

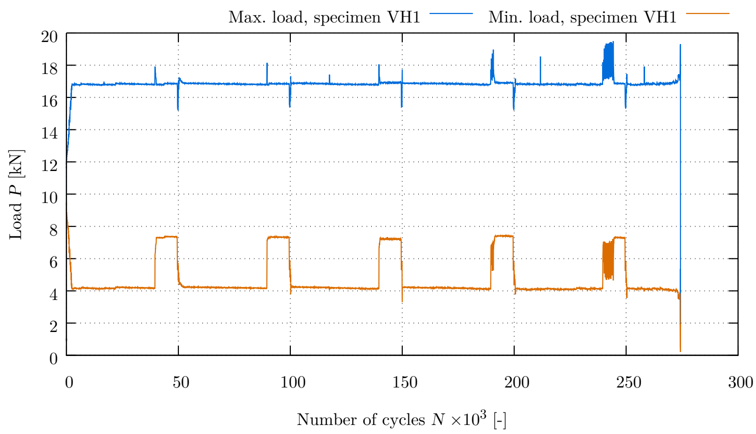

(a) Applied load

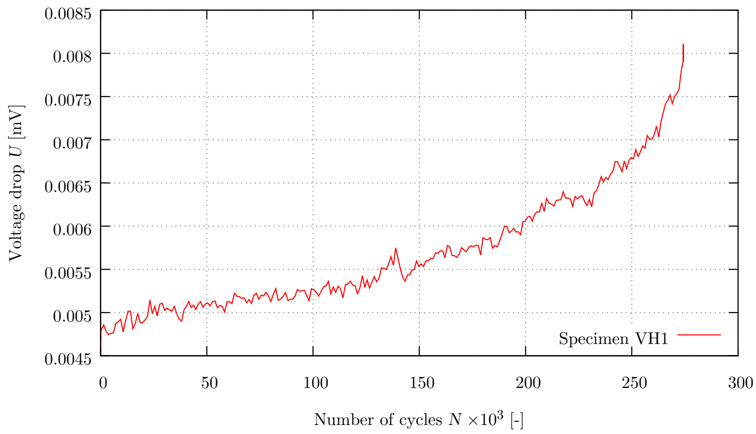

(b) Voltage drop

Figure B.5 Specimen *VH*1.

B.2.2 Specimen *VH*2

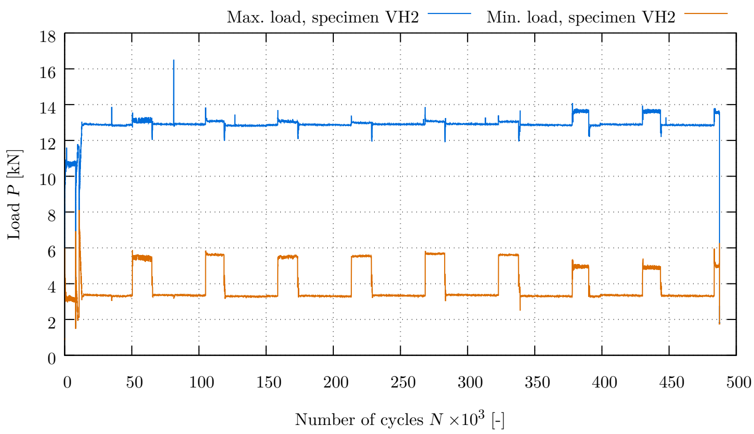

(a) Applied load

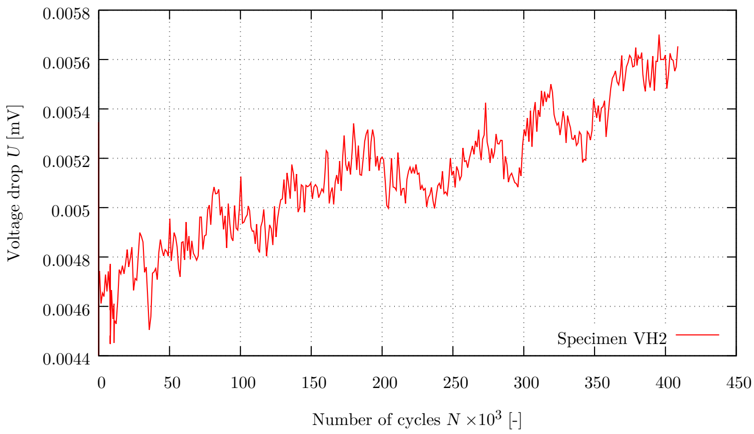

(b) Voltage drop

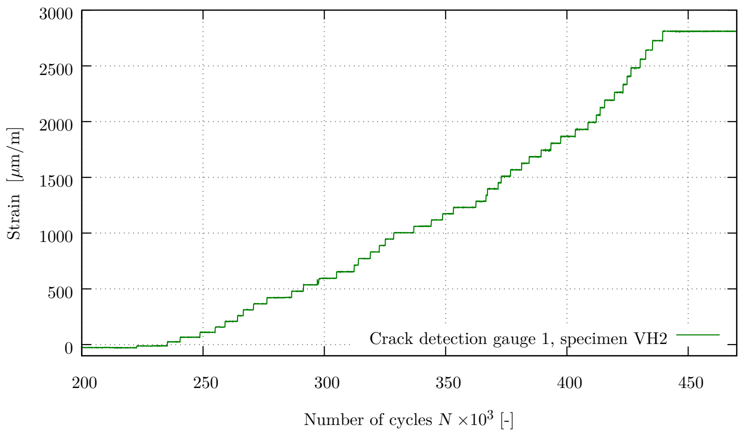

(c) Crack detection gauge

Figure B.6 Specimen *VH*2.

B.2.3 Specimen *VH*4

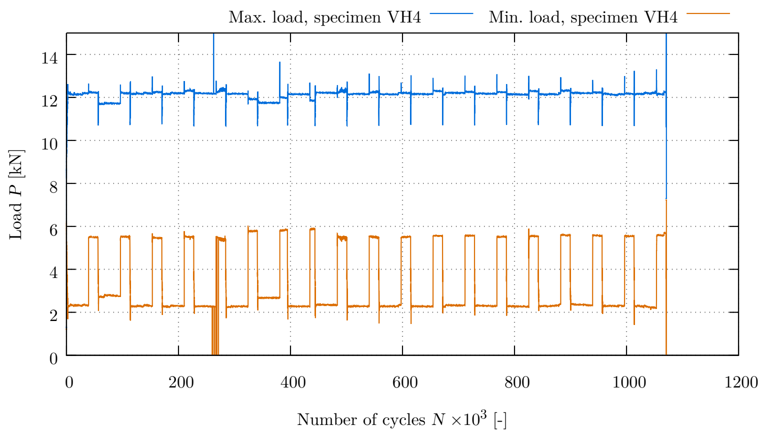

(a) Applied load

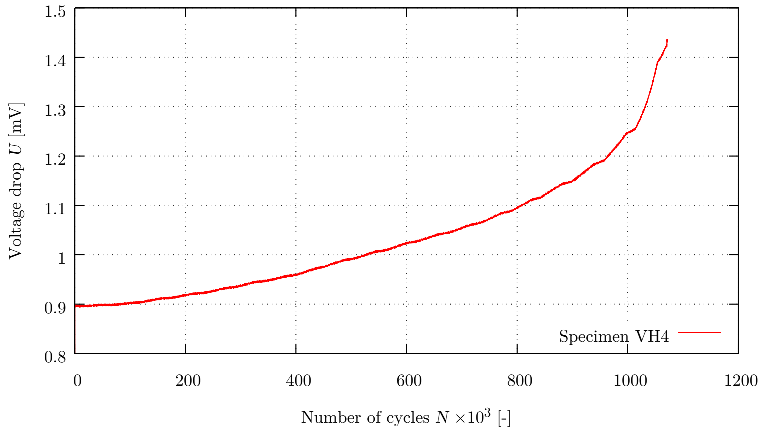

(b) Voltage drop

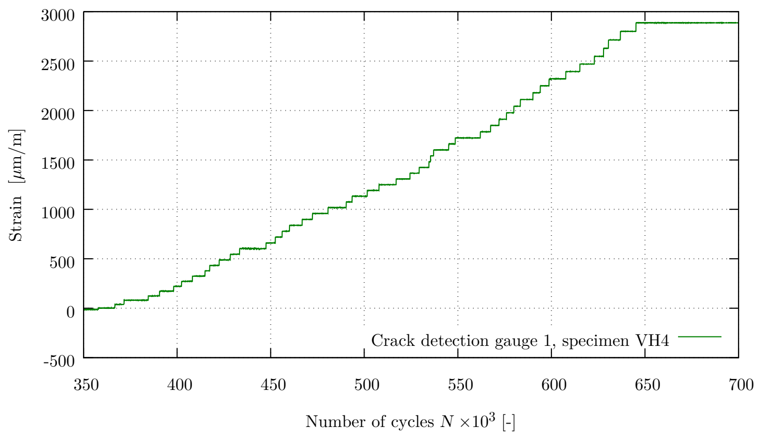

(c) Crack detection gauge

Figure B.7 Specimen *VH*4.

B.3 Beach marks

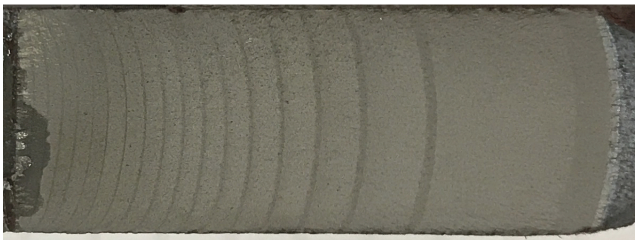

(a) C(T) specimen

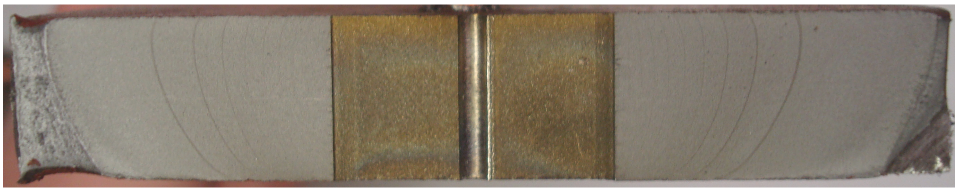

(b) M(T) specimen

Figure B.8 Beach marks of the tested M(T) specimen $VJ3$ and C(T) specimen $VH4$.